Università degli studi di Torino
Facoltà di Scienze Matematiche, Fisiche e Naturali

Corso di Laurea Magistrale in Fisica delle Interazioni Fondamentali
Anno Accademico 2007-2008

The CMS Electromagnetic Calorimeter: preparatory studies for the experiment startup

Tesi di Laurea di
Serena Oggero

Relatrice
Dott.ssa ***Roberta Arcidiacono***

Corelatrice
Dott.ssa ***Nadia Pastrone***

Luglio 2008

If you're gonna live, then live it up
And if you're gonna give then give it up
If you're gonna walk the earth, then walk it proud
And if you're gonna say the word you got to say it loud.

If you're gonna build a house, make it a home
If you're gonna pull some weight, pull your own
If you're gonna help reach out your hand
If you're getting up, then take a stand.

If you're gonna step, step on in
If you're gonna finish, you got to begin
Don't you fear what you don't know
Just let that be your room to grow.

Ben Harper, "Fight For Your Mind"

Contents

Introduction

The Standard Model of electroweak interactions shows a good agreement between theory and experiment, but it does not give an answer to a number of fundamental questions, first of all the origin of particle mass. The electroweak symmetry breaking is not yet fully understood: the mechanism proposed to justify massive particles is based on the existence of a scalar field, which should manifest itself through a massive scalar particle called Higgs boson. The Higgs boson search has been carried out at LEP2 and at Tevatron experiments, but only mass boundaries have been established. Therefore, the Large Hadron Collider (LHC) has been designed with the specific purpose of investigating the origin of particle mass. The choice of a proton-proton collider and its nominal luminosity make of LHC a challenging collider, especially designed for new physics discoveries and for the Higgs boson search in the full allowed mass range.
The work presented in this thesis has been done within the Compact Muon Solenoid (CMS) collaboration. CMS is one of the two general purpose experiments, in conjunction with ATLAS, which are installed at the LHC at CERN. In particular, my work focused on the commissioning with cosmics data and the preparation of software tools for the data analysis of the CMS Electromagnetic Calorimeter. In Chapter 1 a theoretical overview of the Standard Model is provided; in Chapter 2 the LHC collider and the CMS detector are presented. Chapter 3 better focuses on the CMS ECAL performance and illustrates the work done within the ECAL Prompt Feedback Analysis Group during Spring 2008 cosmics data taking; particular emphasis is given to the high energy events analysis. In Chapter 4 the ECAL calibration procedure is described, together with my contribution to the ECAL intercalibration task: a ϕ-symmetry algorithm was studied and optimized on generated jet events. Finally, Chapter 5 describes the High Level Trigger paths to select the $H \rightarrow ZZ^* \rightarrow 4e$ channel; the measurement of paths efficiency, performed both on signal and on backgrounds, is then presented.

Chapter 1

Theoretical Framework: Standard Model Physics

1.1 General concepts

The Standard Model (SM) of Particle Physics is currently the best mathematical description of three of the known interactions with elementary particles and fields. It is based upon the Glashow-Weinberg-Salam model of the electroweak interaction and the Quantum Chromo-Dynamics, model of the strong interaction. Both the GWS and the QCD are quantum field theories.

The theory is based on a local $SU(3)_C \otimes SU(2)_I \otimes U(1)_Y$ gauge symmetry (see Appendix A) and predicts that interactions are mediated by the exchange of vector bosons. Almost all the predictions have been verified to a very high precision.
The aim of this chapter is not to give a complete description of the theory but rather to illustrate its basic principles and the (still not fully answered) fundamental questions.

1.1.1 Elementary Particles

In the Standard Model the elementary particles are (spin $\frac{1}{2}$) fermions, divided into leptons, quarks and their anti-particles. They can be classified in three families (or generations):

$$\text{leptons } \binom{e}{\nu_e}\binom{\mu}{\nu_\mu}\binom{\tau}{\nu_\tau}$$

$$\text{quarks } \binom{u}{d}\binom{c}{s}\binom{t}{b}$$

While leptons can only interact by electromagnetic and weak forces, quarks are subject to both strong and electroweak interaction; they do not exist as free states but as constituents of the hadrons (mesons, if made up of one quark and one anti-quark, and barions, if made up with combinations of three quarks).

Elementary particles interact with each other via the four fundamental interactions, which are mediated by integer-spin particles called bosons[1]:

force	**carrier**	**range**	**relative strength**
Gravitational	graviton G	$\approx \infty$	1
Electromagnetic	photon γ	R $\approx \infty$	10^{36}
Weak	bosons W^+, W^-, Z	R $\approx 10^{-16} cm$	10^{25}
Strong	8 gluons g	R ≈ 1 fm	10^{38}

Since the present work deals both with an electroweak decay and with QCD data, in the next sections the Electroweak and the Quantum Chromo-Dynamics theories will be described.

1.2 The Electroweak sector

The path which lead to a unified theory of weak and electromagnetic interactions took up more than 40 years. From an historical point of view, the starting point is the effective Feynmann- Gell-Mann Lagrangian describing weak processes at low energies as "point-like" interactions. For example, the Lagrangian describing the muon decay is given by

$$\mathscr{L} = -\frac{4G_F}{\sqrt{2}} \left(\bar{\nu}_\mu \gamma^\alpha \frac{1-\gamma_5}{2} \mu \right) \left(\bar{e} \gamma_\alpha \frac{1-\gamma_5}{2} \nu_e \right) \tag{1.1}$$

where G_F is the Fermi constant ($G_F \approx 1.16639 \cdot 10^{-5} GeV^{-2}$), γ_α and γ_5 are Dirac matrices. Eq. 1.1 represents an interaction with only one vertex and without any intermediate boson exchanged and is usually referred to as a "V-A" interaction, because it is formed by a vectorial and an axial component. This Lagrangian is non-renormalizable (higher order perturbative calculations reveal quadratic divergences) and brings to a non-unitary S matrix[2]: a possible remedy is given by requiring the Lagrangian to be invariant under gauge group transformations. The

[1] the relative strenghts are approximate; the exact strengths depend on the particles and energies involved.

[2] that is the *scattering matrix*, whose elements are defined by the Heisenberg in- and out-states: $S_{\beta\alpha} \equiv \langle \beta_{OUT} | \alpha_{IN} \rangle$; S is unitary if $S^\dagger S = S S^\dagger = I$

specific gauge group must be determined by the phenomenological properties of the interaction of the particles involved and the resulting Lagrangian must reduce to Eq. 1.1 in the low energy limit.
The Weinberg-Glashow-Salam model represents a theory for the electroweak unification: it is based not only on the choice of a gauge symmetry group but also on the idea that this symmetry is spontaneously broken so that the electric charge is preserved. In the next paragraphs, first gauge invariances will be described and then the spontaneously symmetry breaking will be investigated.

1.2.1 The gauge invariance

Local symmetries play a central role in modern field theory. A transformation which leaves the Lagrangian invariant is called *local transformation* if it does not need to be the same at each point in space: take for example the gauge symmetry of the electromagnetic field

$$A^\mu(x) \rightarrow A^\mu(x) - \partial^\mu \alpha(x) \tag{1.2}$$

which leaves invariant the Lagrangian

$$\mathscr{L}(x) = -\frac{1}{4} F_{\mu\nu}(x) F^{\mu\nu}(x) \tag{1.3}$$

Using now the coupling of a vector particle to a Dirac spinor ($\bar{\psi} A_\mu \gamma^\mu \psi$), we can obtain the Lagrangian for Quantum Electrodynamics (QED), describing the interaction between a Dirac spinor particle and the electromagnetic field:

$$\mathscr{L} = -\frac{1}{4} F_{\mu\nu}(x) F^{\mu\nu}(x) + \bar{\psi} \left(i \partial_\mu \gamma^\mu - m \right) \psi - e \left(\bar{\psi} A_\mu \gamma^\mu \right) \psi \tag{1.4}$$

The first two terms are the free Lagrangian for the electromagnetic and spinor fields, while the third couples the electromagnetic field to the current $\bar{\psi}\gamma^\mu\psi$ with a coupling constant e which can be identified as the electric charge of the Dirac field. If the invariance under the gauge transformation (1.2) is required, the change in the Lagrangian can be compensated by a change in the phase of the Dirac field (1.5) and by a redefinition of the derivative ∂_μ (1.6). The new derivative is called *covariant*.

$$\psi \rightarrow (e^{ie\alpha(x)})\psi, \quad \bar{\psi} \rightarrow \bar{\psi}(e^{-ie\alpha(x)}) \tag{1.5}$$

$$D_\mu(A) = \partial_\mu + ieA_\mu, \quad \textit{covariant derivative} \tag{1.6}$$

This QED local symmetry belongs to the abelian group U(1)[3].
A fundamental way of looking at the Dirac field phase transformation is to say that any local phase variation on the Dirac field can be compensated by an appropriate local gauge transformation on the electromagnetic field: for this reason it can be said that *local symmetries require the addition of interactions to preserve the symmetry* (Yang & Mills, 1954). Therefore, the QED is based on the gauge group $U(1)_{EM}$, associated to the conserved quantum number Q (electric charge) and the condition of gauge invariance under the $U(1)_{EM}$ group leads to the existence of a massless vector field which can be identified with the *photon*.
If we generalize the concept of local phase invariance to Lagrange densities with n identical Dirac spinor fields, the symmetry group becomes U(n), nonabelian, and the change in the Lagrangian is canceled if a nonabelian gauge or Yang-Mills field $(A^\mu)_{ij}$ is introduced. In both cases, the gauge field A_μ is *massless*: in fact, a mass term would be proportional to $A_\mu A^\mu$ and thus would violate the gauge invariance itself.
Consider now the invariance under a local transformation of the nonabelian $SU(2)$ group: if σ^i are the group generators (i = 1,2,3), the fields transform as

$$\psi(x) \rightarrow e^{i\alpha^i(x)\frac{\sigma^i}{2}}\psi(x) \tag{1.7}$$

and then the covariant derivative takes the form

$$D_\mu \equiv \partial_\mu - igB_\mu = \partial_\mu - ig(A^i_\mu \frac{\sigma_i}{2}) \tag{1.8}$$

A^i_μ are three vector fields, one for each generator of the gauge symmetry group. The (Yang-Mills) gauge invariant Lagrangian density will have a free term for the ψ_i fields, and also a kinetic term for the nonabelian gauge fields and especially new interaction terms:

$$\mathscr{L}_{YM} = \bar{\psi}_i \left(i\gamma_\mu (D^\mu)_{ij} - m\delta_{ij}\right)\psi_j - \frac{g}{2}\bar{\psi}\gamma^\mu A^i_\mu \sigma^i \psi - \frac{1}{2} tr F_{\mu\nu}F^{\mu\nu} \tag{1.9}$$

The requirement of gauge invariance has led not only to the coupling of the gauge fields to the fermions, but also to new interactions: as a consequence of the theory being nonabelian, three- and four-gauge-bosons vertices are allowed.

As already mentioned, to unify electromagnetic and weak interactions, a gauge theory for weak interaction is needed. Proposed by Weinberg (1967), Glashow

[3] U(n) is the nxn unitary matrices group

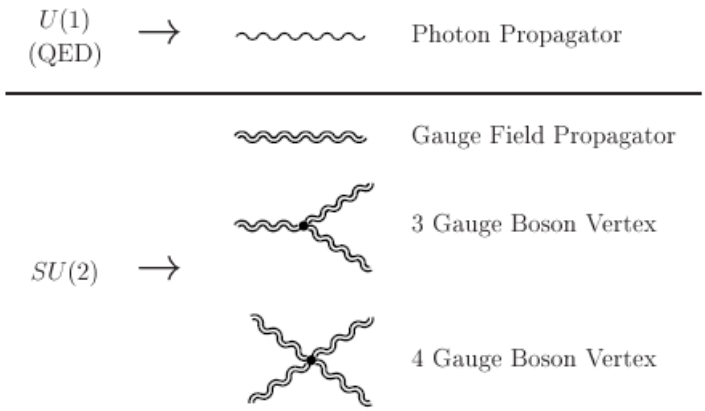

Figure 1.1: Examples of coupling prescribed by an abelian ($U(1)$) and nonabelian ($SU(2)$) gauge symmetry group

(1961) and Salam, the Standard Model of electroweak interaction was basically formulated by extending the gauge symmetry to the group $SU(2)_I \otimes U(1)_Y$, that is the largest possible symmetry group associating the leptons according to the experimental knowledge at that time. The generators of $SU(2)_I$ are the three components of the weak isospin operator ($t^a = \frac{1}{2}\tau^a, \tau^a$ are the Pauli matrices), while the generator of $U(1)_Y$ is the weak hypercharge Y operator. The corresponding quantum numbers satisfy the following relation

$$Q = I_3 + \frac{Y}{2}$$

where I_3 is the t_3 eigenvalue. Fermions can be divided in doublets of negative-helicity (left-handed) particles and singlets of positive-helicity (right-handed) particles; neutrinos have no right component as their mass is ≈ 0. In the following table all fermions quantum numbers are shown.

	I_3	Y	Q
$\binom{u_L}{d_L}$	$\binom{\frac{1}{2}}{-\frac{1}{2}}$	$\binom{\frac{1}{3}}{\frac{1}{3}}$	$\binom{\frac{2}{3}}{-\frac{1}{3}}$
u_R, d_R	0, 0	$\frac{4}{3}$, $-\frac{2}{3}$	$\frac{2}{3}$, $-\frac{1}{3}$
$\binom{\nu_{l,L}}{l_L}$	$\binom{\frac{1}{2}}{-\frac{1}{2}}$	$\binom{-1}{-1}$	$\binom{0}{-1}$
l_R	0	-2	-1

Setting the local invariance of the theory under a $SU(2)\otimes U(1)$ transformation

introduces 4 massless gauge fields: three fields ($W_\mu^{1,2,3}$) correspond to the $SU(2)$ symmetry group and one field (B_μ) corresponds to the $U(1)$ symmetry group. They appear in the definition of the covariant derivative and couple to fermions with two different coupling constants, but do not represent physical fields: a linear combinations of them is needed to obtain the physical fields and the relative currents. From the gauge-invariant Lagrangian for fermion fields (see Eq. 1.10)

$$\mathscr{L} = \bar{\psi}_L \gamma^\mu \left(i\partial_\mu + g t_a W_\mu^a - \frac{1}{2} g' Y B_\mu \right) \psi_L + \bar{\psi}_R \gamma^\mu \left(i\partial_\mu - \frac{1}{2} g' Y B_\mu \right) \psi_R \quad (1.10)$$

(please note that ψ_L and ψ_R are summed over all the flavour possibilities), the physical fields can be obtained by the following combinations:

$$W_\mu^\pm = \sqrt{\frac{1}{2}} \left(W_\mu^1 \mp i W_\mu^2 \right) \quad (1.11)$$

$$A_\mu = B_\mu \cos\theta_W + W_\mu^3 \sin\theta_W \quad (1.12)$$

$$Z_\mu = -B_\mu \sin\theta_W + W_\mu^3 \cos\theta_W \quad (1.13)$$

Thus, $W^\pm$ correspond to the charged bosons, while A_μ and Z_μ correspond to the neutral bosons γ and Z and are obtained by mixing the neutral fields W_μ^3 and B_μ with a rotation defined by the Weinberg angle θ_W. In terms of the new fields, the lagrangian interaction term between gauge fields and fermions becomes

$$\mathscr{L}_{int} = \frac{1}{2\sqrt{2}} g \left(J_\alpha^+ W^{(+)\alpha} + J_\alpha^- W^{(-)\alpha} \right) + \frac{1}{2} \sqrt{g'^2 + g^2} J_\alpha^Z Z^\alpha - e J_\alpha^{EM} A^\alpha \quad (1.14)$$

where J^{EM} is the electromagnetic current coupling to the photon field, J^+, J^- and J^Z are the three weak isospin currents. The currents are bound by relation 1.15.

$$J_\alpha^Z = J_\alpha^3 - 2\sin^2\theta_W \cdot J_\alpha^{EM} \quad (1.15)$$

Finally, the identification of A_μ with the photon field leads to the *electroweak unification*:

$$g \sin\theta_W = g' \cos\theta_W = e$$

The GWS model for electroweak unification thus predicts the existence of two charged gauge fields, which can only couple to left-handed fermions, and two neutral gauge fields, interacting with both left- and right-handed components.

1.2.2 Spontaneously broken symmetries

As previously seen, the principle of local invariance is a consistent way to have massless vector bosons candidates into the theory; nevertheless, in order to be used to describe the weak interactions they must acquire a mass. This can be obtained by means of a spontaneous breaking of the symmetry, which makes possible Lagrangians that have at once local gauge invariance and massive vector particles.

Spontaneous symmetry breaking generally refers to any situation in which a system as a set of degenerate ground states, related by continuous symmetry transformations. In plain words, the symmetry is said to be spontaneously broken if the theory Lagrangian is invariant under a given symmetry but its physical vacuum is not.
There are several occurrences of spontaneous symmetry breaking, for instance in the theory of superconductivity; the Standard Model for elementary interactions is based on a Lagrangian with spontaneous symmetry breaking, too. An example of spontaneous symmetry breaking in a complex scalar theory is realized with a global *U(1)* symmetry: starting from a Lagrangian $\mathscr{L}$ with a chosen effective potential $V(\phi\phi^*)$

$$\mathscr{L} = \partial_\mu\phi(\partial^\mu\phi)^* - V(\phi^*\phi) \tag{1.16}$$

$$V(\phi^*\phi) = -\mu^2\phi^*\phi + \frac{\lambda}{2}(\phi^*\phi)^2, \quad \lambda > 0 \tag{1.17}$$

two cases can be considered:
· $\mu^2 < 0 \Rightarrow$ the symmetry is exact and there is a unique vacuum state for the theory at $\langle\phi\rangle = 0$;
· $\mu^2 > 0 \Rightarrow$ the vacuum state is infinitely degenerate for all the configurations which satisfy

$$|\phi| = \left(\frac{\mu^2}{\lambda}\right)^{1/2} \equiv v$$

The choice of one of the configurations spontaneously breaks the symmetry. In Fig. 1.2 the V potential is shown for different μ values.

For instance, if a vacuum configuration with only a real part ($\langle\phi\rangle_0 = \mathrm{v}$) is chosen, we can introduce ϕ_1 and ϕ_2 (real scalar fields) and define $\phi(x)$ as

$$\phi(x) = v + \frac{1}{\sqrt{2}}(\phi_1(x) + i\phi_2(x)) \tag{1.18}$$

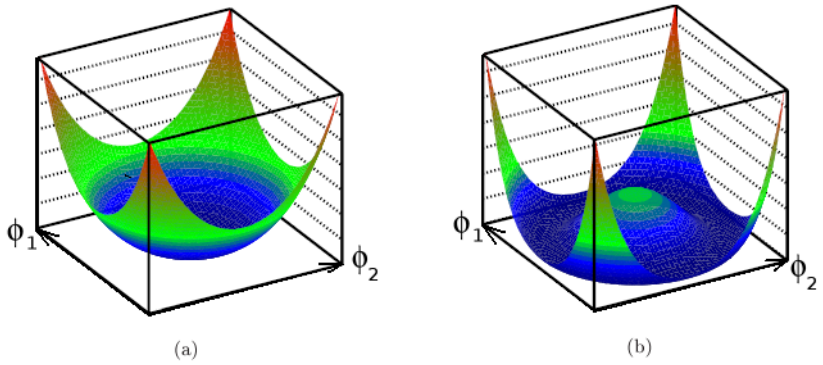

Figure 1.2: Potential $V(\phi^*\phi)$ for $\mu^2 > 0$ (a) and $\mu^2 < 0$ (b).

The potential and the Lagrangian then become

$$V(\phi^*\phi) \approx \frac{\mu^4}{2\lambda} + \frac{1}{2}\mu^2\phi_1^2 \tag{1.19}$$

$$\mathscr{L} = \frac{1}{2}(\partial_\mu\eta)(\partial^\mu\eta) + \frac{1}{2}(\partial_\mu\xi)(\partial^\mu\xi) + \mu^2\phi_1^2 \tag{1.20}$$

So the field ϕ_1 has acquired a mass $\sqrt{2}\mu$, as a consequence of the restoring force against radial oscillations, while ϕ_2 remains massless, since the Lagrangian keeps its symmetry under U(1) rotations. The fact that massless scalars appear when a global continuous symmetry is spontaneously broken is a consequence of the *Goldstone's theorem*: after a spontaneous breakdown of the *O(N)* symmetry to an *O(N-1)* one, we find that:

- $\frac{(N-1)(N-2)}{2}$ are still unbroken symmetries,
- *(N-1)* is the number of massless Goldstone bosons, corresponding to as many broken symmetries.

In the previous example, if *U(1)* is a local symmetry group, then plugging the $\phi(x)$ expression (Eq. 1.18) into the Lagrangian gives a different result: a new kinetic term is generated, due to the covariant derivatives; in particular the gauge boson A_μ acquires a mass proportional to the vacuum value v chosen for the field ϕ. Exactly this "link" between local invariance and spontaneous symmetry breaking allowed Higgs (1964) to solve the problems associated with the weak interactions description.

1.2.3 A spontaneously broken symmetry mechanism: the Higgs mechanism

The Standard Electroweak model is based on the gauge group $SU(2)_I \otimes U(1)_Y$: by requiring the theory to fulfill this local symmetry and, at the same time, by introducing new fields subjected to certain effective potentials, the massive gauge bosons problem is solved. The Goldstone scalars disappear, giving the (previously massless) gauge bosons one more degree of freedom, that is a transversely polarized state.
The field introduced into the theory is the scalar Higgs field ϕ, in order to give a mass to the weak gauge fields and to keep massless the photon field. Thus, the simplest choice for ϕ is a doublet representation of *SU(2)*:

$$\phi \equiv \begin{pmatrix} \phi^0 \\ \phi^+ \end{pmatrix}$$

In this way, ϕ transforms under $SU(2) \otimes U(1)$ as

$$\phi \rightarrow e^{i\alpha^i \tau^i} e^{i\beta/2} \phi$$

where α and β are real numbers and a charge 1/2 under *U(1)* is given. Then, a vacuum expectation value is chosen, in order to break the *SU(2)* symmetry (and not *U(1)*):

$$\langle \phi \rangle = \frac{1}{\sqrt{2}} \begin{pmatrix} 0 \\ v \end{pmatrix}$$

$\langle \phi \rangle$ is not invariant under any of the original four generators, but it is invariant under the transformation corresponding to the electric charge

$$Q = (\tau^3 + Y/2)$$

In this way, the 3 bosons corresponding to the weak sector become massive, via the Goldstone scalars associated with the 3 broken symmetries; on the other hand, the photon field remains massless as expected. Eq. 1.21 shows the masses for the weak gauge bosons.

$$m_{W^\pm} = g\frac{v}{2} \ , \quad m_Z = \sqrt{g^2 + g'^2}\frac{v}{2} \tag{1.21}$$

Thus, three free parameters of the gauge sector exist: the two coupling constants g and g', and the vacuum expectation value v of the Higgs field; they are usually expressed using the electromagnetic coupling constant ($\alpha_{e.m.}$), the Fermi constant (G_F) and the mass of the Z boson, which are measured with very high accuracy.

1.2.4 Higgs model and limit on Higgs boson mass

The introduction of the Higgs field in the Standard Model theory gives mass to gauge bosons, but a new massive scalar particle is also expected to appear. First, the Lagrangian for ϕ is

$$\mathscr{L} = (D_\mu \phi)^\dagger (D_\mu \phi) - V(\phi^\dagger \phi) \tag{1.22}$$

$$V(\phi^\dagger \phi) = \mu^2 \phi^\dagger \phi - \lambda (\phi^\dagger \phi)^2 \tag{1.23}$$

and the Higgs potential (see Fig. 1.3) reaches a minimum at

$$v \equiv (\frac{\mu^2}{\lambda})^{1/2}$$

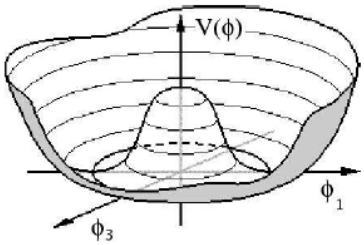

Figure 1.3: Representation of the Higgs potential.

Then, if we parametrize the expansion of ϕ using a real field *H(x)* with $\langle H(x) \rangle = 0$

$$\phi(x) = \frac{1}{\sqrt{2}} \begin{pmatrix} 0 \\ v + H(x) \end{pmatrix} \tag{1.24}$$

the potential becomes

$$\mathscr{L} = -\mu^2 H^2 - \lambda v H^3 - \frac{1}{4} \lambda H^4 \tag{1.25}$$

Higgs couplings. So, the field H is a massive scalar, with mass $m_H = \sqrt{2\lambda} v$, and it is identified with the so-called *Higgs boson*. Moreover, if we write the kinetic term, we recognize the Higgs boson coupling to the gauge bosons, together with the cubic and quartic self-interaction couplings (see Fig. 1.4 for the Higgs and gauge boson interactions diagrams):

$$\mathscr{L}_{kin} = \frac{1}{2}(\partial_\mu H)^2 + (m_W^2 W_\mu^+ W^{\mu-} + \frac{1}{2} m_Z^2 Z_\mu Z^\mu) \cdot \left(1 + \frac{H}{v}\right)^2 \tag{1.26}$$

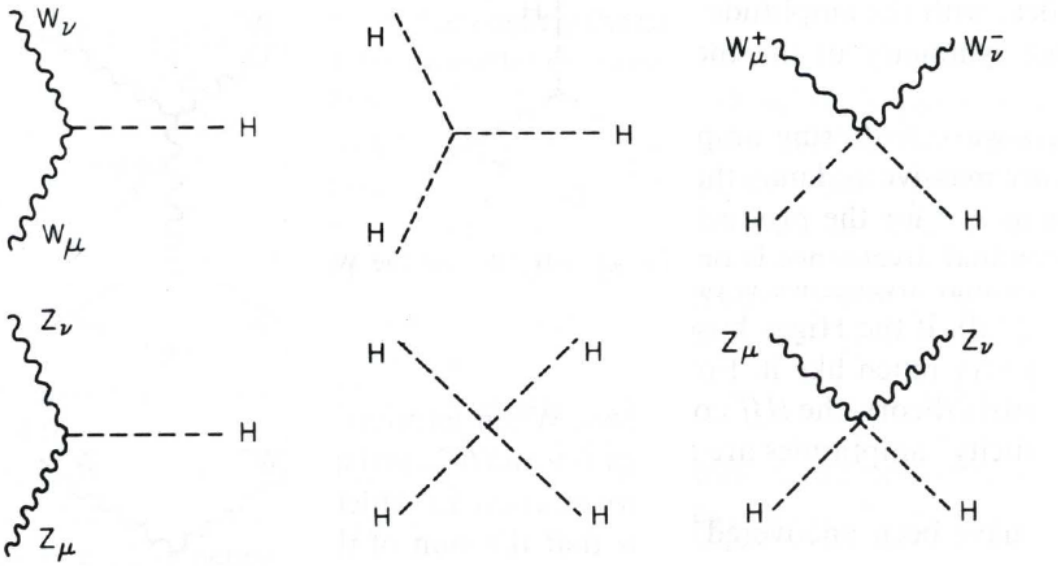

Figure 1.4: Feynman diagrams for the Higgs and gauge bosons interaction.

As for fermions, although the electroweak symmetry is broken, the electroweak theory does not predict the fermion mass values; in fact, a mass term of the generic form

$$-m\psi\bar{\psi} = -m(\bar{\psi}_L\psi_R + \bar{\psi}_R\psi_L)$$

is not allowed, because it would break the gauge invariance in the Lagrangian. This is due to the fact that ψ_R and ψ_L belong to different *SU(2)* representations and have different *U(1)* charges. Every fermion needs the so-called *Yukawa coupling*, whose value must match the observed mass: it is possible to build a mass term to fermions by introducing a Yukawa coupling to the Higgs field (see Eq.1.27).

$$\mathscr{L}^f_{Yukawa} = -g_f(\psi^f_L \phi \psi^f_R + \psi^f_R \phi^\dagger \psi^f_L) \tag{1.27}$$

According to (Eq. 1.24), the Higgs coupling to fermions is

$$\mathscr{L}_f = -m_f \bar{f} f \left(1 + \frac{H}{v}\right) \tag{1.28}$$

and the mass for a lepton or a quark (i) results then proportional to its Yukawa coupling to the Higgs:

$$m_i = g_f \frac{v}{\sqrt{2}}$$

Constraints on Higgs boson mass and Higgs search. The Higgs mass is a free parameter of the Standard Model, but there are both theoretical arguments and experimental evidences giving limits on it.
As for theoretical constraints (see Fig. 1.5), if we assume the SM not to be a fundamental theory but an effective one, we can say SM to be valid at least up to a certain energy scale Λ, over which the perturbative theory is no longer valid.

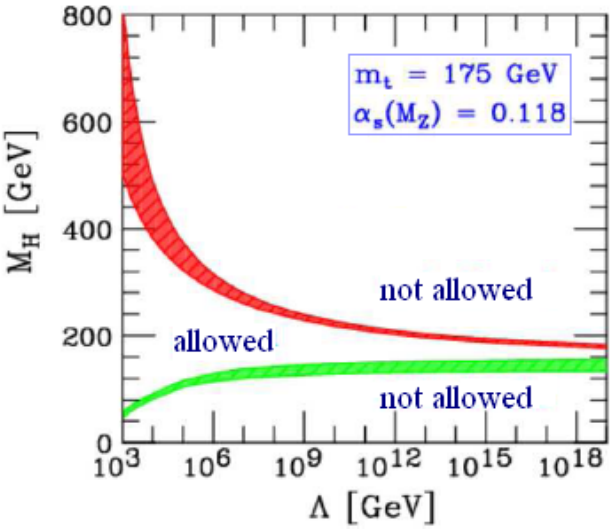

Figure 1.5: Theoretical limits on the Higgs boson mass, assuming the validity of the SM up to an energy scale Λ; the solid areas show the uncertainties in the bounds.

Then, a lower bound comes from the requirement for the symmetry breaking to actually occur, that is the requirement for the Higgs potential to be bounded below ($V(\langle\phi\rangle) < V(0)$): λ must be positive also after the radiative corrections (*absolute vacuum stability*). The upper bound comes from the requirement for λ to keep finite up to the scale Λ, although it increases with energy (*consistency of the electroweak theory*).

Therefore, if we assume SM to be valid up to $\Lambda \approx 10^{19}$ GeV (i.e. Planck energy scale), the Higgs boson mass is expected to lie between ≈ 130 GeV/c^2 and 190 GeV/c^2; on the other side, if $\Lambda \approx 1\ TeV$, the Higgs mass must be lower than 500 GeV/c^2.
Beside, better limits on the Higgs boson mass are provided by the experimental

data: Higgs boson searches have been done in electron and hadron colliders, and there are also indirect searches using the precision electroweak measurements. At LEP, a Higgs direct search was performed, exploiting the Higgstrahlung and WW-fusion production processes (see Fig. 1.6 for the respective Feynmann diagrams).

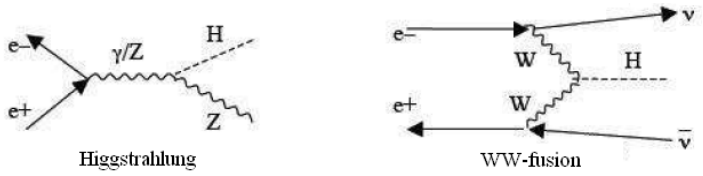

Figure 1.6: Feynmann diagrams for Higgs production processes at LEP.

LEP was an electron-positron collider which reached a centre of mass energy of 209 GeV; due to its simple initial state, it was the ideal machine for a direct Higgs search in the range $m_H < E_{CM} - m_Z$. The Higgstrahlung process ($e^+e^- \rightarrow HZ$) prevails for $m_H << E_{CM} - m_Z$, while the WW-fusion allows a Higgs production toward higher mass values; although its cross section is much lower than the Higgstrahlung cross section, the two processes interfere positively at the so-called "Higgstrahlung wall" (i.e. the kinematic limit of $m_H \approx E_{CM} - m_Z$). In Fig. 1.7 the cross section for Higgs production at LEP is shown.

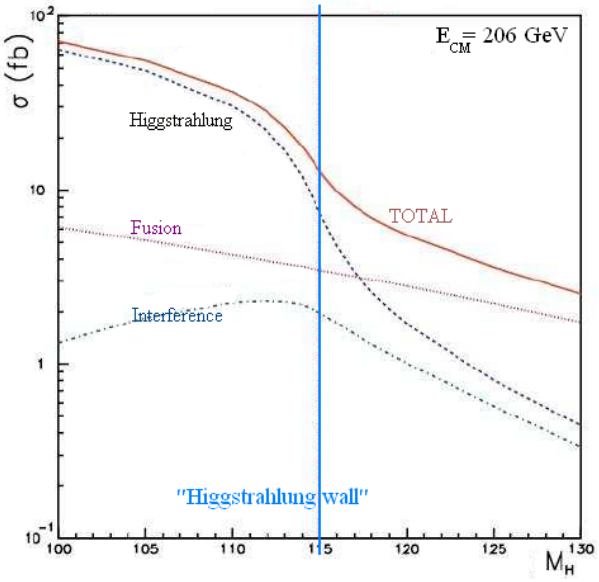

Figure 1.7: Higgs production cross section at LEP.

Thanks to the 4 LEP experiments results, the direct search for the SM Higgs boson sets the lower limit at 114.4 GeV/c^2 for a 95% confidence level. Finally, indirect constraints are based on the requirement for all the measurements of electroweak variables (asymmetry measurements, $W^{\pm}$ mass, top quark mass, etc.) to be consistent (*global electroweak fit*), since Higgs mass appears in one-loop readiative corrections. Global fits to electroweak measurements performed at LEP, SLD, Tevatron, constrain the Higgs mass to be less than about 144 GeV/c^2 (182 GeV/c^2 if the direct search lower limit is considered). The results (July 2007) are shown in Fig. 1.8: solid line shows the fit, the blue band around the fit curve shows the theoretical uncertainty induced by higher order corrections, the yellow region is the region excluded from the direct search at LEP. The fit minimum is at about $m_H = 76^{+33}_{-24}$ GeV/c^2, for a 68% confidence level.

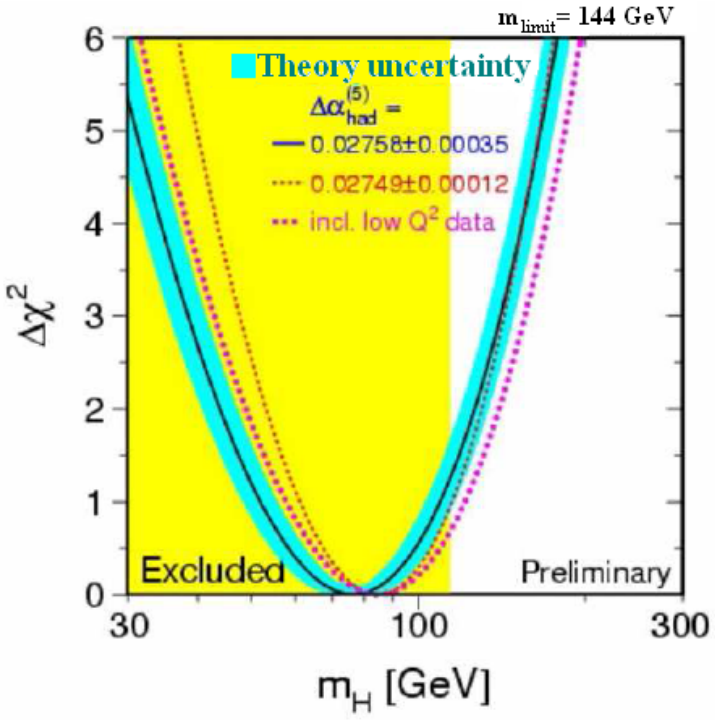

Figure 1.8: $\Delta\chi^2 = \chi^2 - \chi^2_{min}$ vs m_H (global fit to electroweak measurements, with $m_t = 170.9 \pm 1.8$).

However, indirect constraints on Higgs boson mass have a limited sensitivity, since second order corrections to SM observables depend only logarithmically on m_H, while fermions give contributions quadratically dependent on m_f: thus, uncertainty on the top quark mass can sensibly shift the constraints on m_H, due to the large m_t comparable to the predicted Higgs mass. In Fig. 1.9 the Higgs

mass constraints from m_t values is shown.

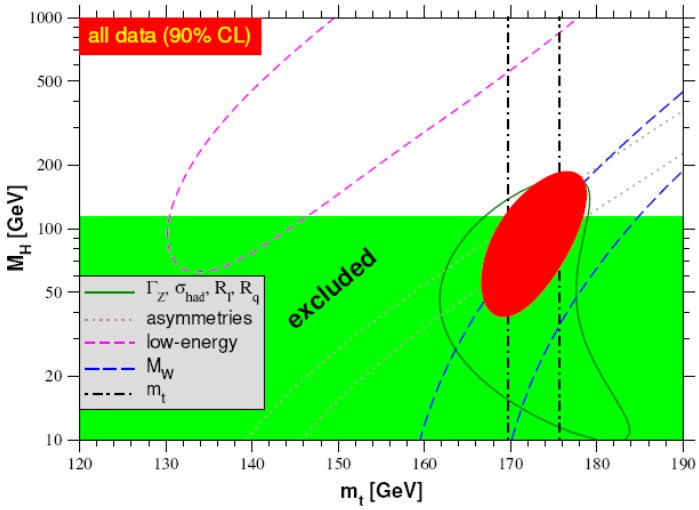

Figure 1.9: SM Higgs mass as a function of top mass.

1.2.5 Standard Model and Higgs Physics at LHC

As will be better described in the following chapter, Large Hadron Collider is a proton-proton collider whose main goal is to elucidate the nature of electroweak symmetry breaking for which the Higgs mechanism is presumed to be responsible. Actually, hadron colliders are well suited for the exploration of new energy domains, and the LHC design luminosity of $10^{34} cm^{-2} s^{-1}$, with a beam energy of 7 TeV, has been chosen to study physics at the TeV energy scale. The experimental study of the Higgs mechanism will hopefully bring to new discoveries at energy scales above 1 TeV.
In this chapter, the phenomenology of Higgs physics at the LHC is described, together with the mechanisms of Higgs production in 14 TeV centre-of-mass energy pp collisions and the search strategies for different mass regions.

LHC collisions. The QCD model (see section 1.3) describes the interaction between two protons with the parton model approximation: the incoming beam of hadrons is considered equivalent to a beam of partons (identified with quarks and gluons), whose momentum distributions inside the hadron is characterized by the parton density functions *pdf* $f_i(x, \mu)$ (μ is the typical energy scale of the process). In particular, $dx\ f_i(x, \mu)$ gives the probability to find a parton i carrying

a fraction of the hadron initial momentum p included between x and $x + dx$. The *pdf*s are universal functions, since they do not depend on the analysed process. Then, the production cross section of a certain final state with high invariant mass from the interaction of two protons beams can be described by

$$\sigma(p_1, p_2) = \sum_{i,j} \int dx_1 dx_2 f_i(x_1, \mu) f_j(x_2, \mu) \sigma_{ij}(x_1 p_1, x_2 p_2, \alpha_s(\mu), \mu)$$

where p_1 and p_2 are the two protons beams momenta. In Fig. 1.10 the cross-section for the most important processes at LHC is shown.

In spite of the LHC high centre of mass energy, the cross section of interesting events will be several order lower than the total one (see Tab. 1.1).

Process	**Cross section**	**Events/sec**	**Events/year**
$W \to e\nu$	20 nb	15	10^8
$Z \to ee$	2 nb	1.5	10^7
$t\bar{t}$	1 nb	0.8	10^7
bb	2 0.8 mb	10^5	10^{12}
H ($m_H \approx 800$ GeV)	1 pb	0.001	10^4
H ($m_H \approx 200$ GeV)	20 pb	0.002	10^5

Table 1.1: Rates and cross section for some interesting processes at LHC (luminosity of 2 $\cdot 10^{33} cm^{-2} s^{-1}$)

The total cross section for proton-proton interactions was measured[4] as

$$\sigma_{tot} = (100 \pm 20) mb$$

where the purely elastic contribution has been considered.
The inelastic processes can be

soft collisions, with a great impact parameter between the two partons, and a small transferred momentum; they produce great transverse momentum particles ($\approx$ 500 MeV/c) which generally go into the beam pipe and can not be revealed;

hard collisions, with a small impact parameter and a higher transferred momentum; particles with a great transverse momentum and a high scattering

[4]UA4, UA5, E710 measurements

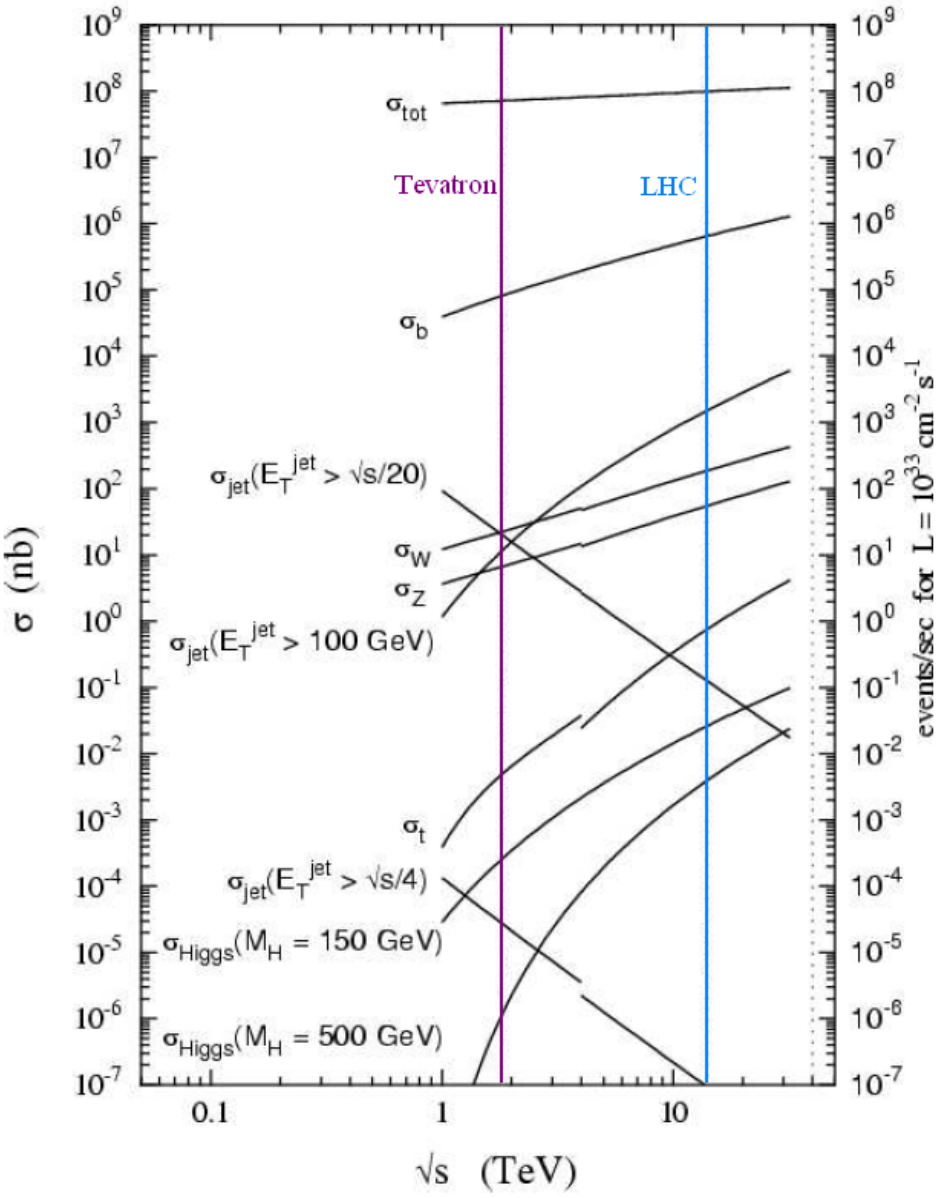

Figure 1.10: Cross section for the most important LHC processes; the rate of events per year is reported on the right scale, for an integrated luminosity of 100 fb^{-1}.

angle are produced. The rare and interesting events are typically hard scattering events.

To increase the interesting events rate, a high luminosity is needed, but this leads to the so-called *pile-up*: several interactions overlap in the same bunch crossing and each interesting event is superimposed by other soft events. With a luminosity of $10^{34} cm^{-2} s^{-1}$, ≈ 17.3 events overlapped are expected for each bunch crossing.

SM Higgs production in *p-p* collisions. In Fig. 1.11, the cross section trend for Higgs boson production processes is shown.

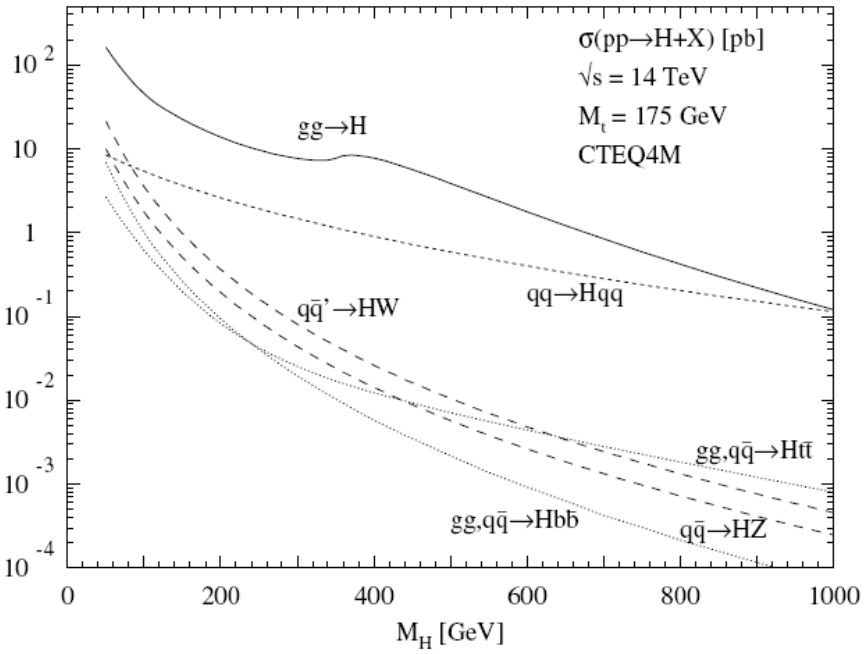

Figure 1.11: Cross section trend for the Higgs production processes at LHC.

The dominant Higgs production mechanism at the LHC will be gluon-fusion process

$$pp \rightarrow gg \rightarrow H$$

(see diagram (a) in Fig. 1.12).

This process provides the largest production cross section for the whole Higgs mass range, because of the much larger gluon density in the proton than the quark density at around 100 GeV/c^2 masses at the LHC energy. It is mediated

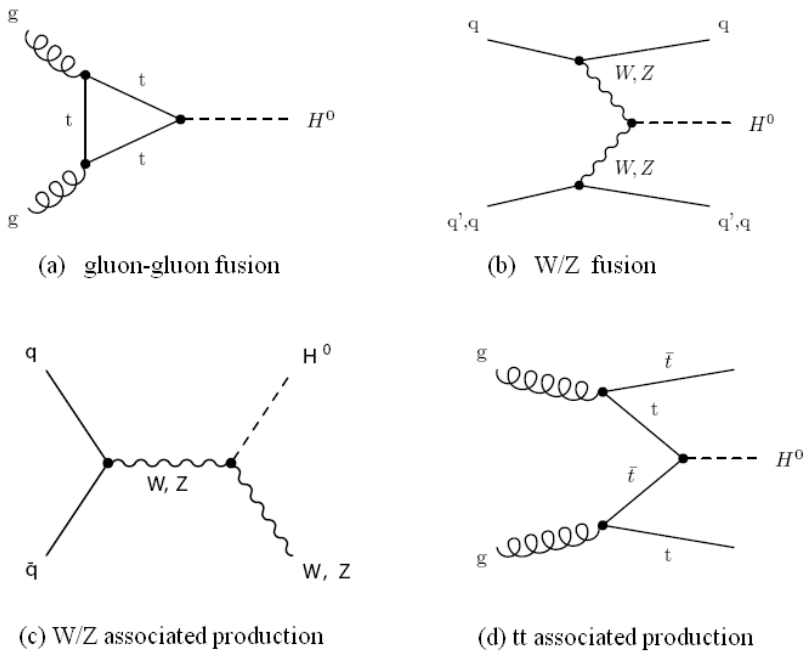

Figure 1.12: Feynman diagrams for the Higgs boson production processes.

by t or b quark loops; the t-quark loop prevails, due to its higher mass. There are large next-to-leading order (NLO) QCD corrections to this process and the corrections are known up to next-to-next-to-leading order (NNLO), although a full massive NNLO calculation is not available so that NNLO results can only be trusted for small and intermediate Higgs masses. The theoretical uncertainties of the total cross section can be estimated as $\approx 20\%$ at NNLO.
For large Higgs masses the W and Z boson-fusion processes

$$pp \rightarrow qq \rightarrow qq + WW/ZZ \rightarrow qqH$$

become competitive (see Fig. 1.12 for the leading order diagram (b)). Although this process cross section is about an order of magnitude smaller than the gluon-fusion one, it is a promising channel for the discovery of a SM Higgs boson especially in the intermediate mass range ($130\ GeV/c^2 < m_H < 180$ GeV/c^2), due to its unique kinematics and QCD properties. In fact, it is characterized by two forward jets with transverse momentum $p_T \approx m_W/2$; between the forward jets, a large rapidity gap, in which the decay products of the Higgs boson lie, is expected. Also, NLO corrections are known for the W/Z-fusion.
In the intermediate mass range $m_H < 2m_Z$, an alternative signature can be pro-

vided by Higgstrahlung process, with the associated production of W/Z bosons:

$$pp \rightarrow q\bar{q} \rightarrow Z^*/W^* \rightarrow H + Z/W$$

The decay products of W or Z bosons are used to identify such events. This channel is suppressed because its cross section (for $m_H > 200$ GeV/c^2) is two order of magnitude smaller than the others; nevertheless, it is effective in the intermediate mass range and has a particularly clear signature when the boson decays leptonically.

For Higgs masses below 150 GeV/c^2, a significant role is played by the associated production with a $t\bar{t}$ pair:

$$pp \rightarrow q\bar{q}/hh \rightarrow Ht\bar{t}$$

Its cross section decreases with m_H and it is 50 pb lower than gluon-gluon fusion cross section, for a high mass range. In spite of that, it is interesting due to final state signature: t-quark most probably decays into a W boson and b-quark pair; the final state can thus be characterized by 2 b-tagged jets and two W bosons decaying into leptons.

Higgs boson decays. Since the Higgs couplings to particles increases with the particle mass, the probability of the Higgs boson to decay into high mass particles is larger, as long as the kinematics allows it. Thus, Higgs boson couples preferably with the Z and W bosons, with the *tau* lepton and the b or t quarks. It can not couple with photons and gluons at the tree level, but only loop-diagrams are permitted. The branching ratios for the SM Higgs boson as a function of the Higgs boson mass are displayed in Fig. 1.13.

The expected decays are listed in Tab. 1.2.

Diagram	**decay**
tree-level	$H \rightarrow f\bar{f}$
tree-level	$H \rightarrow W^+W^-$
tree-level	$H \rightarrow ZZ^{(*)}$
one-loop	$H \rightarrow gg$
one-loop	$H \rightarrow \gamma\gamma$
one-loop	$H \rightarrow Z\gamma$

Table 1.2: Higgs boson decays at LHC.)

For $m_H < 130$ GeV/c^2, the most dominant decay mode is expected to be into

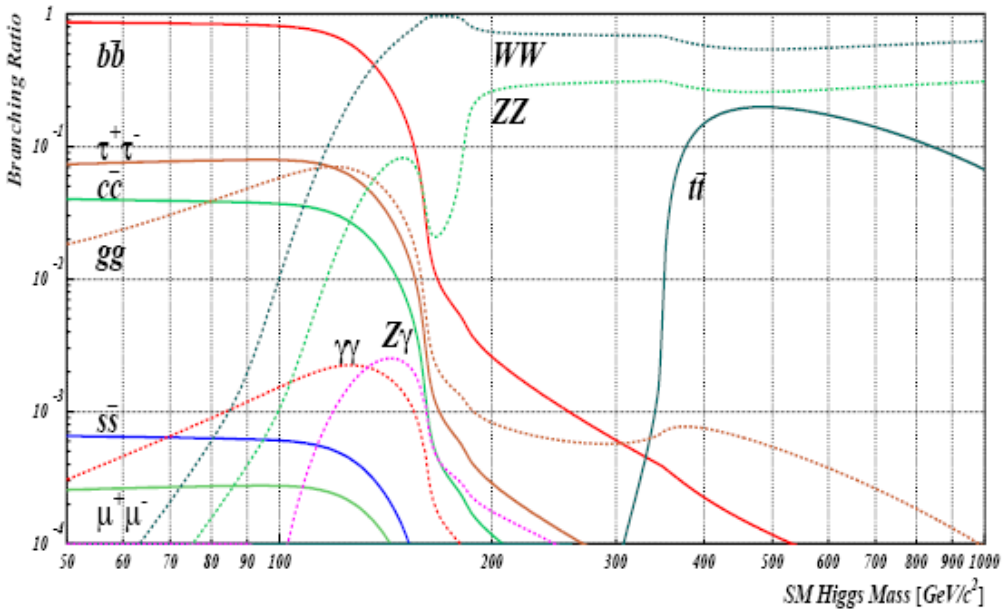

Figure 1.13: Branching ratio for Higgs boson decay channels.

a fermions pair (see diagram in Fig. 1.14).

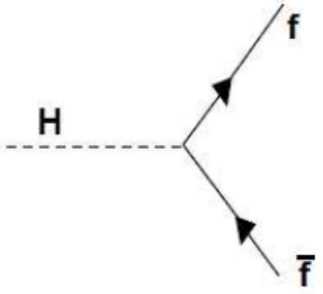

Figure 1.14: $H \to f\bar{f}$ decay channel.)

Due to the Yukawa coupling being proportional to the fermion mass,

$$BR(H \to f\bar{f}) \approx m_f^2$$

the most dominant decay mode is expected to be into $b\bar{b}$ pairs (branching ratio of about 85%), while the remaining 15% is quite equally divided into $H \to \tau^+\tau^-$, $H \to c\bar{c}$ and $H \to gg$.
In this mass range, the other decay modes are not significant, except for $H \to \gamma\gamma$ at the LHC: its branching ratio is notably lower (10^{-3}) but its signature is very clear (two high E_T isolated electromagnetic clusters, so the Higgs signal can be observed as a small but narrow peak over a large background). The Higgs decay into two photons is characterized, at the lower perturbative level, by a fermion or boson loop; the higher contribution comes from the W boson and t quark loops (see the diagram in Fig. 1.15).

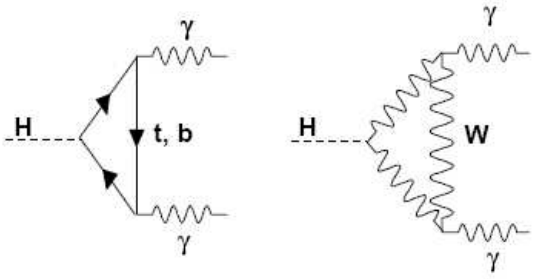

Figure 1.15: $H \to \gamma\gamma$ decay channel.)

For Higgs boson masses larger than 130 GeV/c^2, the two main decay modes are expected to be into W^+W^- and ZZ pairs (see Fig. 1.16). At lower Higgs masses, one of the vector bosons can be virtual, while at higher m_H values both vector bosons are on-shell. For instance, at $m_H \approx 160$ GeV/c^2 (WW on-shell channel open), the branching ratio into WW bosons becomes $\approx 100\%$ and the BR into $ZZ^{(*)}$ bosons goes down to 2%; when the decay channel into ZZ on-shell is open too, the $BR_{H\to ZZ}$ goes up again to 30%. For $m_H > 2m_t$, the $t\bar{t}$ decay mode becomes possible, but its branching ratio is never higher than 30%.

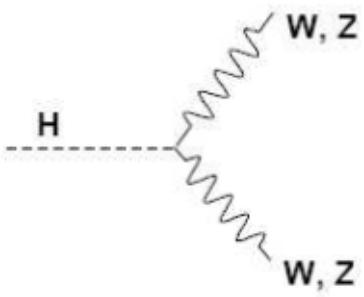

Figure 1.16: Higgs into two vector bosons decay channel.

Higgs boson search strategies. The Higgs boson search strategies can not rely just on the production rate, since the decay channel background plays a fundamental role. In particular, fully hadronic events are the most copious final states from Higgs decays but can not easily resolved when merged in QCD background; therefore, topologies with leptons or photons are preferred, even if they have a smaller branching ratio. Furthermore, the associated production with a leptonically decaying particle is searched for, despite a smaller cross section. Since the different processes have different cross sections depending on m_H, three regions of Higgs mass are defined with several strategies:

- low mass region ($m_H < 130\ GeV/c^2$)
  this region is the most probable to find Higgs boson in, as indicated by theoretical and experimental limits, but it is nevertheless the harder to be explored at LHC. The $b\bar{b}$ decay mode is the dominant one by more than one order of magnitude, but it is almost impossible to exploit it, due to the "overwhelming" QCD background. In fact, the total $b\bar{b}$ cross section at LHC is more than six order of magnitude higher than the expected signal. This is the reason of the importance of the search for the associated

production $t\bar{t}H$, $W^{\pm}H$ or ZH with the $H \to b\bar{b}$ decay followed by a leptonic decay of the accompanying particle. For instance, for a 115 GeV/c^2 Higgs boson mass, the WH cross section is about 2 pb but this kind of events can be efficiently extracted from the background by identifying the isolated charged lepton (e, μ) originated from the W decay (see Fig. 1.17);

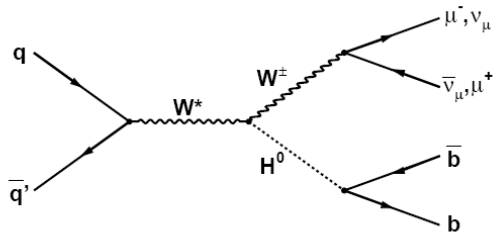

Figure 1.17: Feynman diagram for $q\bar{q} \to W^* \to W(\to \mu\nu_\mu)H(\to b\bar{b})$ process at tree-level.

The second decay channel $H \to t\bar{t}$ is difficult to be studied, because of the background given by $t\bar{t}$ and Drell-Yan $\tau^+\tau^-$ pair productions. A cleaner channel should be the decay $H \to \gamma\gamma$, but it has a very small cross section. The background for this channel comes from $\pi^0 \to \gamma\gamma$ decays with the two photons so much close one to each other to fake a single energetic γ. Anyway the signal-to-background ratio is 10^{-2}, so this channel is much more attractive than the $b\bar{b}$ channel. The two photons decay can be searched for also in association with a leptonic $t\bar{t}$ or $W^{\pm}$ decay, making this channel the most clear at LHC if the Higgs would be less than 150 GeV/c^2. To enhance the signal-to-background ratio for exactly this channel, an electromagnetic calorimeter with excellent performance is required.

- intermediate mass region (130 GeV/$c^2 < m_H < 2m_Z$)
  in this region the $b\bar{b}$ decay decreases with increasing $H \to VV^*$ (V = $W^{\pm}$ or Z); the most promising channels are $gg \to H \to WW^* \to l^+\nu l^+\bar{\nu}$ or $gg \to H \to ZZ^* \to l^+l^-l^+l^-$, with l=e or μ (see Fig. 1.18). The WW^* decay mode has to be extracted from a background mainly due to $qq \to WW$ continuum or $t\bar{t} \to bW^+\bar{b}W^-$ and $W^{\pm}t(b)$ associated production. On the other side, the fully leptonic decay $H \to ZZ^* \to 4l$ has the cleanest experimental signature, particularly in the four-muon channel. The signal selection is based on the identification of two opposite charged lepton pairs coming from a common vertex, requiring the invariant mass of one of the two pairs to be compatible with m_Z. The main irreducible background

is continuum ZZ^* production $q\bar{q} \rightarrow ZZ^* \rightarrow 4l$ together with reducible background $t\bar{t} \rightarrow 4l + X$ and $Zb\bar{b} \rightarrow 4l + X$: in the first case leptons come from $t \rightarrow Wb$ decay followed by $W \rightarrow l\nu$ and semileptonic b decay, in the second case two leptons are from $Z \rightarrow l\bar{l}$ and the other two from b quark decay chains. Chapter 5 of this work focuses on High Level Trigger studies for this $H \rightarrow ZZ^* \rightarrow 4l$ channel, with a 4 electrons final state;

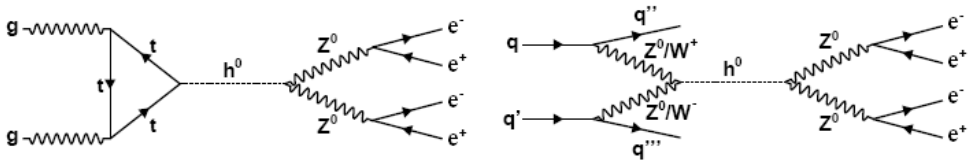

Figure 1.18: Feynman diagram for $H \rightarrow VV^*$ decays.

- high mass region ($m_H > 2m_Z$)
  the Higgs boson decays mainly into on-shell W^+W^- or ZZ pairs; the $H \rightarrow ZZ \rightarrow 4l$ channel has a smaller $q\bar{q} \rightarrow ZZ \rightarrow 4l$ background than in the intermediate mass region, the selection of the signal being facilitated by requiring both l^+l^- pair invariant masses close to m_Z, thus the Higgs into ZZ into 4 leptons channel is the so-called "gold" Higgs boson signature at LHC. For very large masses, $m_H > 600\ GeV/c^2$, other decay modes are used to supplement the gold channel, because the production cross section decreases significantly and the resonance peak of the four leptons becomes too broad and will no longer be visible. For this reason, the following decays of associated vector bosons are also exploited: $H \rightarrow Z(\rightarrow l^+l^-)Z(\rightarrow \nu\bar{\nu})$ or $H \rightarrow Z(\rightarrow l^+l^-)Z(\rightarrow q\bar{q})$ and $H \rightarrow W(\rightarrow l\nu)W(\rightarrow q\bar{q})$, whose vector boson hadronic decay has a greater branching ratio than the pure leptonic ones. The main background is from ZZ, ZW, WW and W(Z)q, and if neutrinos appear in the final states a high missing transverse energy will be the relevant signatures of the event.

At LHC the Higgs boson discovery will be possible, whatever its mass value may be in the range (100 GeV - 1 TeV) not yet explored.

1.3 The Quantum Chromodynamics

Quantum Chromodynamics (QCD) is the gauge field theory which describes the strong interactions of coloured quarks and gluons; it is based on the local symmetry group $SU(3)$ of colour and it is one of the components of the $SU(3)_C \otimes SU(2)_I \otimes U(1)_Y$ Standard Model.

1.3.1 The QCD Lagrangian

According to the Lie group theory (see Appendix A), the symmetry group $SU(3)_C$ has a fundamental representation r with dimension $d(r) = 3$ and an adjoint representation G with d(G) = 8. As for QCD, by common consent:

the matter fields are the quarks $q_f^i(x)$, 4-component Dirac spinors with spin $\frac{1}{2}$, where i (= 1,2,3) labels the colour and f (= u,d,s,c,b,t) the flavour. The quarks belong to the $SU(3)$ fundamental representation 3, the antiquarks belong to the fundamental representation $\bar{3}$;

the gauge fields are the Yang-Mills fields (gluons $G_\mu^a(x)$), bosons with spin 1, where a (= 1,..., 8) labels the colour. They belong to the adjoint representation G.

So we say that a quark of specific flavour comes in 3 colours and gluons come in 8 colours, while hadrons are colour-singlet combinations of quarks, anti-quarks and guons.
The (classical) Lagrangian describing the interactions of quarks and gluons is

$$L_{QCD} = -\frac{1}{4} F_{\mu\nu}^{(a)} F^{\mu\nu(a)} + \sum_f \bar{q}_f^i (i\gamma^\mu (D_\mu)_{ij} - m_f \delta_{ij}) q_f^j$$

f = flavour index

i, j = quark colour index

a = gluon colour index

$F_{\mu\nu}^{(a)} = \partial_\mu G_\nu^{(a)} - \partial_\nu G_\mu^{(a)} + g_3 F^{abc} G_{\mu,b} G_{\nu,c}$

$(D_\mu)_{ij} = \delta_{ij}\partial_\mu - i g_3 (t_r^a)_{ij} G_\mu^a$

g_3 is the QCD coupling constant and f^{abc} are the algebra structure constants

(t_r^a) are the algebra generators, 8 matrixes *3*x*3* obtainable from the Gell-Mann matrixes λ_a.

The $g_3 f^{abc} G^b_\mu G^c_\nu$ term is the nonabelian one: it divides QCD from QED and gives rise to the gluon self-interaction.

1.3.2 Jets in hadronic collisions

We have seen that QCD is the currently accepted theory of the strong interaction between particles (partons) that carry colour. The partons appear in the detector as "jets", that are "sprays" of particles as a result of parton hadronization. In hadronic collision, we can describe this hadronization with a simple fragmentation model: for example, the virtual gluon emission by the parent parton and the following gluon splitting to $q\bar{q}$ pairs, which form the colour-singlet hadron that can be measured.
Using the fragmentation model, the jet axis can be defined by a cluster of calorimeter cells[5] that minimize the $\vec{k_T}$ (transverse momentum) of the jet remnants. This means to require:

$$\sum_i \vec{k_{T_i}} = 0 \tag{1.29}$$

In projective geometry calorimeters, the jet can be defined also as a cluster of towers. In this way, it can be "converted" into an equivalent particle with its 4-momentum $p^\mu = (E, \vec{p})$, useful to calculate an invariant mass.
Moreover, if we represent the energy E_i of each calorimeter cell (i) as a particle with zero mass and if we introduce the unit vector $\widehat{n_i}$ pointing from the interaction vertex to cell i, we can define the vector

$$\vec{E_i} = E_i \widehat{n_i}$$

So jet can be seen in the rest of frame of the detector, as a set of these zero mass particles, one per calorimeter cell. This clearly does not imply that the jet has zero mass itself, because of the opening angles between the cells. In fact, the invariant mass of two zero-mass particles, with a θ angle between them, is

$$M^2_{12} = m^2_1 + m^2_2 + 2E_1E_2(1 - \cos\theta) = 2E_1E_2(1 - \cos\theta)$$

We can now present a few relations on jets kinematic. First, to form a jet from calorimeter cells we must apply Eq. 1.29 relative to the axis that defines the jet direction, that is transform the cells to the axis using an Euler rotation

[5] less often using the information from tracking chambers, but most of LEP experiments defined jets in this way

with two angles ϕ_{jet} and θ_{jet} (jet cluster coordinates):

$$\begin{pmatrix} -\sin\phi_{jet} & \cos\phi_{jet} & 0 \\ -\cos\theta_{jet}\cos\phi_{jet} & -\cos\theta_{jet}\sin\phi_{jet} & \sin\theta_{jet} \\ \sin\theta_{jet}\cos\phi_{jet} & \sin\theta_{jet}\sin\phi_{jet} & \cos\theta_{jet} \end{pmatrix}$$

Requiring the transverse components of the rotated momentum vectors to be separately set to zero, we obtain some relations involving the angles, like:

$$\tan\theta_{jet} = \frac{\sum E_{T_i}\sin\phi_i}{\sum E_{T_i}\cos\phi_i}$$

Moreover, if we consider the jet as a physical object identified by a 4-vector $(E_{jet}, \vec{p}_{jet})$, the angles can be defined in the laboratory with the usual definition, such as

$$\tan\theta_{jet} = \frac{p_{Tjet}}{p_{zjet}}$$

With some algebra , we establish a self-consistent prescription for turning a cluster of energy towers into a physical jet: the physical jet is now a particle with 4-momentum in the detector frame given by

$$p^{\mu}_{jet} = (E_{jet}, \vec{p_{jet}}) = (\sum_{i=1}^{Ntowers} E_i, \sum \vec{p_i}) \tag{1.30}$$

where

$$p_{xjet} = \sum_{i=1}^{Ntowers} E_{T_i}\cos\phi_i$$

$$p_{yjet} = \sum_{i=1}^{Ntowers} E_{T_i}\sin\phi_i$$

$$p_{xjet} = \sum_{i=1}^{Ntowers} E_{T_i}\sinh\eta_i$$

In particular, the transverse energy of a detected jet is a common way to characterize the hard scattering energy scale Q^2 for QCD collisions. To measure jet E_T we can use the relation

$$E_T \equiv \sum_{i=1}^{Ntowers} E_{T_i}$$

but there are other ways, more suitable to treat jets as collection of particles. For

example, we can use a relation where the definition of E_{jet} as given in Eq.1.30 is implied:

$$E_T \equiv E_{jet} \sin\theta_{jet}$$

In this way, $\cos\theta_{jet}$ can be calculated from the pseudorapidity η_{jet} (see paragraph 2.2.1 for the pseudorapidity definition), but because of the differences between p_T and E_T this latter definition should not be used in calculating the jet invariant mass.

Finally, is important to point out that a jet does not have a transverse mass, since the transverse mass is only defined when dealing with 2 (or more) 4-vectors. For a jet, an invariant mass can be defined, calculated from its transverse momentum and energy:

$$M^2_{jet} = E^2_{jet} + p^2_{jet} \equiv E^2_{Tjet} + p^2_{Tjet}$$

1.3.3 Jets at LHC

LHC will have a very "jetty" environment, since for initial state partons at low x there is dominance of gluon and sea quark interactions, with a large probability for additional jets from ISR and production of extra low p_T jets. Figure 1.19 presents the decomposition of the total jet cross section into the partonic processes for $p\bar{p}$ collisions at the Tevatron and pp collisions at the LHC in dependence of the scaling variable $x_T = 2p_T/\sqrt{s}$, and illustrates the differences in cross section contributions of the pdfs compared to measurements possible today.

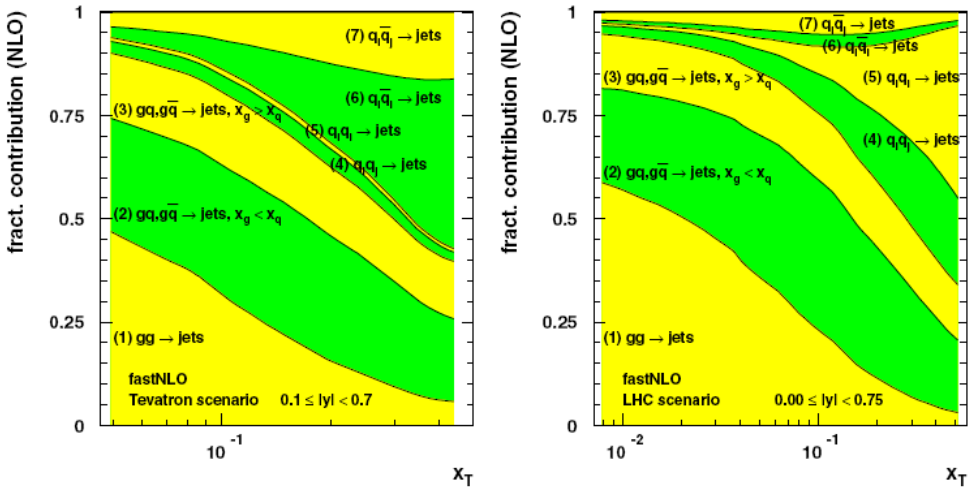

Figure 1.19: Decomposition of the total cross section into the partonic processes for $p\bar{p}$ collisions at the Tevatron and pp collisions at the LHC.

Jet clustering Algorithms. In order to re-establish a link between the particles that appear as collimated streams of hadrons in the detector and the hard process, clustering algorithms are defined to group particles that are supposed to come from the same hard parton into jets. The required ingredients of such a jet algorithm are: a distance measure to define the separation between objects, a procedure how to decide when objects are to be combined, and a recombination scheme explaining how to combine objects. In addition, it has to be specified how the list of input objects has been determined. Thus, clustering algorithms are needed to determine which calorimeter cell is to be included in the cluster, consistent to Eq. 1.29.
Two principal types of algorithms are in common use:
· cone-type algorithms, traditionally employed in hadron-hadron collisions, which cluster together objects that are close in angle around a high-energetic seed;
· clustering algorithms where iteratively objects which have the smallest distance of all pairwise combinations possible are combined; they have been predominantly used in e^+e^- and $e^\pm p$ collisions, first in the form of the Jade algorithm and nowadays as k_T algorithm.
Three principal jet reconstruction algorithms have been coded and studied for CMS: the iterative cone, the midpoint cone and the inclusive k_T jet algorithm.

Iterative cone algorithm: an E_T-ordered list of input objects (calorimeter towers or particles) is created. A cone of size R in η, ϕ space is cast around the input object having the largest transverse energy above a specified seed threshold. The objects inside the cone are then used to calculate a "proto-jet" direction and energy using the so-called E_T scheme[6]. The computed direction is used to seed a new proto-jet. The procedure is repeated until the energy of the proto-jet changes by less than 1% between iterations and the direction of the proto-jet changes by $\Delta R < 0.01$. When a stable proto-jet is found, all objects in the proto-jet are removed from the list of input objects and the stable proto-jet is added to the list of jets. The whole procedure is repeated until the list contains no more objects with an E_T above the seed threshold. The cone size and the seed threshold are parameters of the algorithm. When the algorithm is terminated, a different recombination scheme may be applied to jet constituents to define the final jet kinematic properties.

[6]massless jets are produced by equating the jet transverse momentum to the $\sum E_T$ of the constituents and then fixing the direction of the jet in one of two ways: 1) $\sin\theta = \sum E_T/E$, where E is the jet energy (usually used with cone algorithms), or 2) $\eta = \sum E_{T_i}\eta_i / \sum E_T$ and $\phi = \sum E_{T_i}\phi_i / \sum E_T$

Midpont-cone algorithm: it was designed to facilitate the splitting and merging of jets and also uses an iterative procedure to find stable cones (proto-jets) starting from the cones around objects with an E_T above a seed threshold. Unlike the iterative cone algorithm, no object is removed from the input list; this can result in overlapping proto-jets (a single input object may belong to several proto-jets) and to ensure the collinear and infrared safety of the algorithm, a second iteration of the list of stable jets is done. For every pair of proto-jets that are closer than the cone diameter, a midpoint is calculated as the direction of the combined momentum; these midpoints are then used as additional seeds to find more proto-jets. When all proto-jets are found, the splitting and merging procedure is applied, starting with the highest E_T proto-jet; if the proto-jet does not share objects with other proto-jets, it is defined as a jet and removed from the proto-jet list. Otherwise, the transverse energy shared with the highest E_T neighbor proto-jet is compared to the total transverse energy of this neighbor proto-jet and if the fraction is greater than f (typically 50%) the proto-jets are merged, otherwise the shared objects are individually assigned to the proto-jet that is closest in η, ϕ space. The procedure is repeated, again always starting with the highest E_T proto-jet, until no proto-jets are left. This algorithm implements the energy scheme to calculate the proto-jet properties but a different recombination scheme may be used for the final jet. The parameters of the algorithm include a seed threshold, a cone radius, a threshold f on the shared energy fraction for jet merging, and also a maximum number of proto-jets that are used to calculate midpoints.

Inclusive k_T algorithm: it is a cluster-based jet algorithm, where the cluster procedure starts with a list of input objects, stable particles or calorimeter cells. For each object i and each pair (i,j) the following distances are calculated

$$d_i = (E_{T,i})^2 R^2$$

$$d_{ij} = min(E_{T,i}^2, E_{T,j}^2) R_{ij}^2$$

with

$$R_{ij}^2 = (\eta_i - \eta_j)^2 + (\phi_i - \phi_j)^2$$

and R^2 a dimensionless parameter normally set to unity. The algorithm searches for the smallest d_i or d_{ij} and if a value of type d_{ij} is the smallest, the corresponding objects i and j are removed from the list of input objects. They are then merged using one of the recombination schemes listed below and filled as one new object into the list of input objects. If a distance

of type d_i is the smallest, the corresponding object i is removed from the list of input objects and filled into the list of final jets. The procedure is repeated until all objects are included in jets; the algorithm successively merges objects which have a distance $R_{ij} < R$.

1.4 Beyond SM

1.4.1 Search for new physics at LHC

Despite the good agreement between SM predictions and experimental evidences, there are both conceptual problems and phenomenological indications of new physics beyond it. For instance, particle mass and quantum numbers (such as electric charge, weak isospin, hypercharge and colours) are not explained by the Standard Model; moreover, there is no reason why leptons and quarks come in different flavours and why their electroweak interactions mix in such a peculiar way. All these arguments lead to the idea of more elementary constituents of matter than quarks and leptons.
Another crucial point is gravity: typical energy scales for quantum gravity are seventeen order of magnitude higher than the typical electroweak interactions. It seems unlikely that SM could valid up to such large energies without new physics, since there are no indications in it of why the typical weak scale of masses is so small relatively to the Planck mass.
Also, the Higgs sector itself is not satisfactory, since loop corrections to the Higgs mass are quadratically divergent and give rise to the so-called "naturality problem". If we recognize SM to be an effective theory, valid up to a certain energy scale Λ, it will be interesting to look at the relevant SM quantities upon this cut off scale. Moreover, the Standard Model appear to be founded on a too high number of arbitrary parameters: three independent gauge couplings, a possible CP-violating strong-interaction parameter, two independent masses for weak bosons and six quarks and three charged-leptons masses, three generalized Cabibbo weak-mixing angles and the CP-violating Kobayashi-Maskawa phase. Experiments are giving a strong evidence of neutrino oscillations: this would imply massive neutrinos and the violation of the family lepton number, leading to the existence of at least nine more arbitrary parameters and to the introduction of a more complicated mechanism for the generation of the neutrino masses with the SM. Among the several possible new theories and SM extensions, supersymmetry and extra-dimensions will be briefly considered.

Supersymmetry. It consists in assuming the existence of a new symmetry Q which transforms bosons to fermions, and vice versa. Since its associated operator links particles with different spin values, Q must carry a semi-entire spin, that is must be fermionic. A direct consequence of the new symmetry is that to each boson is associated a fermion and, by analogy, to each fermion is associated a boson. In a supersymmetric Standard Model, each fermion is coupled to a boson in a supersymmetric multiplet called "supermultiplet": to each lepton a so-called "slepton" is associated, to each quark a "squark", and so on (see Fig. 1.20). The simplest extension of the SM (Minimal Supersymmetric Standard Model, MSSM) assume the Higgs sector composed by two scalar doublets, with their fermionic partners.
This model has a useful consequence on the one-loop corrections to the Higgs mass: for suitable values of the coupling constants, the quadratic divergences disappear, due to fermionic degrees of freedom doubling (the fermionic loop is balanced by the "sfermionic"-loop).

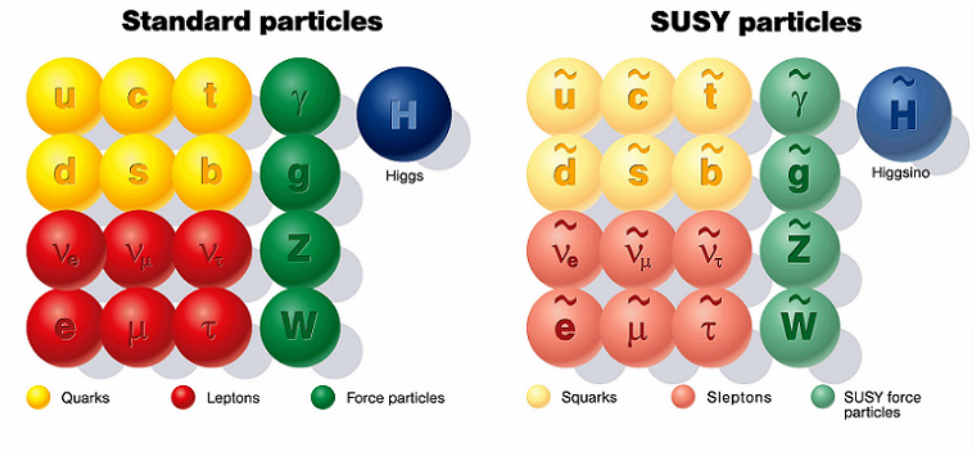

Figure 1.20: Particles of a SUpersymmetric Standard Model.

In order to implement the baryon (B) and lepton (L) number conservation, a new quantum number (R-parity) must be conserved and it is defined as

$$R = (-1)^{3B+L+2S}$$

where R = 1 for standard particles and R = -1 for their superpartners.
We must notice that superpartners of standard particles with the same mass should have been already detected in experiments but it did not happen; the supersymmetric particles search at LEP put lower limits on their masses (for instance, $m_{\tilde{f}} > 100$ GeV, $m_{\tilde{\gamma}} > 50$ GeV). For this reason, the supersymme-

try must be broken in a realistic theory, at a certain energy scale Λ_{SUSY}. The mechanism by which the supersymmetry is broken is the main difficulty of the supersymmetric model.

Extra-dimensions. A second SM extension is based on phenomenological theories involving the gravitation interaction: the general idea is to bring the gravity down to the weak interaction scale and to obtain the observed Planck mass scale as a result of a (4 + n)-dimensional world. The starting argument is that electroweak forces have been probed at distances $\approx \Lambda_{EW}^{-1}$, while gravitational forces have been investigated only to distances of about 1 cm, 33 orders of magnitude greater than the intrinsic energy scale of gravity ($\approx m_P^{-1}$). The idea is that changes could happen in between the two scales.
The existing proposed theories can be divided into different classes (flat compactified extra dimensions, warped extra dimensions) and each one can be further divided in two groups (gravitational extra dimensions, universal extra dimensions). For example, a gravitational extra dimensions scenario proposes that, in addition to the space-time dimensions we live in, there are n compact space dimensions accessible to the gravity but not to the other three fundamental forces. SM particles cannot freely propagate in (4 + n) dimensions but would be localized on the four-dimensional subspace (submanifold), whilst the fields propagating in the extra dimensions are gravitons. As a consequence, gravity manifests itself in our world as an extremely weak force.

Chapter 2

Experimental Framework

Modern physics still has a great number of open questions and the Standard Model itself does not give an answer to many of them. New experiments and new efforts must be provided by the scientific international community and in this context hadron colliders are particularly suitable for new physics search. The present chapter gives a brief description of the Large Hadron Collider, about to be started up at CERN, and focuses on the CMS experiment, one of the four detectors installed at LHC, giving a particular attention to the CMS Electromagnetic Calorimeter. Together with the experiment hardware aspects, the CMS software and the main CMS trigger features are also described.

2.1 The LHC

The first aim of the Large Hadron Collider (LHC) is to elucidate the nature of electroweak symmetry breaking for which the Higgs mechanism is presumed to be responsible. The experimental study of the Higgs mechanism can also shed light on the mathematical consistency of the SM at energy scales above ≈1 TeV, up to which SM is considered to be an effective theory; new symmetries or new forces or constituents could be discovered, and there is a high hope for discoveries that could bring toward a unified theory. For all these reasons, the TeV energy scale has to be investigated.

2.1.1 The LHC machine

The LHC will provide proton-proton collisions and has been designed to reach a sufficient high colliding protons energy and luminosity. LHC beam nominal energy is 7 TeV, with a center of mass energy of 14 TeV, while the design luminosity is of $\mathscr{L} = 10^{34}\ cm^{-2}\ s^{-1}$, that is a seven-fold increase in energy and

a hundred-fold increase in integrated luminosity over the current hadron collider experiments. LHC has been placed in the already existent LEP tunnel, a 26.7 km long tunnel with a diameter of 3.8 m; it is situated 50-175 m underground nearby the France-Switzerland border (see Fig. 2.1).

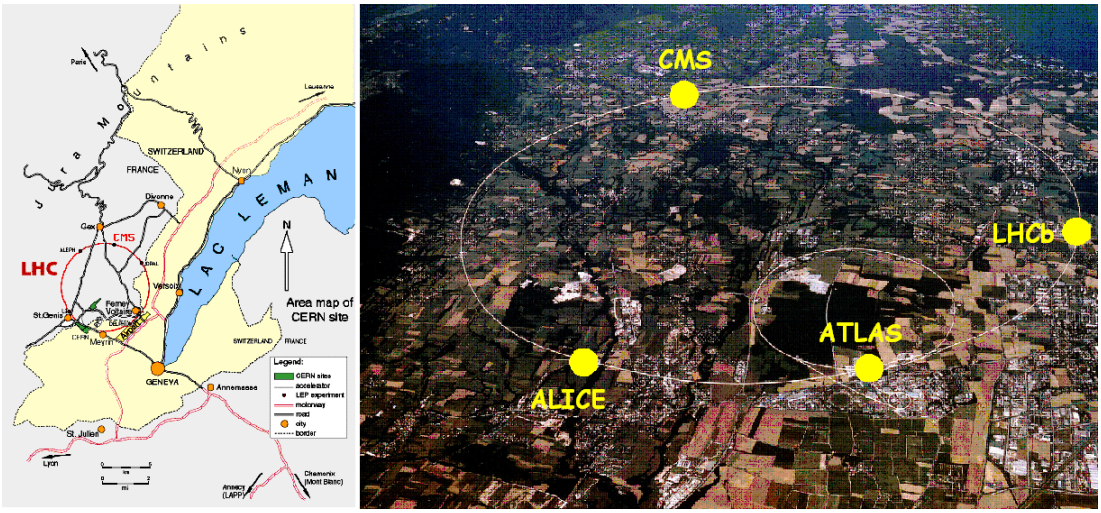

Figure 2.1: On the left, map of the CERN site with the LHC tunnel; on the right, aerial view of the same area, with the 4 experiments located at each interaction point.

Unlike LEP, the collisions will occur between particles of the same charge, so two separated beam pipes with two different magnetic field configurations are set up. The magnetic field of ≈8.4 T will be provided by 1232 superconducting dipoles operating at 1.9 K.
According to Eq. 2.1, luminosity depends on the Lorentz factor (γ), the revolution frequency (f), the number of bunches (k_B), the number of protons/bunch (N_p), the normalized transverse emittance (ϵ_n), the betatron function at the impact parameter (β^*), and the reduction factor due to the crossing angle (F).

$$\mathscr{L} = \frac{\gamma f k_B N_p^2}{4\pi\epsilon_n\beta^*} F \tag{2.1}$$

The ϵ_n design value is of 3.75 μm, while the other parameters value are listed in Tab. 2.1.

Protons will be delivered to LHC by an upgrade of the CERN existing facility (see Fig. 2.2): the bunches are formed in the 50 MeV LINAC, then accelerated up to 1.4 GeV in the Booster; the Proton Syncrotron (PS) will further accelerate them up to 26 GeV and the Super Proton Synchrotron (SPS) will inject them into the LHC at the initial energy of 450 GeV. This operation is repeated 12 times

		p-p	Pb-Pb	
Energy per nucleon	E	7	2.76	TeV
Dipole field at 7 TeV	B	8.33	8.33	T
Design luminosity	$\mathscr{L}$	10^{34}	10^{27}	$cm^{-2}s^{-1}$
Bunch separation (time)		25	100	ns
Number of bunches	k_B	2808	593	
Number of particles/bunch	N_p	$1.15 \cdot 10^{11}$	$7 \cdot 10^7$	
β value at IP	β^*	0.55	0.5	m
RMS beam radius at IP	$\sigma*$	16.7	15.9	μm
luminosity lifetime	τ_L	15	6	hr

Table 2.1: LHC machine main parameters.

for each counter-rotating beam and at each transfer, enough space has to be reserved to accommodate the rise time of the injection kickers. Finally, a longer gap is reserved for the rise time of the dump kicker by eliminating 1 PS batch. During the beam acceleration, the 25 ns spacing between proton bunches must be provided. The final bunches will have the nominal number of 10^{11} particles each, a very small transverse spread ($\sigma_x \approx \sigma_y \approx 15\mu m$) and will be 7.5 cm long in the beam direction at the collision points.

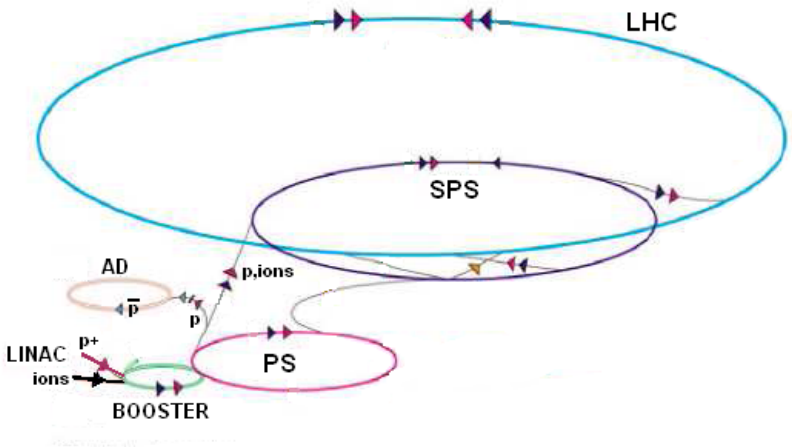

Figure 2.2: LHC pre-acceleration and injection facility.

Note that the design luminosity of $\mathscr{L} = 10^{34}\ cm^{-2}\ s^{-1}$ leads to around 20 proton-proton interactions per bunch crossing, that is ≈1 billion interactions per second, and corresponds to an integrated luminosity over one year of LHC running of ≈100 fb^{-1}. This value will be reached after an initial start-up phase at $10^{32}cm^{-2}s^{-1}$ and a so called "low luminosity" phase at $10^{33}cm^{-2}s^{-1}$, mainly

dedicated to tune the detector performances, search for new particles and b-physics studies. The commissioning of the LHC machine with beams is expected to start in the second half of 2008, with some machine development periods interleaved with data taking runs. See Tab. 2.2 for the expected evolution of the machine performance.

	pilot run	first physics
Number of bunches	$43 \rightarrow 156$	$936 \rightarrow 2808$
$\beta*$	18 m $\rightarrow$ 2 m	2 m $\rightarrow$ 0.55 m
Protons per bunch	$10^{10} \rightarrow 4 \cdot 10^{10}$	$4 \cdot 10^{10}$
Luminosity	$3 \cdot 10^{29} \rightarrow 2 \cdot 10^{31}$	$10^{32} \rightarrow 2 \cdot 10^{33}$
Integrated luminosity	10 pb^{-1}	< 5 fb^{-1}

Table 2.2: Expected evolution of LHC performance parameters from August 2008 on.

2.1.2 Physics requirements

The requirements on the LHC physics programme create several challenges from the experimental point of view. First, in order to investigate rare processes, a very high luminosity is needed: this causes a very high common QCD event rate[1] and an extremely dense particle environment (10^9 interactions per second). Therefore, a strong online event selection (*trigger*) is needed in order to reduce the event rate to the maximum data storage rate reachable with the existing device technology, that is of about 100 Hz (7 orders of magnitude less). See Section 2.4 for more details about the CMS trigger system.
An excellent time resolution is needed to distinguish events belonging to different bunch crossings, which are separated only by 25 ns: this brings major implications for the design of the readout and trigger systems.
Moreover, detectors must have fine granularity to separate particles very close in space, requiring a large number of detector channels and very sophisticated reconstruction algorithms. In fact, at the design luminosity, a mean of about 20 hard-core scattering collisions will be superimposed on the event of interest (*pile-up*): around 1000 charged particles will emerge from the interaction region every 25 ns and the products of an interaction under study may be confused with those from other interactions in the same bunch crossing. This large flux of particles also requires radiation-hard detectors and front-end electronics.
Finally, all the LHC physics programme considered (see Chapter 1), multi-purpose detectors should fulfill the following requirements:

[1] the total pp cross section at the LHC energy is estimated to be $\approx$ 100 mb

- good muon identification and momentum resolution over a wide range of momenta in the region $|\eta| < 2.5$, good dimuon mass resolution and the ability to determine the charge of muons with p $<$ 1 TeV/c;
- good charged particle momentum resolution and reconstruction efficiency in the inner tracker; pixel detectors close to the interaction region to provide an efficient τ and b tagging;
- good electromagnetic energy resolution, good diphoton and dielectron mass resolution, wide geometric coverage ($|\eta| < 2.5$), measurement of the direction of photons and correct localization of the primary interaction vertex, π^0 rejection and efficient photon and lepton isolation at high luminosity;
- good E_T^{miss} and dijet mass resolution, hadron calorimeters with a large hermetic geometrical coverage ($|\eta| < 5$) and with fine lateral segmentation ($\Delta\eta \times \Delta\phi < 0.1 \times 0.1$).

2.2 The CMS Experiment at LHC

The CMS experiment is placed at LHC interaction Point 5, in the french village of Cessy. Fig. 2.3 shows the CMS site, with the big surface hall where the detector has been assembled.

Figure 2.3: CMS site in Cessy (France).

The construction, installation and commissioning of CMS is progressing well toward the goal of being ready for collisions in Summer 2008.

The design of CMS meets the physics requirements previously detailed (see Section 2.1.2). The main distinguishing features of CMS are a high-field solenoid, a full silicon-based tracking system and a fully active scintillating crystals-based electromagnetic calorimeter. In particular, the choice of the magnetic field configuration has been done to provide a large bending power and so to measure precisely the momentum of charged particles. This leads to a careful choice of the magnets superconducting technology, described in Section 2.2.2. The overall CMS layout is shown in Fig. 2.4: it is made up by a 21.6 m long *barrel* and two *endcaps*; it has a diameter of about 15 m and a total weight of about 12500 tons.

The tracking volume is given by a cylinder of length 5.8 m and diameter 2.6 m, with 10 layers of silicon microstrips detectors and 3 layers of silicon pixel detectors close to the interaction region: this allows to deal with high track multiplicities and to improve the impact parameter measurement for charged-particle tracks. The tracker is surrounded by the ECAL, whose lead tungstate ($PbWO_4$) crystals cover a region in pseudorapidity up to $|\eta| < 3$; the scintillation light is detected by silicon avalanche photodiodes (APDs) in the barrel region and vacuum phototriodes (VPTs) in the endcap regions. A preshower system is also installed in front of the endcap ECAL for π^0 rejection. The ECAL is then surrounded by the hadron calorimeter (HCAL): it is divided into a brass/scintillator sampling central calorimeter, which covers a region up to $|\eta| < 3$, and an iron/quartz-fibre calorimeter, placed in the very forward region outside the magnet, in order to extend the pseudorapidity coverage up to $|\eta| < 5$. The tracker and calorimeters volume is embraced by the magnet solenoid, with a length of 13 m and an inner diameter of 5.9 m: to achieve a good momentum resolution a high magnetic field of 4 T has been chosen. The return field is large enough to saturate 1.5 m of iron and to allow 4 muon stations to be integrated. Each of them consists of several layers of aluminium drift tubes (DTs) in the barrel region and cathode strip chambers (CSCs) in the endcap region, together with resistive plate chambers (RPCs).
The thickness of the ECAL detector in radiation lengths is greater than 25 X_0, while HCAL thickness in interaction lengths varies with η from 7 to 11 λ_I. In the present section, the CMS detectors are described, while the next section better focuses on the Electromagnetic Calorimeter.

2.2.1 Coordinate system

The coordinate system adopted by CMS is a clockwise system, with the origin centered at the nominal collision point, the x-axis pointing radially toward the center of LHC, the y-axis pointing vertically upward and the z-axis pointing along

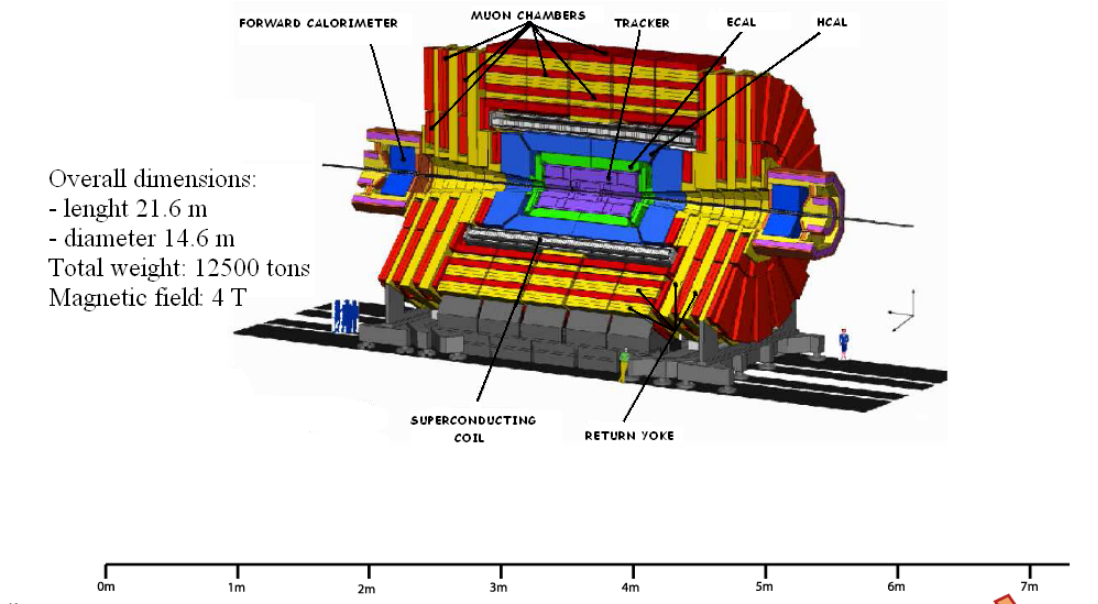

Figure 2.4: On top, CMS detector overall view; on bottom, transversal view of a CMS "slice".

the beam direction toward the Jura mountains. A spherical coordinate system is also used by the reconstruction algorithms: it is based on

- the distance r from the z-axis;
- the azimuthal angle ϕ, measured from the x-axis and the (x,y) plane;
- the polar angle θ, measured from the z-axis.

The momentum and energy measured transverse to the beam direction (p_T and E_T respectively), are computed from the x and y components.

Often, the *pseudorapidity* is also used: it is defined as

$$\eta = -\ln\ \tan\frac{\theta}{2}$$

and it changes additively under a boost transformation. In fact, the collision point can be boosted toward the beam direction and it is useful to use quantities which are invariant with respect to such a transformation. Rapidity is not invariant but changes only additively under a boost; it is defined as

$$y = \frac{1}{2}\ln\frac{E + p_z}{E - p_z}$$

and comes near to pseudorapidity for $p >> m$ (thus pseudorapidity can be seen as the rapidity of a particle with zero mass). Also, pseudorapidity only depends on θ so can be used for unknown mass and unknown momentum particles.

2.2.2 Magnet

The choice of a strong solenoidal magnetic field is due to the needed high resolution on the muon momentum measurement; current technologies put structural and geometrical limits on the construction of a very strong magnet, and this leads to a very compact design for the CMS detector. In fact, the required performance of the muon system, and hence the bending power, is defined by the narrow states decaying into muons and by the unambiguous determination of the sign for muons with a momentum of ≈ 1 TeV/c. This implies a momentum resolution of $\Delta p/p \approx 10\%$ at p = 1 TeV/c. The CMS magnet is a large superconducting magnet, with a favourable length/radius ratio in order to ensure good momentum resolution in the forward region as well. See Tab. 2.3 for the main magnet parameters.

Field	4 T
Inner bore	5.9 m
Length	12.9 m
Number of turns	2168
Current	19.5 kA

Table 2.3: CMS superconducting solenoid main parameters.

The magnetic flux is returned via a 1.8 m thick saturated iron yoke.
The CMS magnet is the largest element of the CMS detector, so it provides the principle support structure for all the barrel detector components: muon stations

outside the coil, calorimeters and tracker inside.

2.2.3 Muon system

Muons can be measured both by the inner tracker and by the muon chambers after the coil. The muon momentum is determined by the bending angle at the exit of the coils, but, up to p_T values of 200 GeV/c, the resolution on this measurement will be dominated by multiple scattering in the material before the first muon station. So, the best momentum resolution for low-momentum muons is obtained through the inner tracker measurements. For high-momentum muons, the combination of inner tracker and muon detector measurements can improve the resolution; the muon trajectory beyond the return yoke can be extrapolated back to the beam-line, thanks to the compensation of the bend before and after the coil.
The muon detectors have been designed in order to cover a very large surface and different radiation environments: in the barrel region, 4 active detector layers are arranged in cylinders interleaved with the iron plates of the yoke; the segmentation along the beam direction follows the 5 wheels of the yoke (labeled from YB-2 to YB+2) and the total thickness before the last muon station of ≈ 16 interaction lengths. In each of the endcaps, the muon stations are arranged in 4 disks perpendicular to the beam and in concentric rings, 3 rings in the innermost station and 2 in the others. In Fig. 2.5 the layout of one quarter of the CMS muon system for initial low luminosity running is shown:

At $\eta < 1.2$ (barrel region) the neutron induced background is small so the muon rate is low and the residual magnetic field in the chambers is low too; in this region, drift tube (DT) chambers are used. At greater η values, the muon rate and the magnetic field are higher, so cathode strip chambers (CSC) and resistive plate chambers (RPC) are used: the first cover a region up to $\eta < 2.4$, while the second are placed both in the barrel and in the endcap regions.
All the muon detectors contribute to the L1 trigger system, providing independent and complementary sources of information.

Drift Tube Chambers. Each of the 5 wheels of the barrel muon detector is divided into 12 sectors, each covering a 30° azimuthal angle. In each sector the chambers are organized in 4 layers (labeled MB1, MB2, MB3 and MB4). There are 12 chambers in each of the 3 inner layers; in the 4th layer the top and bottom sectors host 2 chambers each, thus leading to a total of 14 chambers per wheel in this outermost layer. In total, the barrel muon detector consists of 250 chambers. Each DT chamber consists of 12 layers of drift tubes (see Fig. 2.6).

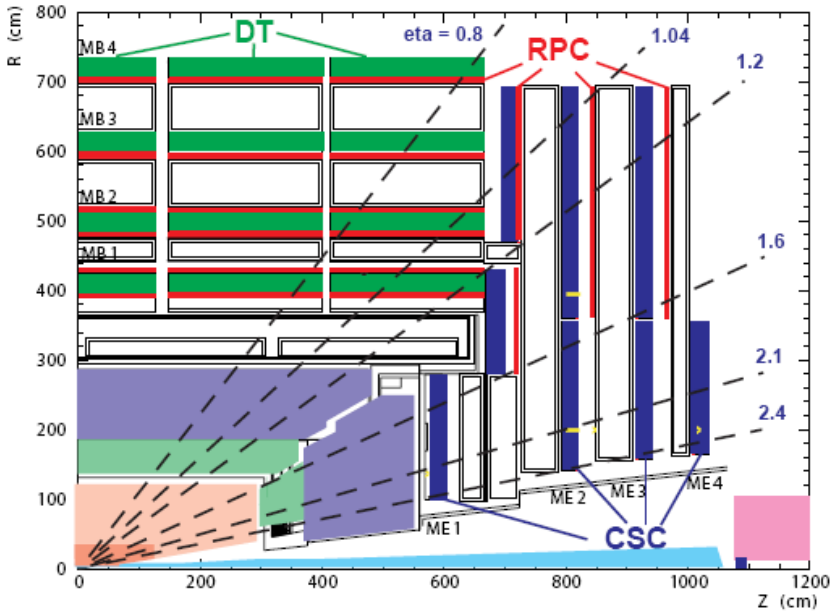

Figure 2.5: Layout of one quarter of the CMS muon system for initial low luminosity.

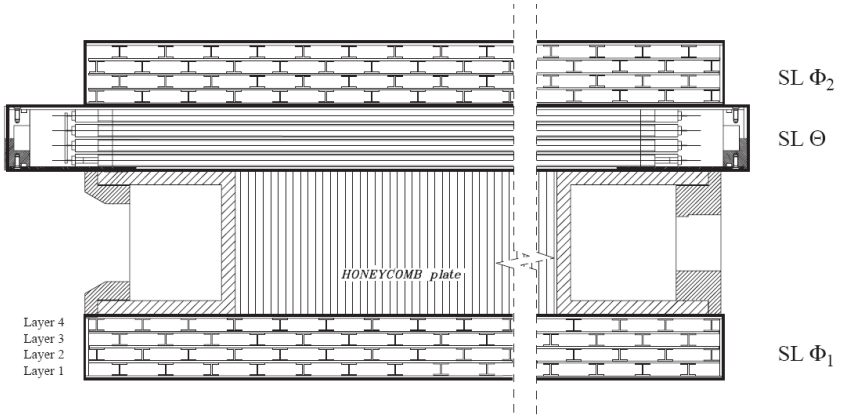

Figure 2.6: Layout of a DT chamber.

The DTs provide a precise track measurement in the bending plane; their maximum drift time is about 400 ns, with a time resolution of 5 ns. The overall spatial resolution is expected to be of 100 μm in the (R,ϕ) plane, and of 150 μm in the beam axis direction.
Each DT chamber has 1 or 2 RPCs coupled to it before installation, depending on the station: in stations MB1 and MB2, each package consists of 1 DT chamber sandwiched between 2 RPCs; in stations MB3 and MB4, each package comprises 1 DT chamber and 1 RPC, which is placed on the innermost side of the station. A high-p_T muon thus crosses up to 6 RPCs and 4 DT chambers, producing up to 44 measured points in the DT system from which a muon-track candidate can be built.

Cathode Strip Chambers. The CSCs cover a region with $0.9 < \eta < 2.4$: they can sustain a stronger and non uniform magnetic field and higher particle fluxes; each CSC is trapezoidal in shape and consists of 6 gas gaps, each gap having a plane of radial cathode strips and a plane of anode wires running almost perpendicularly to the strips (see Fig. 2.7). A charged particle traversing each plane of a chamber causes the gas ionization and subsequent electron avalanche: so a charge on the anode wire and an image charge on a group of cathode strips are produced. Each CSC measures the space coordinates (r, ϕ, z) in each of the 6 layers, with the strips having a spatial resolution of about 200 μm, and with an angular resolution in ϕ of about 10 $mrad$.
The first layer has 3 detector rings; the others have 18 detectors in the inner ring and 36 in the outer.

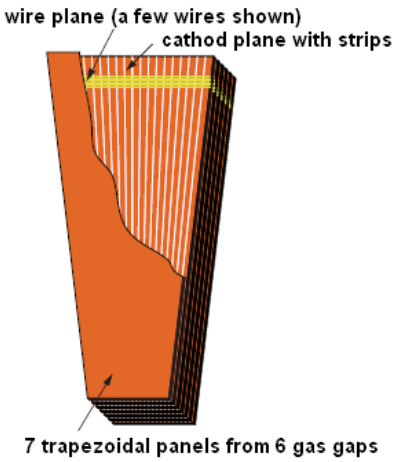

Figure 2.7: Schematic view of a CSC chamber.

Resistive Plate Chambers. Each RPC detector consists of a double-gap bakelite chamber, operating in avalanche mode to ensure good operation at high rates (up to 10 kHz/cm^2). RPCs are used both in the barrel and in the endcap regions, to complement the precision tracking given by DTs and RPCs; they provide a fast response, with an excellent time resolution of about 1 ns, but with a coarser position resolution than the DTs or CSCs. RPCs are then used for triggering purposes and for an unambiguous identification of the bunch crossing.

2.2.4 HCAL

The design of the hadron calorimeter is strongly influenced by the choice of the magnet parameters and by the fact that most of the CMS calorimetry is located inside the magnet coil. Since the goal of HCAL is to measure the energy and the direction of hadronic jets, as well as the missing transverse momentum, it must fully contain the hadronic shower. HCAL should also have a good transverse granularity and be completely hermetic. Thus, the HCAL design maximizes material inside the magnet coil. In particular:
· to have a quite short interaction length, brass has been chosen as absorber material; it is also easy to machine and non-magnetic;
· to maximize the amount of absorber before the magnet, the space devoted to the active medium is minimized; for instance, plastic scintillator tiles read out with embedded wavelength-shifting (WLS) fibres have been chosen for this purpose in the HCAL barrel and endcap regions.
HCAL is then a sampling calorimeter with 3.7 mm thick active layers of plastic scintillators alternated with 5 cm thick brass plate absorbers. It consists of:

Hadron barrel (HB), which covers the pseudorapidity region $-1.4 < \eta < 1.4$ and is made up of 2304 towers with a segmentation $\Delta\eta \times \Delta\phi = 0.087 \times 0.087$, in order to match the ECAL lateral granularity;

Hadron outer (HO), which is used to help the hadron shower containment and serve as a "tail catcher" placed outside the magnetic coil; HO consists of scintillators placed outside of the coil outer vacuum tank and covers the region $-1.26 < \eta < 1.26$. HO increases the effective thickness of the hadron calorimetry to over 10 interaction lengths, thus reducing the tails in the energy resolution function. The tiles are grouped in 30°-sectors, matching the ϕ segmentation of the DT chambers and are physically located inside the barrel muon system hence constrained by the geometry and construction of that system;

Hadron endcaps (HE), each one made up of 14 towers in η, with a 5° ϕ-segmentation; HE covers the pseudorapidity region $1.3 < |\eta| < 3.0$;

Hadron forward (HF), a steel/quartz fibre calorimeter placed at 11.2 m from the interaction point; it is a very forward calorimeter placed outside the magnet to extend the pseudorapidity coverage up to $|\eta| < 5.3$; the signal originates from Cerenkov light emitted in the quartz fibres and is then channeled by the fibres to photomultipliers.

The HCAL energy resolution is

$$\frac{\sigma E}{E} \approx 65\%\sqrt{E} \otimes 5\% \qquad (HB) \tag{2.2}$$

$$\frac{\sigma E}{E} \approx 85\%\sqrt{E} \otimes 5\% \qquad (HE) \tag{2.3}$$

$$\frac{\sigma E}{E} \approx 100\%\sqrt{E} \otimes 5\% \qquad (HF) \tag{2.4}$$

The granularity of the sampling in the 3 parts of the HCAL has been chosen such that the jet energy resolution, as a function of E_T, is similar in all 3 parts. This is illustrated in Fig. 2.8.

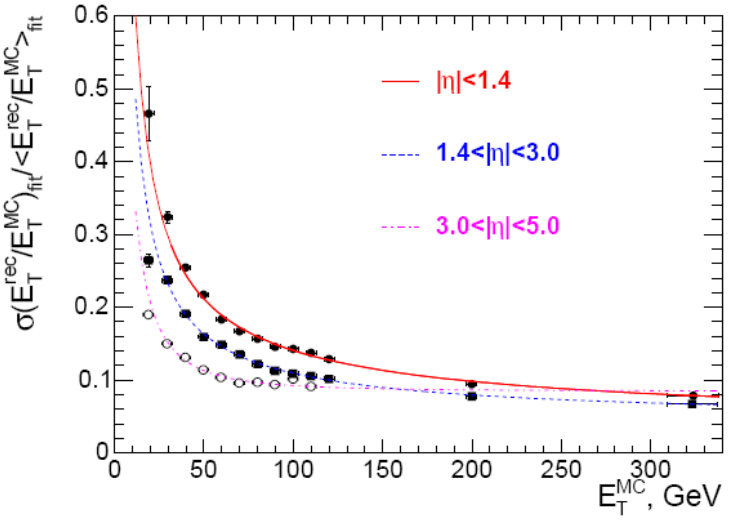

Figure 2.8: Jet transverse energy resolution as a function of the simulated jet transverse energy for barrel jets ($|\eta| < 1.4$), endcap jets ($1.4 < |\eta| < 3.0$) and very forward jets ($3.0 < |\eta| < 5.0$).

2.2.5 Tracker

The tracker is the CMS-subdetector closest to the interaction point. Its aim is the reconstruction of charged tracks and vertices, together with the measurement of charged particles p_T and the distinction between photons and electrons. The accurate vertex identification will be crucial for many physics cases, like for the Higgs boson search or the b-quark physics. In order to distinguish tracks and to provide a good precision in the extrapolation of the primary vertex, a high granularity is needed. Three regions can be delineated over the radius, with different granularities:
· at r≈10 cm, pixel detectors are placed (innermost part, covering a pseudorapidity range of $|\eta| < 2.4$) arranged in 3 layers in the barrel region and 3 disks in the endcaps; this is the region closest to the interaction vertex, where the particle flux is the highest ($\approx 10^7$/s). Each pixel covers an area of 100 × 150 μm^2; both the z-resolution and the ϕ-resolution are ≈ 15 μm;
· at $20 < r < 55$ cm (intermediate region), the particle flux is low enough to enable the use of silicon microstrip detectors with a minimum cell size of 10 cm × 80 μm; they are arranged in 5 cylinders in the barrel and 10 disks in the endcap;
· in the outermost region ($r > 55$ cm), the particle flux has dropped sufficiently to allow use of larger-pitch silicon microstrips with a maximum cell size of 25 cm × 180 μm.
See Fig. 2.9 for a tracker layout representation.

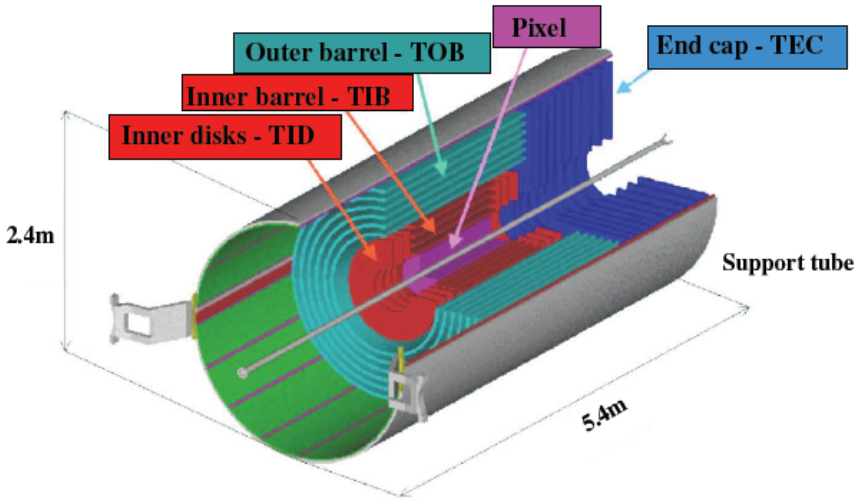

Figure 2.9: Layout of tracker detector.

The outer radius of the CMS tracker extends to nearly 110 cm, and its total

length is approximately 540 cm. The barrel part is separated into an Inner and an Outer Barrel: to avoid too shallow track crossing angles, the Inner Barrel is shorter than the Outer Barrel, and there are 3 additional Inner Disks in the transition region between the barrel and the endcap parts, on each side of the Inner Barrel. The total area of the pixel detector is $\approx 1\ m^2$, while the total area of the silicon strip detectors is 200 m^2. The inner tracker comprises 66 million pixels and 9.6 million silicon strips.

Please note that one of the major constraints of a tracker system design is to reduce the amount of material (as much as possible) in front of the calorimeters. Fig. 2.10 shows the CMS tracker *material budget*: it represents the main source of errors in accurate calorimetric measurements, for instance affecting the detector resolution in the Higgs search as for channels with electrons or photons in the final state ($H \to \gamma\gamma$; $H \to ZZ \to 4e$).

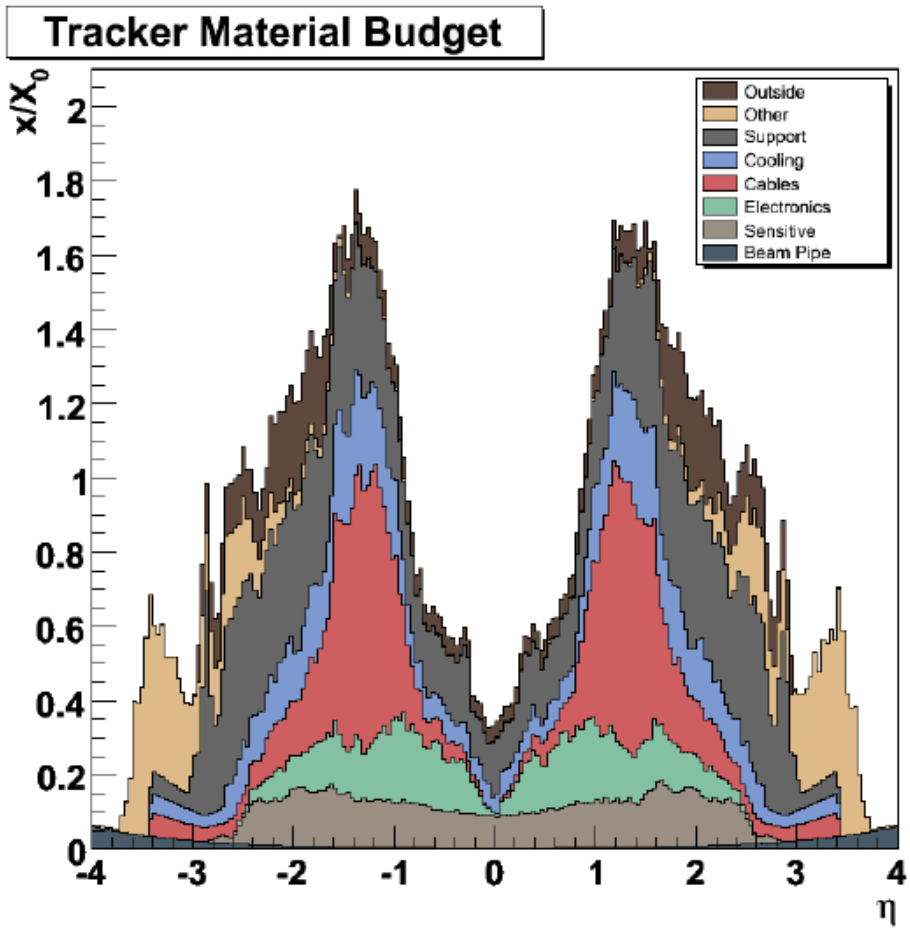

Figure 2.10: CMS tracker material budget distribution.

2.3 ECAL

The Electromagnetic Calorimeter (ECAL) is a hermetic, homogeneous calorimeter divided into a barrel part, made up of 61200 lead tungstate ($PbWO_4$) crystals, and two endcaps, with 7324 crystals each. In the present section ECAL layout, crystals and photodetectors are described, while its performance is deepened in Chapter 3 and its calibration and energy resolution are described in Chapter 4.

2.3.1 ECAL geometry

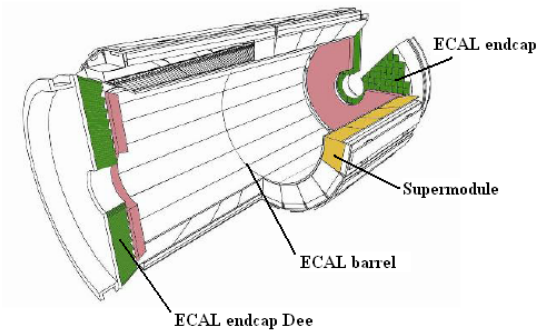

Figure 2.11: ECAL geometrical configuration.

In Fig. 2.11 and 2.12 the ECAL geometrical configuration and the transverse section are shown.

ECAL barrel layout. The barrel section (EB) has a length of about 3 m, an inner radius of 1.29 m and an outer radius of 1.75 m: it is structured as 36 identical "supermodules" (see Fig. 2.13), each covering half the barrel length and corresponding to a pseudorapidity interval of $|\eta| < 1.479$.

There are 18 supermodules in each half barrel, each covering 20° in ϕ and resulting in a total of 61200 crystals. The truncated pyramid shaped crystals are mounted in a quasi-projective geometry, so that their axes are tilted at 3° with respect to the line from the nominal vertex position, in both the ϕ and η projections (see Fig. 2.14).

The ECAL barrel granularity is of

$$\Delta\eta \times \Delta\phi = \ 0.0174 \times 0.0174$$

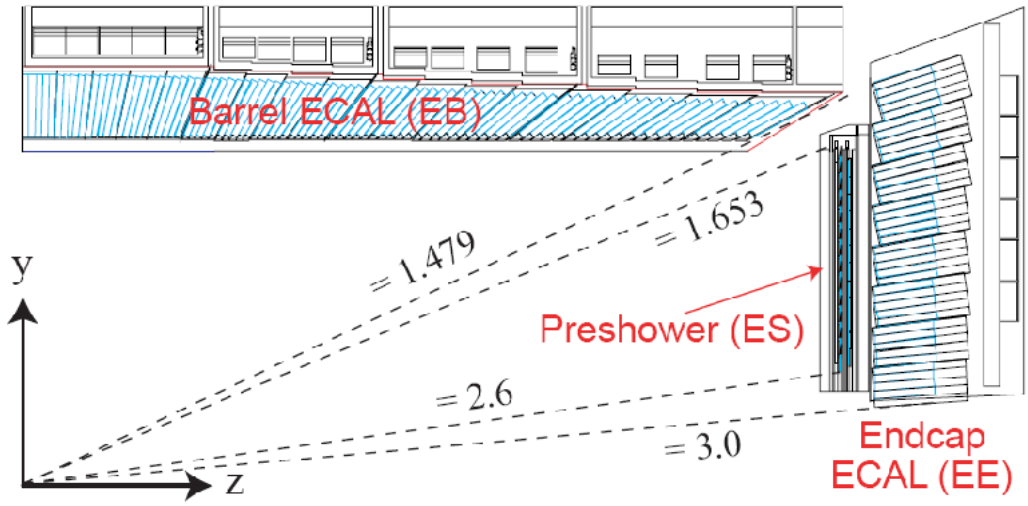

Figure 2.12: ECAL transverse section.

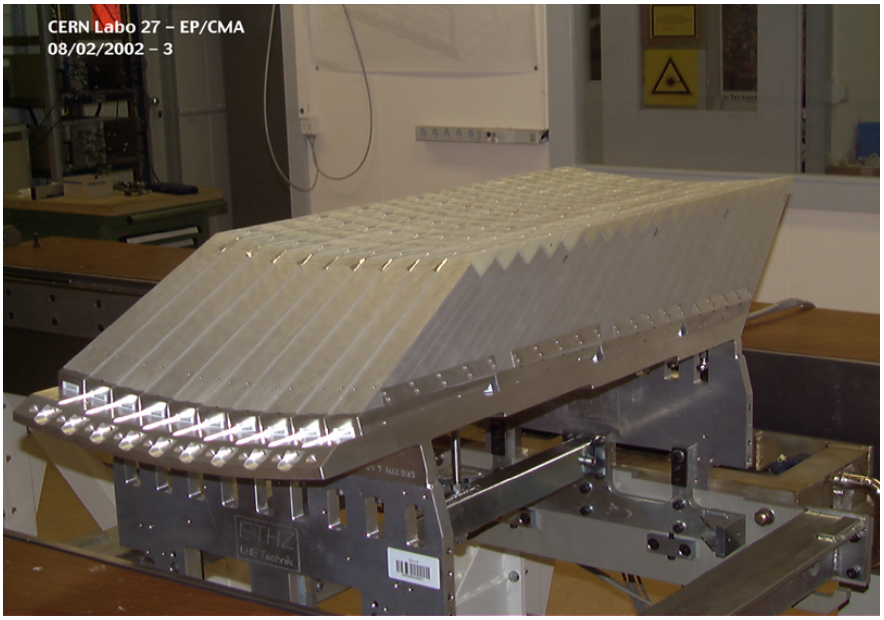

Figure 2.13: An ECAL supermodule.

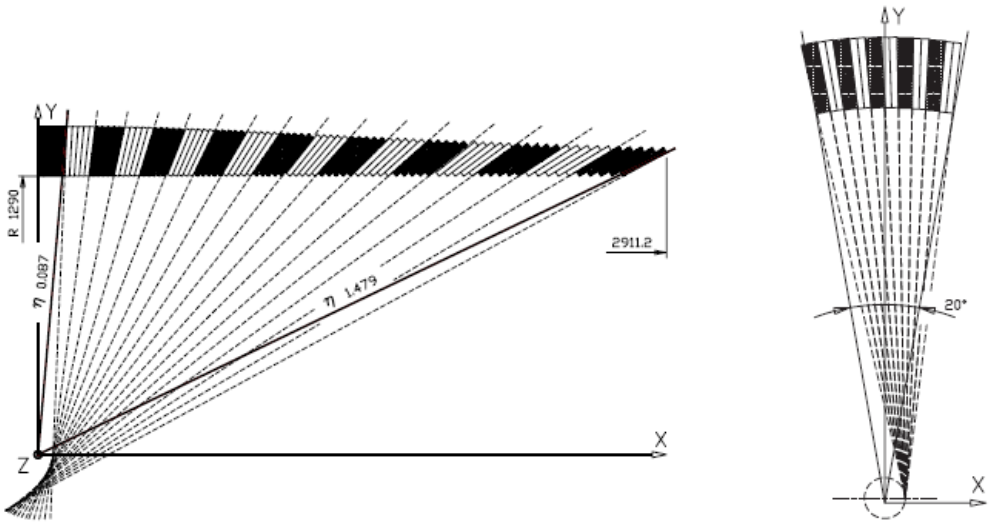

Figure 2.14: Crystals tilt in η (left) and in ϕ (right).

In fact, each crystal covers 1° in $\Delta\phi$ and $\Delta\eta$ and has a front face cross-section of $\approx 22{\times}22\ mm^2$; its length is about 230 mm, corresponding to 25.8 X_0.
Moreover, the crystals are contained in a thin-walled glass-fibre alveola structures (called "submodules") with 5 pairs of crystals each. The η extent of the submodule corresponds to a trigger tower. To reduce the number of different type of crystals, the crystals in each submodule have the same shape and there are 17 pairs of shapes in total. The submodules are then assembled into modules and there are 4 modules in each supermodule separated by aluminium webs.

ECAL endcap layout. The endcaps (EE) are placed at 3.14 m from the vertex and cover a pseudorapidity range of $1.479 < |\eta| < 3.0$; this location takes into account the estimated shift toward the interaction point by 2.6 cm when the magnetic field will be switched on. Each endcap is structured as a "Dee" consisting of semi-circular aluminium plates with structural units of 5x5 crystals, known as "supercrystals", placed in carbon-fibre alveola. There are 138 standard supercrystals and 18 special partial supercrystals on the inner and outer circumference. The endcap crystals, like the barrel crystals, off-point from the nominal vertex position, but the angle varies with η and they are arranged in an x-y grid (not a $\eta - \phi$ grid). All crystals are identical, with a front face cross section of 28.6x28.6 mm^2 and a length of 220 mm (24.7 X_0). The ECAL endcap granularity

is of

$$\Delta\eta \times \Delta\phi = \ 0.05 \times 0.05$$

Preshower detector (ES). A preshower device is placed in front of the crystal calorimeter over much of the endcap pseudorapidity range. The principal aim of the ES is to identify neutral pions in the endcaps within a fiducial region $1.653 < |\eta| < 2.6$, and to help the identification of electrons against minimum ionizing particles, improving the position determination of electrons and photons with its superior granularity. The ES is a sampling calorimeter with 2 layers: lead radiators initiate electromagnetic showers from incoming photons/electrons, whilst silicon strip sensors placed after each radiator measure the energy deposited and the transverse shower profiles.

2.3.2 The ECAL signal

Lead tungstate crystals. Lead tungstate crystals ($PbWO_4$) are used because their properties are an appropriate choice for operation at LHC. In Tab. 2.4 some $PbWO_4$ characteristics are compared to other scintillators.

	$PbWO_4$	NaI(Tl)	BGO
density (g/cm^3)	8.28	3.67	7.13
radiation length (cm)	0.89	2.59	1.12
Molière radius (cm)	2.2	4.5	2.4
maximum emission (nm)	420	410	480
emission time (ns)	5-15	250	300

Table 2.4: $PbWO_4$ compared to other scintillators.

ECAL crystals (see Fig. 2.15) are characterized by
· a high density (8.3 g/cm^3) and a short radiation length (0.89 cm), leading to a compact calorimeter; in fact, with crystals about 23 cm long, a depth of 25.8 X_0 is ensured; for instance, a 1.5 TeV photon gives a shower whose maximum expansion is at about 11.4 cm;
· a small *Molière* radius (2.2 cm), thus giving a good shower lateral containment and a fine granularity, leading to an excellent angular resolution;
· a scintillation decay time of the same order of magnitude as the LHC bunch crossing time, so about 95% of the light is emitted in 25 ns [2];
· a relatively low light output limited by a considerable quenching effect: at room

[2] in fact, $PbWO_4$ light decay time has three components (5 ns, 15 ns, 100 ns), with a respective amplitude of 39%, 60% and 1%

temperature the crystal emits 50-80 photons per MeV, its longitudinal transmission is of about 70%, thus 35-56 photons/MeV can reach the crystal back surface and only about 4.5 photoelectrons per MeV are finally collected by the photodetectors, due to the smaller surface coverage;
· a blue-green scintillation emitted light, with a broad maximum at 420 nm; moreover, due to the same quenching effect, the light output varies with temperature (-1.9% per °C at 18°C), so a cooling system is needed to extract the heat dissipated by the front end electronics and keep the crystal temperature stable within $\pm 0.05°C$.

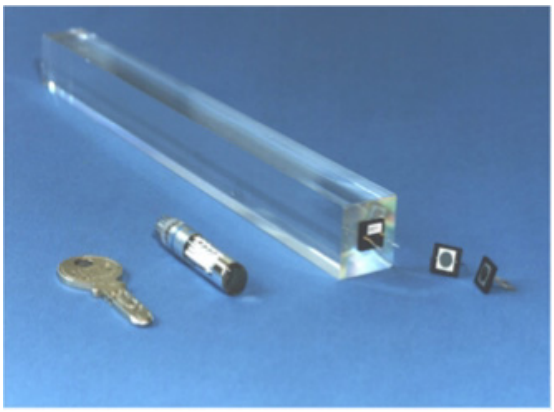

Figure 2.15: Picture of an ECAL barrel crystal.

In Fig. 2.16 the $PbWO_4$ emission spectrum is shown.

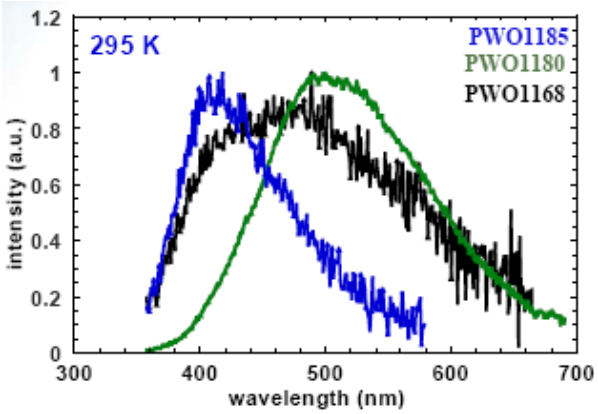

Figure 2.16: $PbWO_4$ emission spectrum: it is peaked at about 440 nm, as a result of the two main emission band (blue light at 420 nm and green light at 500 nm) superimposed.

To exploit the total internal reflection for optimum light collection on the photodetector, the crystals are polished after machining, on all but one side for EB crystals. Since the truncated pyramidal shape makes the light collection non-uniform along the crystal length, the needed uniformity is achieved by depolishing one lateral face. On the contrary, for endcap crystals the light collection is naturally more uniform because the crystal geometry is nearly parallelepipedic.

Photodetectors. Due to the crystals low light yield, the choice of the readout devices used to extract the crystal signal become very important. Photodetectors with an internal gain are needed, in order to give a first amplification stage for the signal before the injection in the electronic readout chain. Nevertheless, due to the strong magnetic field, photomultiplier could not be used: Avalanche Photo Diode (APD) are instead used in the barrel region, Vacuum Photo Triode (VPT) in the endcap one. Two different devices are needed in order to face up the different radiation level and magnetic field conditions.
The use of ADPs presents several advantages: they are fast detectors (≈2 ns of rise time), they have a very good quantum efficiency of 70%-80% around λ= 420 nm and they are higly insensitive to the magnetic field. They are compact devices (overall thickness of 2 mm) with a high radiation resistance, and can be manifactured in large quantities with a small spread in the performance parameters. Each APD has an active area of 5x5 mm^2, so two are glued to the back of each crystal. The APD basic structure is shown in Fig. 2.17.

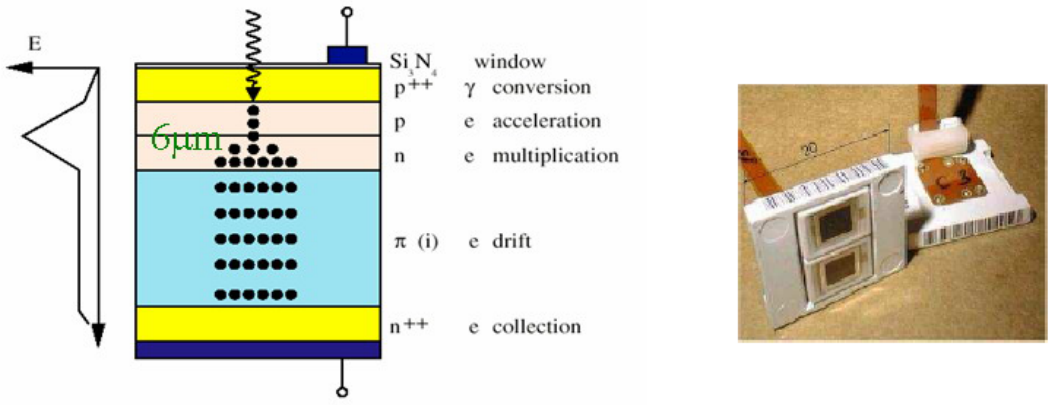

Figure 2.17: On the left, structure of a barrel APD; on the right, pair of APDs to be installed on a crystal rear face.

The light enters via a Si_3N_4 window p^+ and passes through a photocatode, that is a p^{++} layer with a thickness of 2μm. The photon is then absorbed in the

p layer behind, where electron-hole pairs are generated if the photon energy is higher than the gap energy[3]. The conversion region thickness has been chosen in order to optimize the quantum efficiency for 500 nm incident light. The photoelectron enters the p-n transition which leads to the drift; an amplification stage takes then place in the n volume through the avalanche ionization (field of about 100 kV/cm), with a gain tunable between 50 and 200. The charge crosses an intrinsic drift region and is collected by the n^{++} cathode. The APD is supplied by a reverse voltage: by changing its value, the charge multiplication gain can vary from 0 to 200, but the optimum gain to operate with the CMS front-end electronics sits between 50 and 100; it will be fixed at G = 50 during the experiment data taking. Not only the $PbWO_4$ light yield, but also the APD gain is temperature dependent: for this reason, one tenth of the APD pairs glued to the crystals has a sensor for the temperature measurement.

The APDs used in the barrel are insufficiently radiation-hard to be used also in the endcap region, where VPTs are employed. The VPT basic structure is shown in Fig. 2.18.

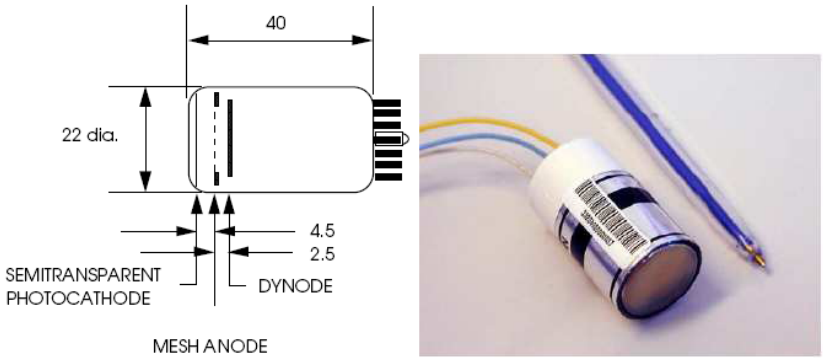

Figure 2.18: On the left, structure of an endcap VPT; on the right, picture of a VPT detector.

The photocatode is semitransparent and made of a radiation-hard glass: the photoelectrons produced are accelerated by an ultra fine mess (199 wires/mm) placed 4-5 mm far from the photocatode, and impact on a dynode producing secondary electrons (emission factor of about 20). The secondary electrons are attracted back to the anode with a total effective gain greater than 8. The VPTs lower quantum efficiency with respect to the APDs is compensated by a larger active area of about 280 mm^2, so that the total detector response is almost the same for barrel and endcap regions.

[3] 1.12 eV for Si

Trigger Tower and readout electronics. The signal produced by photodetectors is amplified and then digitized, passing through 3 different boards as shown in Fig. 2.19. The basic building block of the readout electronics is a 5x5

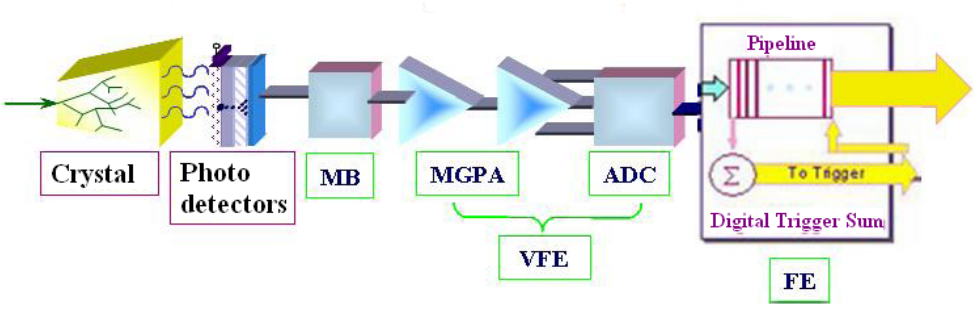

Figure 2.19: ECAL readout chain, from the crystal light emission to the digitized signal.

array of crystals, called *trigger tower* in the barrel, or supercrystal in the endcap, and is made up of 1 Mother Board (MB), a Low Voltage Regulator Board (LVRB), 5 Very Front End (VFE) boards and 1 Front End (FE) card. A trigger tower covers a region of $\Delta\eta \times \Delta\phi = 0.087 \times 0.087$.
The Mother Board is a totally passive board located beneath the cooling system for the electronics; it is necessary to route the signals from the photodetectors to the VFE cards, to distribute high voltage to the photodetectors, and to distribute low voltage to the VFE cards (see Fig. 2.20). Each supermodule contains 68 MBs connected to the photodetectors of 25 crystals via kapton flexible-print cables. In addition, signals for temperature monitoring thermistors are routed from the sensor capsule to the VFE cards.

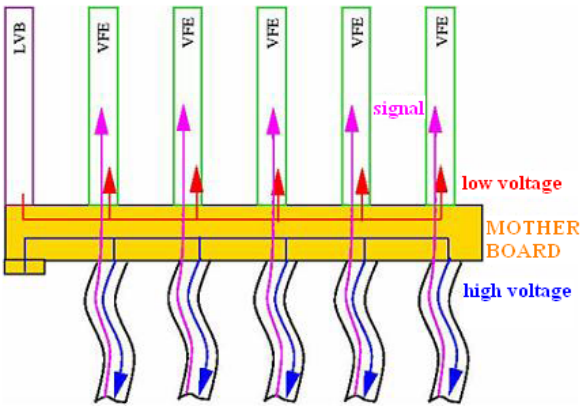

Figure 2.20: ECAL Mother Board.

The LVRBs are connected directly to the external Low Voltage power supplies which sit in the CMS racks attached to the outside of the CMS iron yoke, approximately 20 metres from the supermodule. Each LVRB contains radiation-hard voltage regulators which provide the 2.5 V needed by the front end electronics. This regulated 2.5 V is distributed to the FE card by a small connector on the LVRB, and to the 5 VFE cards in a trigger tower via the MB.

The VFE board is needed to amplify the signal and convert it from analog to digital, using very fast components (40 MHz) compatible with the 25 ns time that separates two LHC bunch crossings. Each VFE contains amplification and digitization for the signals from 5 crystals adjacent in ϕ. As can be seen in Fig. 2.21, the VFE consists of a Multi Gain Pre-Amplifier (MGPA) and a custom designed 12-bit Analog to Digital Converter (ADC). The MGPA contains a preamplifier and 3 parallel gain stages (1, 6, 12) which process the sensor signals; the signals are then routed to 3 ADCs, which digitize the three inputs in parallel and determine whether each channel has saturated. The output will come from the channel which has the highest gain and was not saturated: the output signal is a 12 bit word, with 2 additional bits giving the information on the chosen gain.

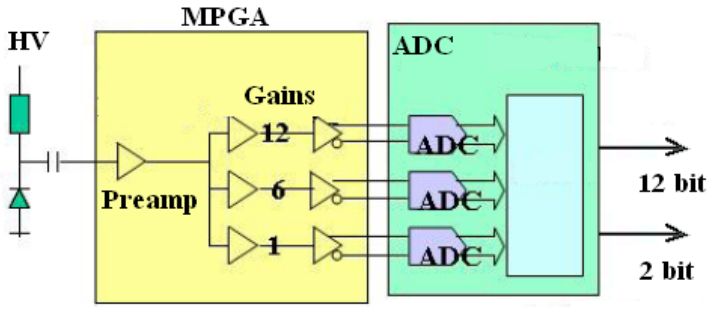

Figure 2.21: Simplified structure of a VFE.

For instance, in Tab. 2.5 some ADC-to-MeV conversions are shown, together with the corresponding MPGA and APD gains.

gain G_{MPGA}	gain G_{APD}	conversion
12	50	1 ADC = 40 MeV
12	200	1 ADC = 9 MeV

Table 2.5: ADC counts-to-MeV conversions for two different gain combinations.

The signals from the 5 VFEs are collected on the FE card. Here
· the data are buffered until a Level-1 trigger is received, and then the sampled

data are transmitted to the ECAL off detector electronics (the amount of data which is transferred is configurable, but typically consists of 10 ADC samples around the beam crossing);
· the samples from a group of 5 channels (called a strip) are summed at 40 MHz;
· the samples from the 5 strips (all 25 channels) are summed and transmitted to the calorimeter trigger.
Data are transferred to the L1-trigger after a conversion in light signals, since optical fibres are used for the transmission.
In Fig. 2.22, a Trigger Tower is shown, together with the pictures of a MB and VFE.

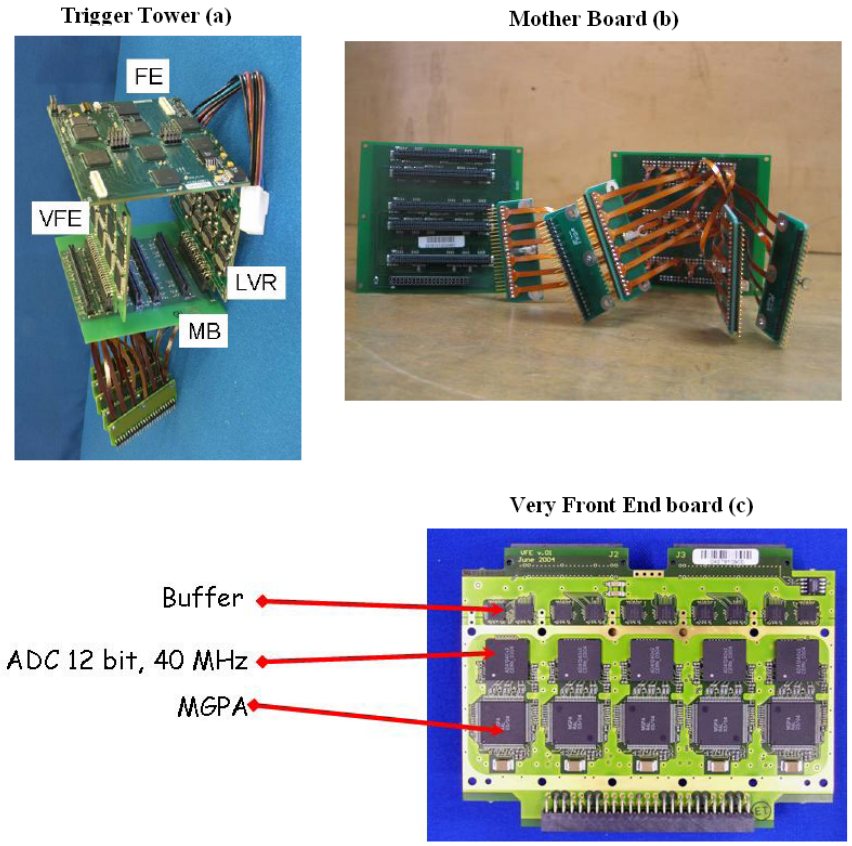

Figure 2.22: ECAL Trigger Tower (a); picture of a MB front and rear sides (b); picture of a VFE (c).

2.4 CMS Trigger and data acquisition

At the LHC expected energy and instantaneous luminosity, the interaction rate ($\approx$ 40 MHz) leads to $\approx 10^9$ interactions/sec, that is orders of magnitude larger than what can be reasonably archived for later off-line analysis. In fact, data from only about 10^2 crossings/sec can be written to archival media. For this reason a very good online selection must be provided and a selectivity of nearly 10^{-7} with respect to the active bunch crossings at the LHC has to be achieved. In the CMS design, this selection is performed in two physical steps: the *Level-1 Trigger* and the *High Level Trigger* (HLT). The L1 Trigger is based on processors which perform fast selections ($\approx$ 3 μs) for each 25-ns crossing; it is built of mostly custom-made hardware and it performs detector analysis in a coarse-grained scale. On the contrary, the HLT can operate on longer timescales and it is basically a processor farm which inspects the events that have already passed the L1 trigger and executes software algorithms. In fact, a key feature of the CMS Data Acquisition is the absence of a Level 2 intermediate trigger stage. For this reason, CMS HLT had not been implemented in multiple physics steps (for instance, a Level-2 and Level-3 steps, as for the ATLAS experiment); in this way, the full event information is available to a fully programmable processor, but the farm must also sustain a higher event rate on input and must provide more significant CPU sources. In Fig.2.23 the data flow in the CMS trigger and data acquisition system is shown.

In this section, L1 trigger and HLT are described; then, a particular attention is given to the calorimeter trigger.

2.4.1 Level 1 Trigger versus High Level Trigger

The total time allocated for the L1 trigger decision to keep or discard data from a particular beam crossing is 3.2 μs. This time includes the transit time for signals from the front-end electronics to reach the services cavern housing the Level-1 trigger logic and return back to the detector front-end electronics. During this time, the detector data must be held in buffers, while trigger data is collected from the front-end electronics and decisions are performed. The Level-1 triggers involve the calorimetry and muon systems, as well as some correlation of information between these systems. The Level-1 decision is based on the presence of "trigger primitive" objects such as photons, electrons, muons, and jets above set E_T or p_T thresholds. It also employs global sums of E_T and E_T^{miss}. Reduced-granularity and reduced-resolution data are used to form trigger objects. The L1 trigger will reduce event rates from 40 MHz to 100 kHz (design value); at startup, the rate

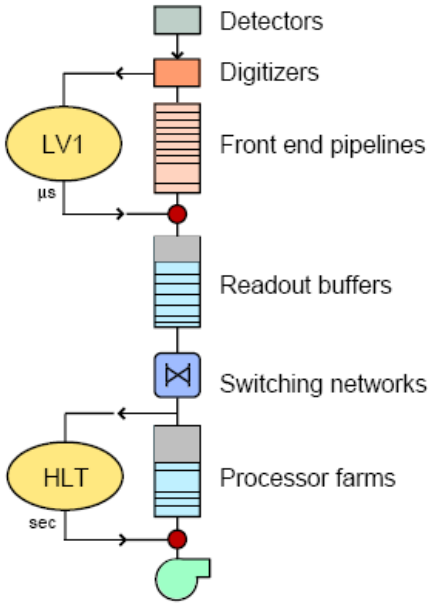

Figure 2.23: Data flow in the CMS Trigger/DAQ system. The software-based High-Level Trigger filters via the Data Acquisition system (DAQ) the events passing hardware-based Level-1 trigger. Time axis goes from upside down.

will be limited to 50 kHz.
The HLT *pc* farm runs the reconstruction algorithms and performs more sophisticated selections to reduce event rates furthermore, up to 100 Hz. The use of a processor farm for all selections beyond Level-1 allows maximal benefit to be taken from the evolution of computing technology. Flexibility is maximized, since there is complete freedom in the selection of the data to access, as well as in the sophistication of the algorithms. The HLT code is developed starting from the idea of partial reconstruction: rather than reconstruct all possible objects in an event, whenever possible only those objects and regions of the detector that are actually needed are reconstructed. Moreover, since events are to be discarded as soon as possible many virtual trigger levels are provided: calorimeter and muon information are used, followed by use of the tracker pixel data and finally the use of the full event information (including full tracking). HLT selection can then be seen as a sequence of filters of increasing complexity, using the information of calorimeters, pixel association and track reconstruction.

2.4.2 The Electromagnetic Calorimeter Trigger

The ECAL front end electronics is in charge of
· amplifying and shaping the signal from the sensors;

· digitizing the signal at 40 MHz;
· using the digitized data to calculate trigger primitives for in the Level-1 Trigger decision;
· buffering the data until receipt of the Level-1 trigger decision;
· transmitting the data to the off-detector electronics for insertion in the CMS data stream.
The building block of the front end electronics is the Trigger Tower, already described in section 2.3.2. At each bunch crossing, trigger primitive generation are first started in the Front End boards, and then finalized and synchronized in an electronic board (called Trigger Concentration Card, TCC) before transmission to the regional calorimeter trigger. Each trigger primitive refers to a single trigger tower and consists of the summed transverse energy deposited in the tower (8 bits)[4], plus a compactness bit which characterizes the lateral extension of the electromagnetic shower ("fine grain veto"). The encoded trigger primitives are time aligned and stored in the TCC during the Level-1 latency for subsequent reading: each TCC collects trigger data from 68 FE boards in the barrel (corresponding to a supermodule), and from 48 FE boards in the endcaps, corresponding to the inner or outer part of a 20° sector. Finally, trigger primitives are sent to the Level-1 regional calorimeter trigger, where together with HCAL trigger primitives, the electron/photon and jets candidates are computed as well as the total transverse energy.

2.4.3 Calorimeter towers: ECAL plus HCAL

Readout cells in HCAL are arranged in a tower pattern in η, ϕ space, projective to the nominal interaction point. The cells in the barrel region have a segmentation of $\Delta\eta \times \Delta\phi = 0.087 \times 0.087$, becoming progressively larger in the endcap and forward regions. Since the ECAL granularity is much finer than HCAL, calorimeter towers (ECAL plus HCAL) are formed by addition of signals in η, ϕ bins corresponding to individual HCAL cells. In total there are 4176 such towers, which when unfolded, may be represented in a "lego" plot (see Fig. 2.24 where the overall segmentation of HCAL is illustrated in a lego plot of a simulated multi-jet event).

[4]in the barrel, the trigger tower is divided into 5 ϕ-oriented strips, whose energy deposits are summed by the FE board trigger pipeline to give the total transverse energy of the tower, called the main trigger primitive

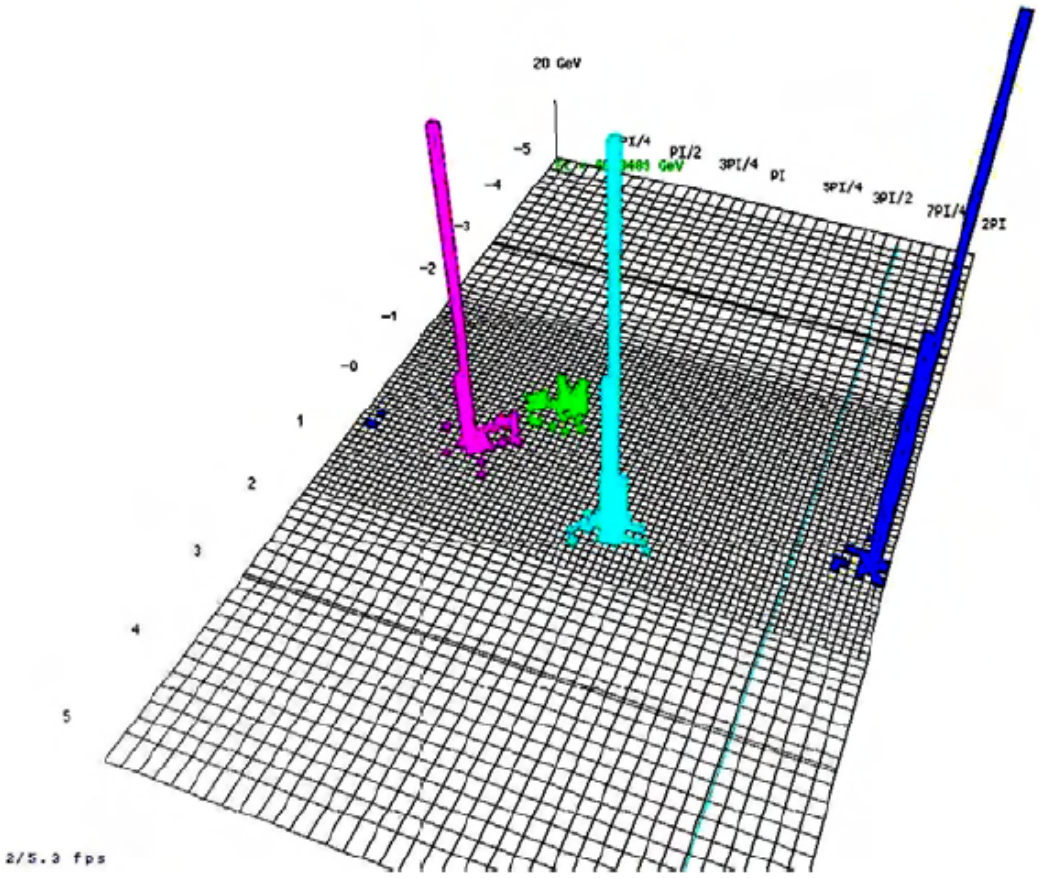

Figure 2.24: Lego plot of a simulated multi-jet event in HCAL.

2.4.4 Global Calorimeter Trigger

As already seen, local calorimeter trigger information refers to energy depositions in the trigger towers of the electromagnetic and hadron calorimeters. The Regional Calorimeter Trigger uses the trigger primitives to find candidate electrons or photons, jets and isolated hadrons from the decay of τs and to calculate transverse energy sums in different detector regions. The jet trigger uses the transverse energy sums of 12x12 electromagnetic and hadronic trigger towers covering a region of $\Delta\eta \times \Delta\phi = 1.04 \times 1.04$. τ-jets are distinguished from normal jets by requiring that none of the nine 4x4 sub-regions have a τ-veto bit set, where a τ-veto bit is set on if there are more than two active towers in the 4x4 sub-region. All calorimeter trigger objects described so far are forwarded to the Global Calorimeter Trigger, which sorts the electrons or photons, τs and jets according to energy and quality, and sends the four objects with the highest rank in each category to the Global Trigger. Furthermore, it determines the total and missing transverse energies as well as eight numbers representing jet multiplicities for eight different transverse energy thresholds, two of which are reserved for the forward region, and sends them to the Global Trigger.
The input for the physics trigger algorithm calculations are the trigger objects ordered by rank: an algorithm is defined as a logic combination of the trigger objects together with a set of energy or momentum thresholds, windows in η and/or ϕ and topological conditions. All threshold and space parameters, except for some exceptions, are only applied at the Global Trigger stage. The L1 decision is taken by applying a final OR to the (128) calculated algorithm bits.

2.5 CMS Software

The simulation tools, the calibration, alignment and reconstruction algorithms needed to process CMS data and to perform analysis have been implemented in a collection of software referred to as `CMSSW`. It is built around a Framework, an Event Data Model, and Services; its high-level goals are to process and select events inside the High Level Trigger Farm, to deliver the results to experimenters and to provide tools to analyse the processed information and to produce physics results. In the present section, an overview of `CMSSW` is given, together with a brief description of the event simulation and detector visualization tools.

2.5.1 CMS software architecture

The CMS software is characterized by:

- an application *Framework*, customizable for each of the computing environments; it defines the top level abstractions, their behavior and collaboration patterns. It comprises two components: a set of classes that capture CMS specific concepts like detector components and event features, and a control policy that orchestrates the instances of those classes taking care of the flow of control, module scheduling, input/output, etc;

- physics software *modules* with clearly defined interfaces that can be plugged into the framework; they can be plugged into the application framework at run time, independently of the computing environment, and do not communicate with each other directly but only through the data access protocols that are part of the framework itself;

- *services* and utility toolkits that can be used by any of the physics modules; there are two major categories of services: physics type services (histogrammers, fitters, mathematical algorithms, geometry and physics calculation routines) and computer services (data access, inter module communication, user interface, etc.).

The CMS Framework takes care of flow of control, event data model and conditions management, while the Event Data Model (EDM) is centered around the `Event`: it is a "container" to hold all data taken during a triggered physics event as well as all data derived from the taken data. Events are processed by passing the Event through a sequence of modules; the exact sequence of modules is specified by the user through the configuration file: the same file tells the framework executable (`cmsRun`) which data to use, which modules to run, which parameter settings to use for the modules and in what order to run them. When an Event is passed to a module, that module can get data from the Event and put data back into the Event; moreover, when data is put into the Event, the provenance information about the module that created the data will be stored with the data into the Event. The purpose of a module is to allow independent development and verification of distinct elements of triggering, simulation, reconstruction, and analysis. Such modules are not allowed to communicate directly with each other, but they communicate only through the Event.
Here is a (possibly non-exhaustive) list of framework module types:
- event data producers (`EDProducers`), used in triggering, reconstruction, and simulation; they put data products into the Event;
- filter (`EDFilters`), used in triggering to control the flow of processing for the trigger lists;
- analysers (`EDAnalyzers`), which do not modify the event data, but can use it

to create histograms or other event summaries.

2.5.2 Event Simulation

The detailed CMS detector and physics simulation is currently based on the `GEANT4` simulation toolkit and the CMS framework and event model. `GEANT4` provides a rich set of physics processes describing electromagnetic and hadronic interactions in detail; it also provides tools for modelling the full CMS detector geometry and the interfaces required for retrieving information from particle tracking through these detectors and the magnetic field. The simulation is implemented for all CMS detectors in both the central region (Tracker, Calorimeters and Muon Systems) and in the forward regions, including the field map from the 4 T solenoid. The full simulation program implements the sensitive detector behavior, track selection mechanisms, hit collection and digitization (i.e. detector response).

The detailed simulation workflow is as follows:

1. an appropriate Monte Carlo event generator is provided to produce data samples of interest and the generator software is run (see Appendix B); the output data (known as `Gen`) are in HepMC format (GenEvents in HepMC are based on the natural structure of an event, i.e. vertices with ingoing and outgoing particles);

2. Gen data are validated and a configuration `GEANT4` simulation is provided with generator events as input; data produced are known as `Sim` and contain persistent hits in the sensitive detectors;

3. after the Sim data validation, they are used as input to the subsequent digitization step, allowing for pile-up; this step converts hits into digitizations (also known as `Digi`) which correspond to the output of the CMS electronics. The digitization step constitutes the simulation of the electronic readout used to acquire data by the detector and Data Acquisition systems: starting from the hit positions, it simulates energy losses in the sensitive detectors and produces an output that needs to be as close as possible to real data coming from CMS; finally, information from the generation stage (for instance, particle type and momentum) is preserved in the digitization step.

The subsequent step, performed on DigiEvents, is reconstruction.

2.5.3 Event selection and reconstruction

Reconstruction with "real" data is the operation of constructing physics quantities from the raw data collected in the experiment. As a software process, reconstruction can be performed on generated events as a procedure of data reduction useful for further data analysis.
The process can be divided into 3 steps:

local reconstruction within an individual detector module, which uses as input real data from the Data Acquisition system or simulated data representing the real data; in either case, these data are the so-called Digis. The output from the local reconstruction process are the RecHits, reconstructed hits; in the ECAL, they identify position, time of arrival and energy of localized electromagnetic energy depositions (calorimetric clusters); RecHits are added to the Event, and used as the input to the global reconstruction;

global reconstruction within a whole detector, it uses the objects created in the local reconstruction within a single detector module and combines them with the objects arising from other modules of the same subdetector to produce further objects which represent the best measurement from that subdetector. Information from different subdetectors are not combined, yet. For example, the Calorimetric Towers (CaloTowers) are provided, matching clusters in ECAL and HCAL to produce a projective tower in the calorimetry system; once again, the objects produced are added to the event;

combination of reconstructed objects to produce higher-level objects based on the complete CMS detector. For instance, electron candidates from the Calorimeter system are matched to tracks in the Tracker system: the success of the matching of an ECAL "supercluster" to hits in the pixel detector flags the candidate as an electron, otherwise, the candidate is flagged as a photon; then the selection of electrons uses full track reconstruction, seeded from the pixel hits obtained by the matching step.

The reconstruction process output data are known as Reco.

Please note that the same code is used to run both the offline reconstruction and the High-Level Trigger selection. In general, the algorithms are the same, while the parameters used for the two use cases are different: for offline reconstruction, a global approach is used, in which all the detector parts are analysed and reconstructed with the best available set of parameters, without constraints on the processing time (at least to first approximation). When the same code

is used in the HLT, the set of parameters is optimized to give the best reconstruction within reasonable processing time, and the reconstruction is regional, i.e. only the regions of the detector from which a Level-1 trigger was received are considered.

Chapter 3

ECAL performance with cosmic muons

ECAL was installed inside the CMS detector during fall 2007; as soon as final cabling was completed, a data taking campaign has been started: each detector has been integrated into the final Data Acquisition System, in order to collect cosmic muon data. Cosmic-ray muons can be sources of background for the main physics channels under study, but they are important and can be used for many purposes, like alignment, calibration, location and identification of noisy channels, understanding of triggers, test of the real data workflow (mostly when beam is not available).
Thus, "cosmic runs" with cosmic-ray muons in the CMS cavern have been performed in spring 2008: a first GRUMM in March (Global RUn Mid March), a CRUZET I (Cosmic RUn at ZEro Tesla) in May, a CRUZET II at the beginning of June and a CRUZET III at the beginning of July. I participated in the CRUZET I data taking and I contributed to the analysis of cosmics events, as a member of the "ECAL Prompt Feedback Analysis Group".
During CRUZET, all CMS detectors were almost fully readout, except the ECAL Endcaps (still to be commissioned). In almost all the runs the trigger was provided by the muon system and by an ECAL top-bottom configuration; a few runs were triggered exclusively by ECAL or HCAL (see Table 3.1 and Fig. 3.1).
Focusing on ECAL, the whole barrel has been fully readout for most of the time, that is 36/36 supermodules. Aside from some High Voltage issues, ECAL readout was efficient through CRUZET and a successful "prompt" analysis was performed with more than 50 million cosmics events processed. To be mentioned that during cosmics data taking the ECAL barrel was operated at High Voltage gain 200[1],

[1] 1 ADC = 9 MeV

instead of 50, to be able to detect cosmic muons.

detector	triggering configuration
DT	all wheels; sectors 3 or 4 or 5 or 9 or 10 or 11, at least 2 chambers
ECAL	EB+ or EB- ; (4 OR 5)&(14 OR 15)
RPC	YB0 or YB1; 10 or 11 or 12 or 1 or 2 or 3, at least 3 rolls
CSC	ME1+, 4+; almost all chambers

Table 3.1: CRUZET I triggering details

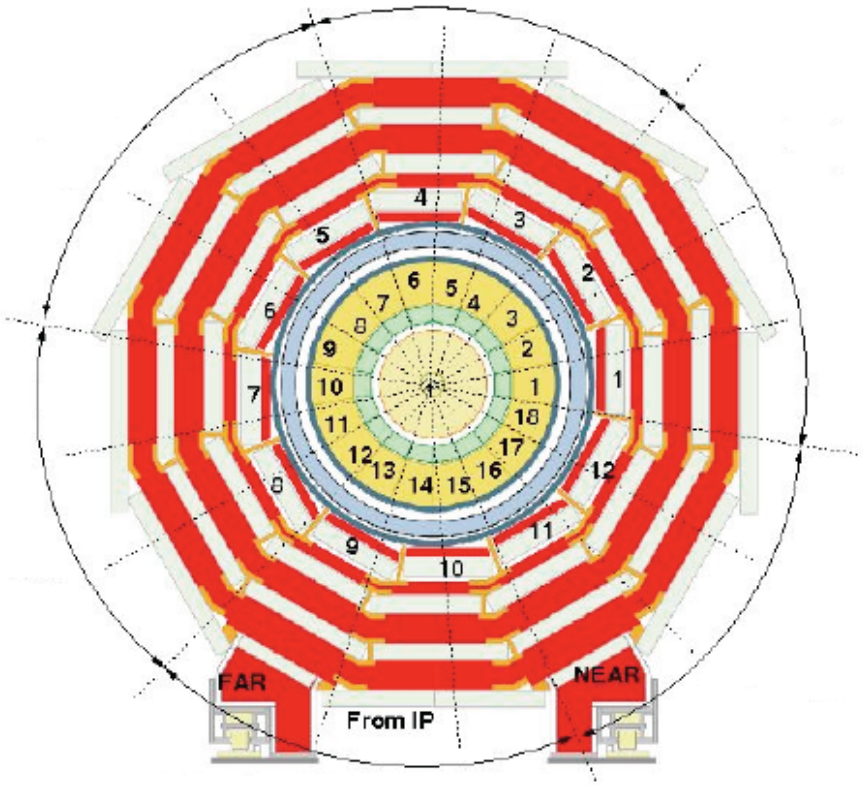

Figure 3.1: CMS (r, ϕ) view, with the muon sectors numbering (red chambers) and the ECAL supermodules numbering (on a yellow background)

3.1 Data collection and amplitude reconstruction

Data directly collected from the detector are the so-called Raw Data. For ECAL this consists, for each read-out channel, in the digital representation of the signal

for the event under examination. An adjustable number of samples, typically 10, constitutes the time frame stored for further online and offline processing. The digitizations are made at the bunch crossing frequency of 40 MHz, using an ADC clock locked to the LHC bunch structure. Therefore, the signal is composed of 10 samples, each one measured in ADC counts (see the "pulse-shape" in Figure 3.2). Digi Data can then be produced within the CMS Software, through the so-called `unpacker`: Digis bring the same information carried by the raw data, but stored in a more "human-readable" format.

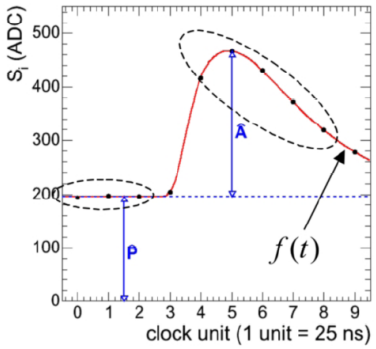

Figure 3.2: Profile of the signal pulse from a crystal, where P is the pedestal, A the amplitude and f(t) is the fit function.

The hit reconstruction is performed, starting from Digi Data, in two steps: Digi to Uncalibrated RecHits, and Uncalibrated RecHits to RecHits. The Uncalibrated RecHits provide the timing and amplitude information, while the RecHits provide timing and energy information, where the energy value is obtained after the calibration process. At this level a mask is generally applied to suppress "noisy" channels (see Section 3.3.2).
The simplest method of reconstructing the amplitude is to take the sampling on the maximum as the measurement of the signal. However, one of the reasons for reading out a larger number of samples is to allow more sophisticated digital processing of the signal to reduce the noise contribution. So, the signal amplitude can be computed in different ways:

- with the "max-min" method, that is subtracting the minimum value to the maximum;

- with the "shape fit" method, where the signal shape is fitted with an analytical function like $Ax^{\alpha}e^{-\frac{x}{\beta}} + c$.

- with the "weights" method, where the amplitude is estimated as a linear combination of discrete time samples as shown in Eq. 3.1

$$A = \sum_{i=1}^{i=N} \omega_i \cdot S_i \tag{3.1}$$

where ω_i are the weights, S_i are the time sample values in ADC counts and N is the number of samples used in the digital filter. The weights are determined to minimize the noise contribution: the determination of the optimal set of weights makes use of a representation f(t) of the time development of the signal pulse (fit function).

The amplitude information, provided by the Uncalibrated Rechits, is used to estimate the measured energy. For this purpose, the calibration is performed by means of the inter-calibration constants (channel-to-channel relative components) and of the global absolute energy scale. In Eq. 3.2 the reconstructed energy of an ECAL deposit, involving a certain number of cells, is shown:

$$E_{e,\gamma} = G \cdot F \cdot \sum_i c_i \cdot A_i \tag{3.2}$$

More details about ECAL calibration can be found in Chapter 4.
The reconstruction process converts Digi Data to Reco Data. From Reco, other higher level physical quantities can be provided at the off-line level and later stored into the event: for instance, the clusterization process is performed. As for electrons and photons, approximately 94% of the incident energy of a single electron or photon is contained in a 3×3 matrix of crystals and 97% in a 5×5 matrix. Finally, the SuperCluster is the endpoint of the ECAL reconstruction for electrons and photons. The presence in CMS of material in front of the calorimeter results in bremsstrahlung and photon conversions and, because of the strong magnetic field, the energy reaching the calorimeter is spread in ϕ. The spread energy is clustered by building a cluster of clusters, called "supercluster", which is extended in ϕ. The SuperClusters can be:

- Hybrid Superclusters, built with a fixed bar of 3 or 5 crystals in η and with a dynamical shape over ϕ; the algorithm makes superclusters which are decomposed into basic clusters;

- Island Superclusters, built from non-overlapping Island clusters. An Island basic cluster is built starting from a seed crystal, that is a local energy maximum above a defined threshold; from the seed position, adjacent crystals are examined, scanning first in ϕ and then in η. Along each scan line,

crystals are added to the cluster until a rise in energy or crystal without recorded energy is encountered. A crystal is added to the cluster if it contains a rechit with positive energy, it has not been assigned to another cluster already and the previous crystal added (in the same direction) has higher energy. In much the same way, the Island Superclusters can be produced, by searching for the most energetic cluster and then collecting all the other nearby clusters in a very narrow η-window, and much wider ϕ-window.

Energy corrections for shower containment and η-dependent energy loss in material are applied at the SuperCluster level to the greatest extent possible. See Fig. 3.3 for an illustration of the sequence for ECAL reconstruction.

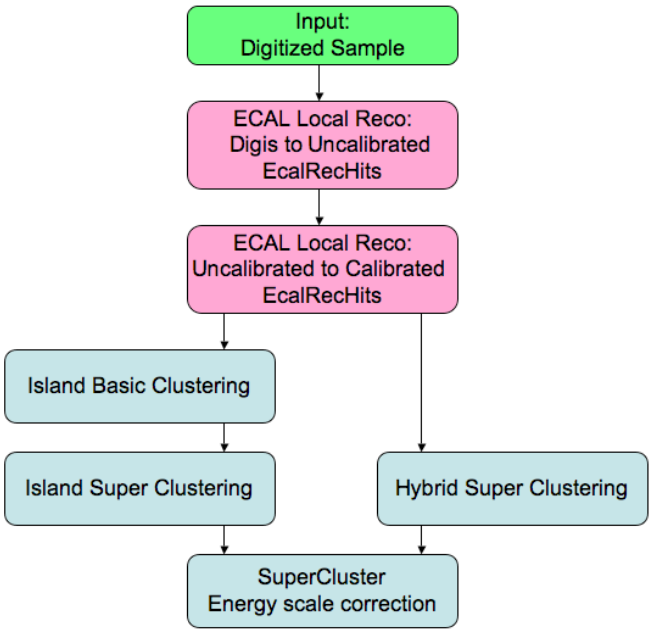

Figure 3.3: Sequence of the ECAL objects reconstruction.

As for cosmic muons, the basic cluster algorithm uses the 5×5 matrix, while the superclusters are produced optimizing the Island algorithm with a particular set of metrics.

3.2 Cosmics events in ECAL

The muon signal in ECAL has been precisely measured during the CRUZET data taking. The detector geometry allows different topological configurations for the

cosmic events (see Fig. 3.4):

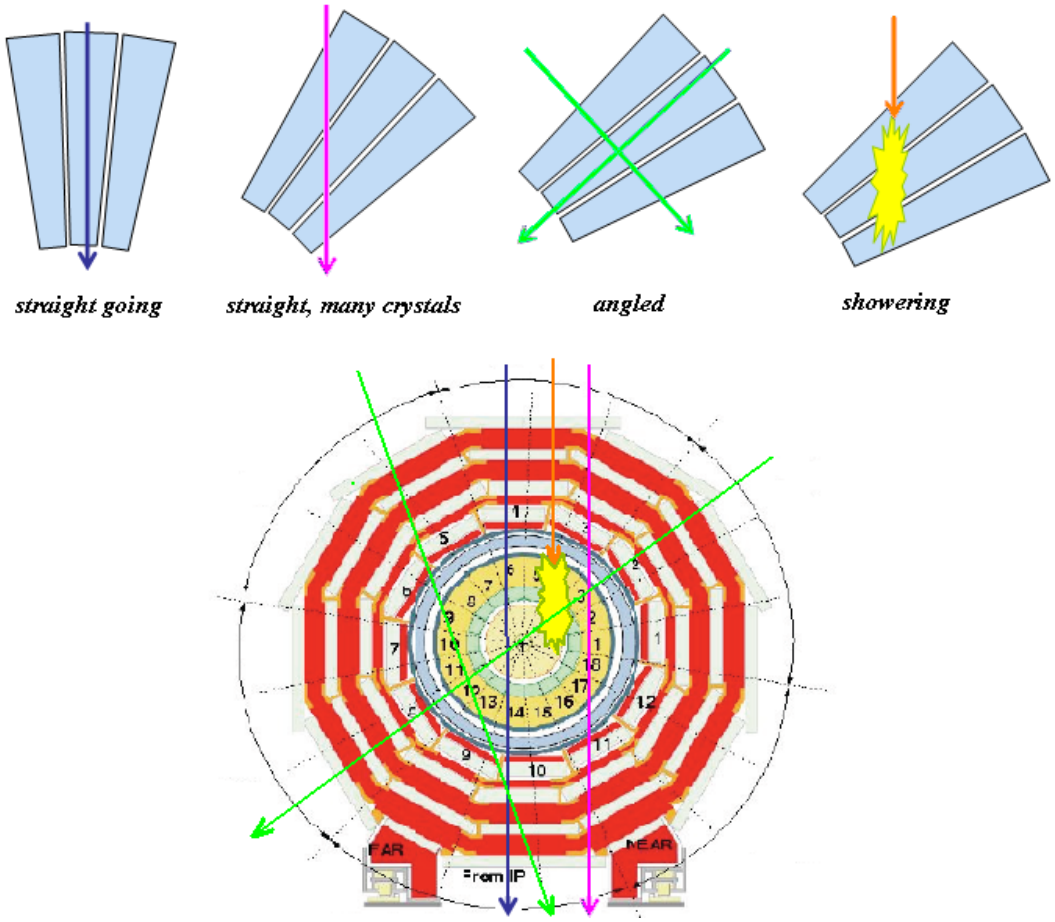

Figure 3.4: Topological configurations of muons crossing ECAL

- "straight going" muon ($\phi \approx 90°$), whose energy deposit is well contained in a single crystal;
- "straight going" muon covering many crystals;
- "angled" muon, can cover many crystals or just a few;
- showering muon, with a much more high energy deposit.

Cosmics events can be visualized using the Iguana Event Display (see Fig. 3.5 and 3.6 which refer to a high energy event), but also some `CMSSW` tools have been prepared in order to analyse them and give a quasi-on-line feedback on the ECAL performance (see Section 3.2.1).

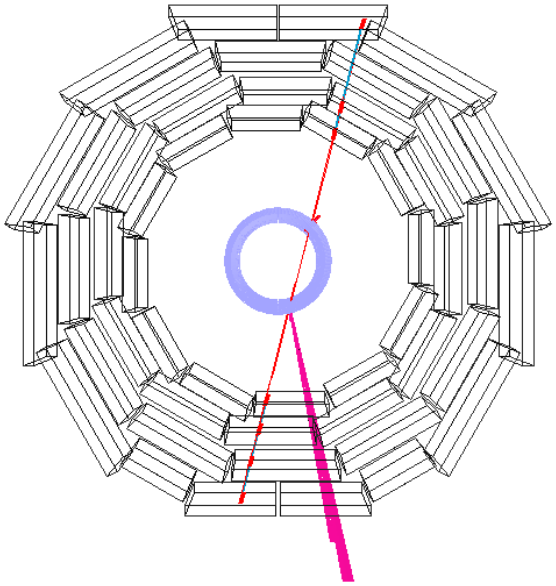

Figure 3.5: Iguana visualization of high energy event 37324 from CRUZET I, (r, ϕ) view; the ECAL cluster is in pink (energy of 288 GeV, 25 crystals in cluster), the muon hits from DT chambers and the reconstructed track are in red.

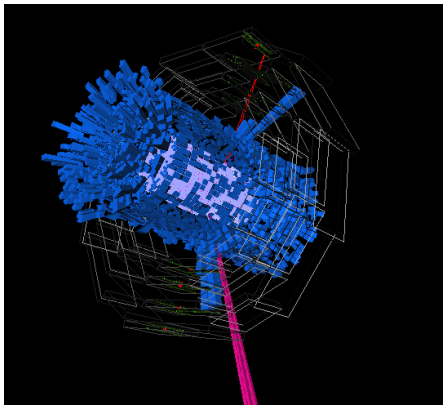

Figure 3.6: Iguana visualization of Event 37324 from CRUZET I, 3D view with HCAL clusters (in blue).

3.2.1 Cosmics Event selection

The cosmics event selection is performed in ECAL using two criteria optimized for purity and efficiency:

· single crystal "stream", one crystal hit with energy greater than 135 MeV (15 ADC counts);

· two crystals "stream", two adjacent crystals, each above 45 MeV (5 ADC counts).

About 14% of triggered events pass this cosmics selection. The chosen crystals then become "seeds" to build 5×5 clusters (Cosmic Basic Clusters); from here the energy and timing are stored. A straight going muon tipically deposits 250 MeV in a basic cluster.

Zero suppression. In order to reduce the size of the collected data volume, a filtering algorithm (zero-suppression) which suppresses the read out of the crystals below a certain energy threshold is used. The zero-suppression algorithm is based on a digital estimate of the crystal energy, which is compared with a suppression threshold. During GRUMM data taking, the zero-suppression was studied in order to determine the rate of channels read out as a function of the threshold set. Fig. 3.7 refers to GRUMM data and shows the fraction of digis with amplitude higher than a certain threshold. With a threshold of 2 ADC, the data reduction is above 97%.

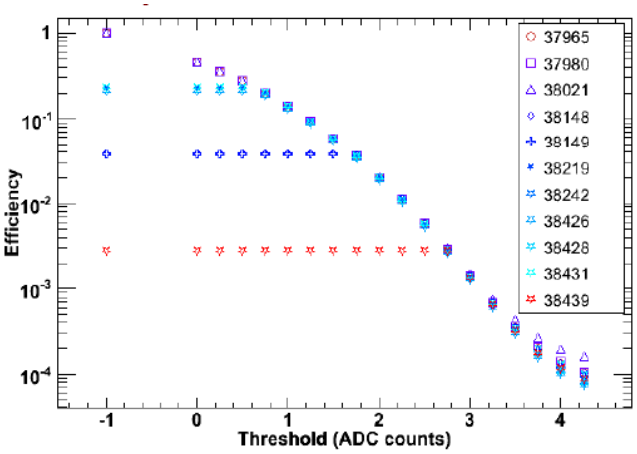

Figure 3.7: GRUMM data: fraction of channels which are read out as function of the 0-suppression threshold; the amplitude is reconstructed with the weights method.

After considering the feedback from GRUMM data analysis, a zero-suppression threshold of 1.75 ADC counts has been applied on the single crystal energy deposit, throughout CRUZET data. In Fig. 3.8 the same plot is shown using CRUZET I data.

Since zero suppression is applied, not all crystals in a 5×5 matrix are included in the basic cluster: in Fig. 3.9 the number of "active" crystals in basic cluster is shown for all CRUZET events which have passed the cosmics selection.

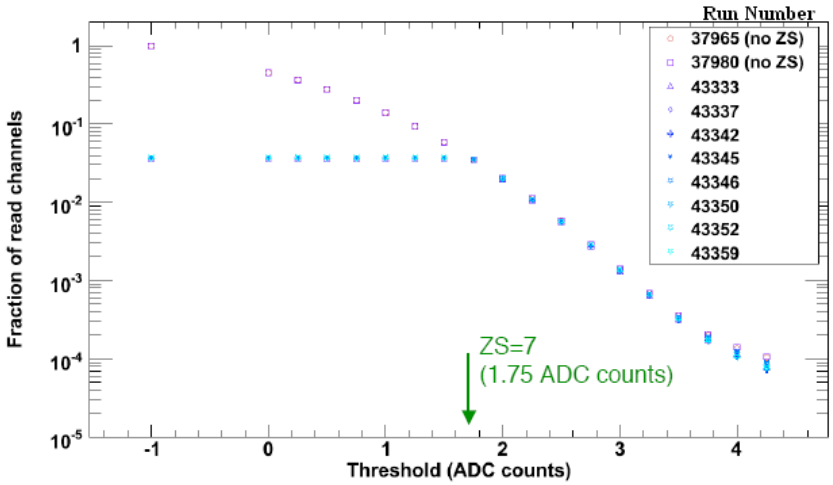

Figure 3.8: CRUZET I data: fraction of channels which are read out as function of the 0-suppression threshold; the amplitude is reconstructed with the weights method.

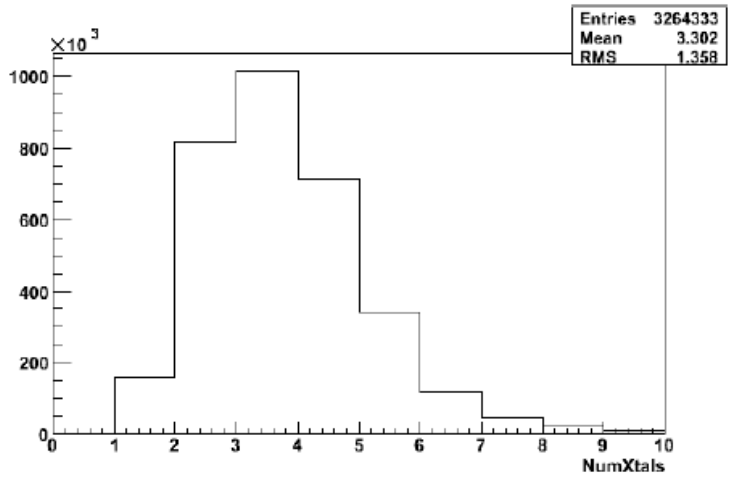

Figure 3.9: CRUZET I data: number of active crystals in each basic cluster for cosmics events

Cosmics cluster energy. In Fig. 3.10 the cluster energy distribution for all CRUZET I cosmics events is shown. On the left side plot, the mip signal at ≈250 MeV is visible, while on the right side plot, a not negligible high energy tail is evident. Since around 1.5 ‰ events have an energy deposit higher than 10 GeV, a specific study is ongoing on high energy events (see Section 3.4).

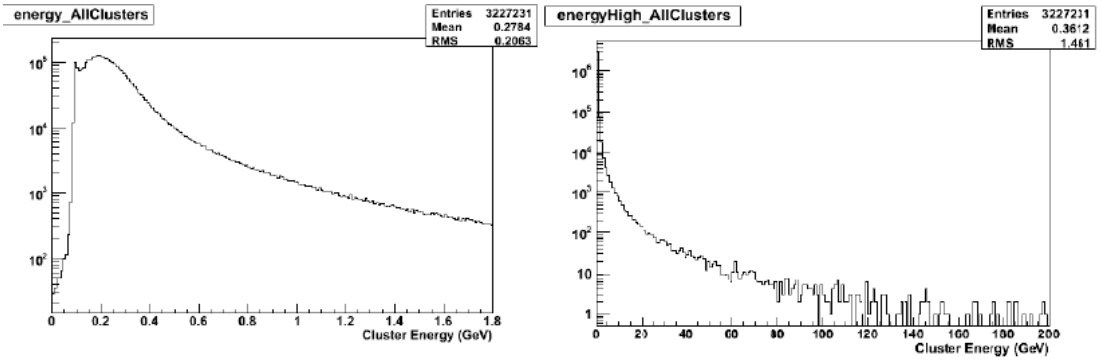

Figure 3.10: CRUZET I data: cluster energy distribution for cosmics events, the mip signal at ≈250 MeV is visible; on the right, the events are shown in a multiple GeV range.

Cosmics occupancy. From 25 Millions CRUZET triggers, 3.2 Millions are selected as cosmics seen by ECAL detector (≈14%). Fig. 3.11 shows the cosmics occupancy, in units of Trigger Towers: the white spots are the evidence of the hardware mask applied at trigger tower level. The (x,y) crystal indices are called *ieta* and *iphi* and label the (ϕ, η) coordinates in the ECAL own reference system. In fact, the ECAL barrel can be seen as a (ϕ, η) grid, where $-85 < i_\eta < +85$ (with no crystal at $i_\eta = 0$) and $1 < i_\phi < 360$ (index 1 starts at -10°). In the same plot note the different occupancy for supermodules EB-11 and EB-12: they had a High Voltage gain setting of 50 (instead of 200) for about one day. This HV issue has been spotted by the offline prompt analysis team and subsequently fixed.

In Fig. 3.12, Fig. 3.13 and Fig. 3.14 the ECAL occupancy is shown for events triggered by ECAL, DT and RPC detector respectively (with an inclusive trigger selection). The regions with higher occupancy are due to the detectors triggering topology.

3.2.2 Muon-ECAL association

It is of great interest to check the association between the hits in the muon system and the ECAL signal. The `CMSSW` tool called "TrackAssociator" has been

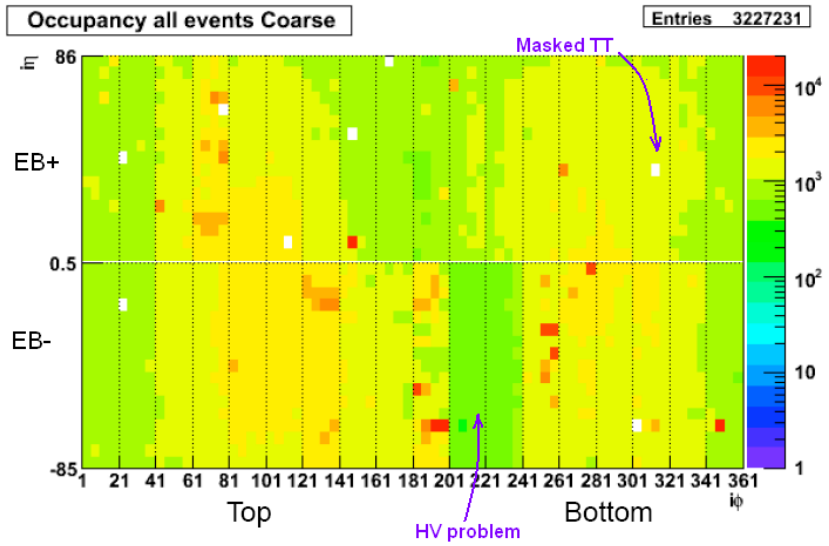

Figure 3.11: CRUZET I data: cosmics occupancy of the ECAL barrel, labeled in Trigger Tower; the bottom region at EB^- has a higher occupancy, corresponding to the cavern shaft position.

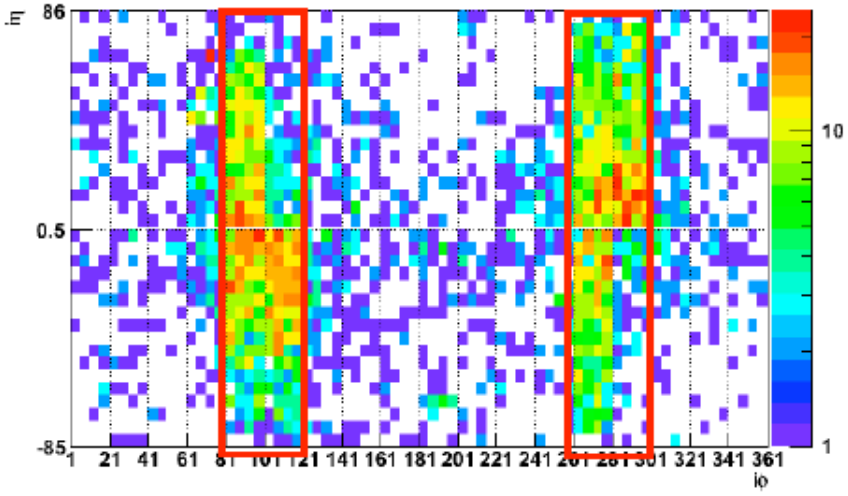

Figure 3.12: CRUZET I data: cosmics occupancy of the ECAL barrel, for events triggered by ECAL itself. The 8 triggering supermodules are bordered in red.

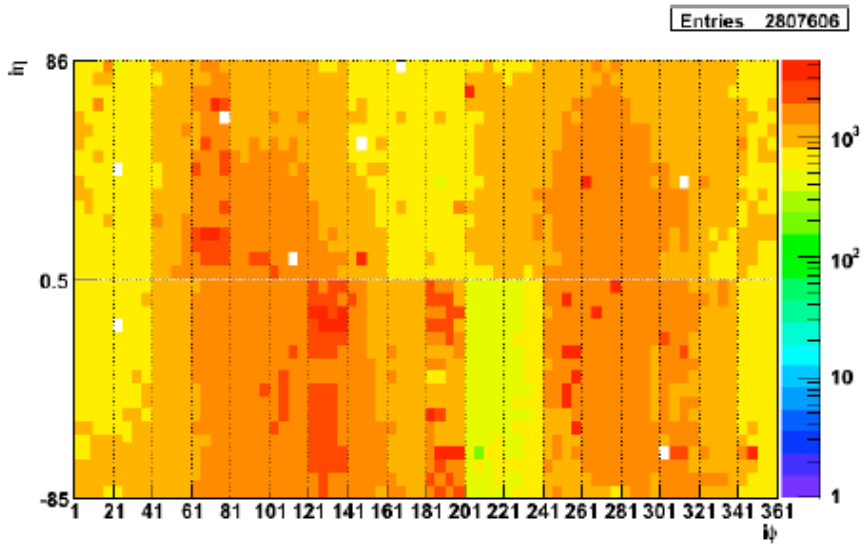

Figure 3.13: CRUZET I data: cosmics occupancy of the ECAL barrel for events triggered by the DT chambers; two main regions can be seen, due to the triggering topology of the DTs during CRUZET I.

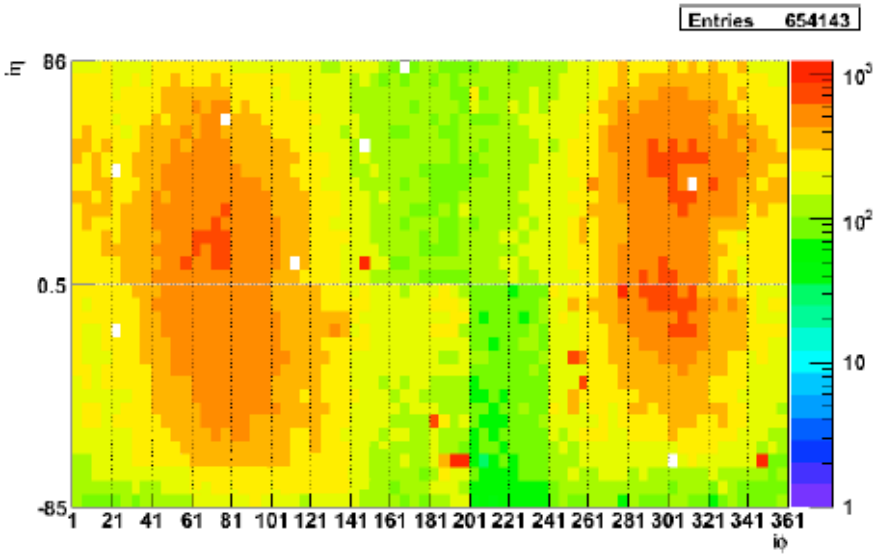

Figure 3.14: CRUZET I data: cosmics occupancy of the ECAL barrel, for events triggered by the RPC chambers. Note that the lower occupancy and the two round-like spots are given by the RPC triggering configuration.

used: it takes the tracks already reconstructed from the muon hits and provide a projection throughout the other detectors, together with a "prediction" of the hit and the energy deposit in each of them. For instance, the position of a hypothetical cluster seed is given.
With the following requirements on each reconstructed track:

- number of muon hits greater than 20, in order to ensure a high quality track (see section 2.2.3);

- transverse impact parameter $|d_0| < 70$ cm and longitudinal impact parafter $|d_z| < 70$ cm

the "quasi" pointing muons, i.e. those passing near the CMS center (interaction point), are selected. In Fig. 3.15 the occupancy of pointing muons is shown. Their energy is peaked at about 250 MeV, as expected (see Fig. 3.16).

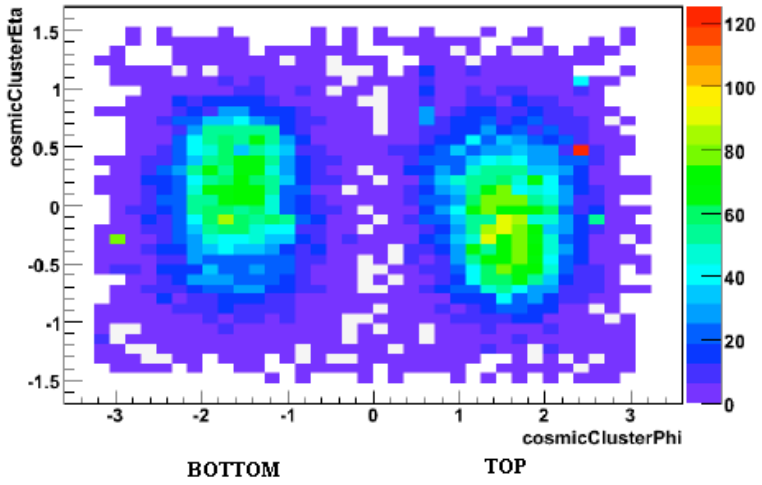

Figure 3.15: Cosmics occupancy of pointing muons in ECAL barrel

Selecting just the pointing muons, the difference between the Track Associator prediction and the "real" ECAL cluster seed position can be used as an index of the match between the muon system signal and the ECAL one. As can be seen in Fig. 3.17, the match (in number of crystals) in CRUZET I data is pretty good within 1 crystal.

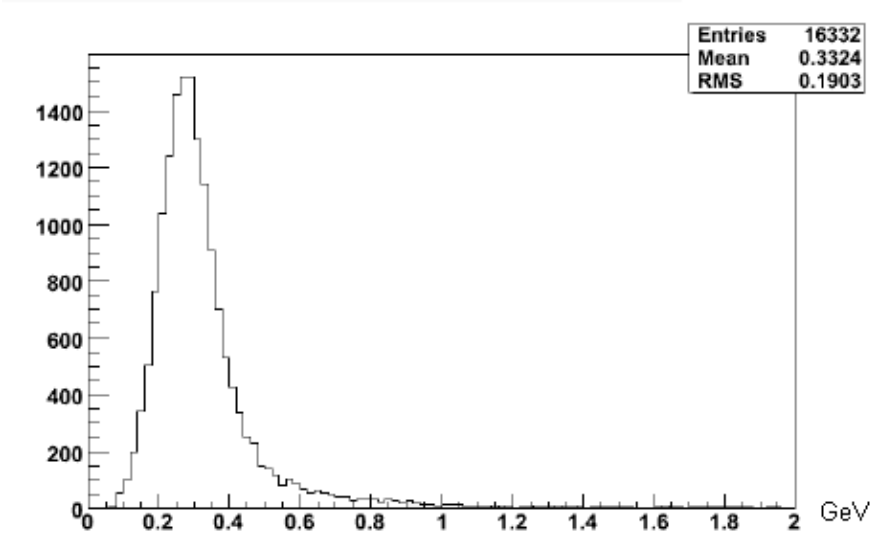

Figure 3.16: Distribution energy for pointing muons

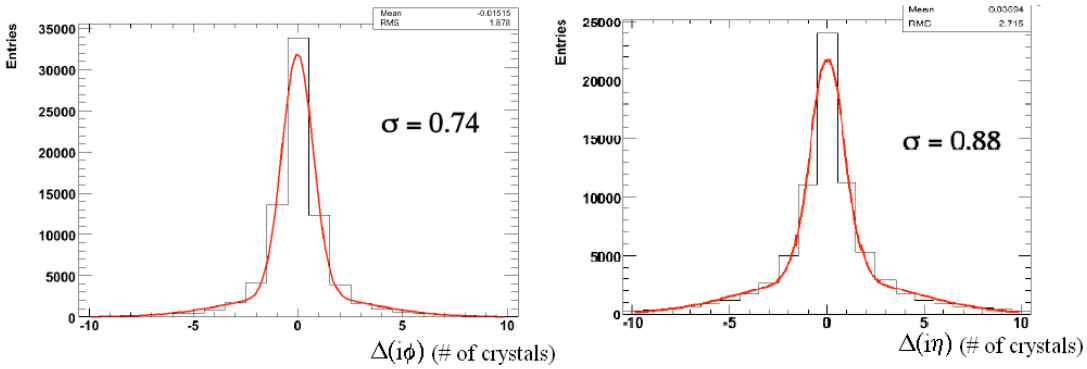

Figure 3.17: Difference (in number of crystals) between the Track Associator prediction and the ECAL cluster seed position; CRUZET I data

3.3 ECAL monitoring

In addition to standard physics trigger data, also special ECAL-only trigger runs, "local calibration" runs, are periodically performed to monitor the ECAL readout synchronization, to check the single channel integrity, to spot possible problems or system instabilities in general and promptly correct for them during the data taking. Moreover, these runs are also useful to monitor the high-level quantities that are needed by the offline reconstruction. These local runs are:

· Laser Runs, where laser pulses (see Fig. 3.18) are sent to every channel and the corresponding 10-sample frames are analysed offline. The response of each channel to the injection of a laser light (normalized to the laser light detected by reference PN diodes) is monitored as a function of time. Laser runs can be used to provide good timing analysis, gain measurements, monitoring of crystal transparency;

· Pedestal Runs, to collect data using a random trigger; they are useful to monitor the mean values and width of the pedestals in the 3 gains;

· Test Pulse Runs, where an internally generated pulse is sent directly to the Front End electronics; they are used to test the electronic chain.

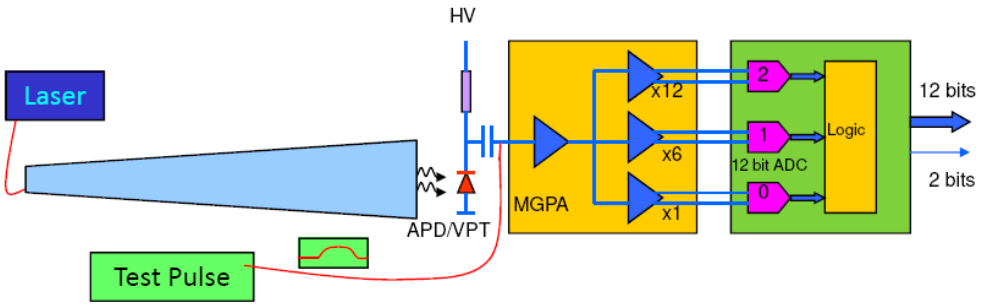

Figure 3.18: VFE architecture for an ECAL single channel

3.3.1 ECAL timing

As long as the laser internal latency is known, laser events can be used to test the single channel data acquisition and to measure any delay due to triggering or differences in the time constant used for the signal shaping. The laser internal latency can be set to the 1 ns level, thus comparable with the time resolution of

the reconstructed signal (1 ns). Moreover, ECAL is timed such that the time-of-flight from the interaction point is taken into account: should the fibres be all of the same length, the expected spread would be of the order of 10 ns.
At the end of CRUZET, laser events have been collected during gap event sequence[2] and the ECAL timing has been studied. The difference in time between the signal 6^{th} sample and the peak obtained from the fit to the signal pulse shape is measured, in clock units (25 ns). In Fig. 3.19 the "timing map" produced with laser data is shown: the colour scale represents this difference. Analysing the ($i\eta$,$i\phi$) map, a small (< 1 ns) variance between the crystals inside trigger towers, a small ($\approx$1 ns) variance between the trigger towers inside each supermodule, and about a 15 ns variance from SM to SM (under investigation) have been measured.

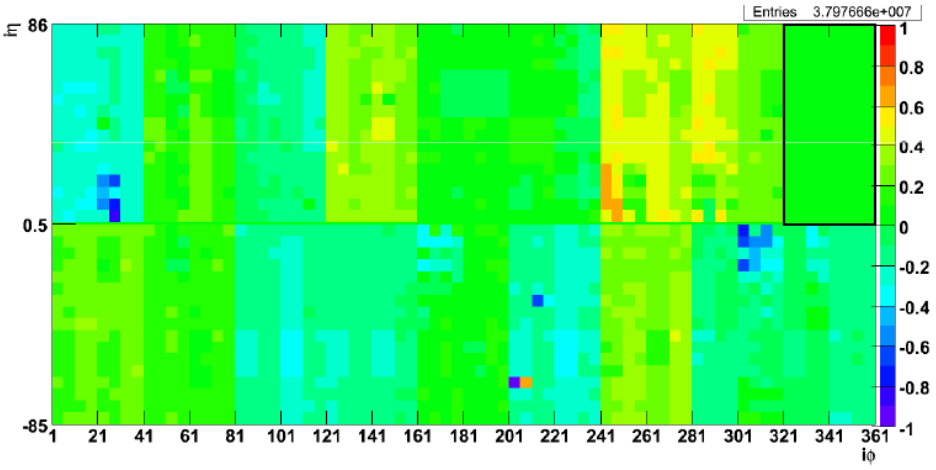

Figure 3.19: Timing map by trigger towers produced with CRUZET laser runs; the color scale represents the difference in time between the signal 6^{th} sample and the peak obtained from the fit to the signal pulse shape, measured in clock units (25 ns). Thus, two colors in the same supermodule correspond to $\approx$1 ns variance, a third color means that a correction is needed. EB+17 and EB+18 were not in the data taking (black box).

Moreover, a timing analysis has been performed using the cosmics runs and asking the ECAL seed to be greater than 100 MeV, in order to reduce the "time-jitter". In fact, since timing is measured from the fit to the pulse shape, a quite high signal is required to obtain a sufficiently good fit. Among the 25 Million CRUZET triggers, 1.5 Million were selected asking the seed to be greater than 100 MeV. In Fig. 3.20 the timing map produced with CRUZET cosmics runs is shown: the signal peak position from the 6th sample is less than 1 bunch crossing

[2]In real data taking, the gap events are events taken during the LHC empty bunches; instead of collisions, test pulse, pedestal and laser events are typically taken. During CRUZET, the gaps have been simulated at trigger level.

different from top to bottom. In Fig. 3.21 the CRUZET ECAL timing for all seeds greater than 100 MeV is shown. The timing is close to the optimal value (zero).

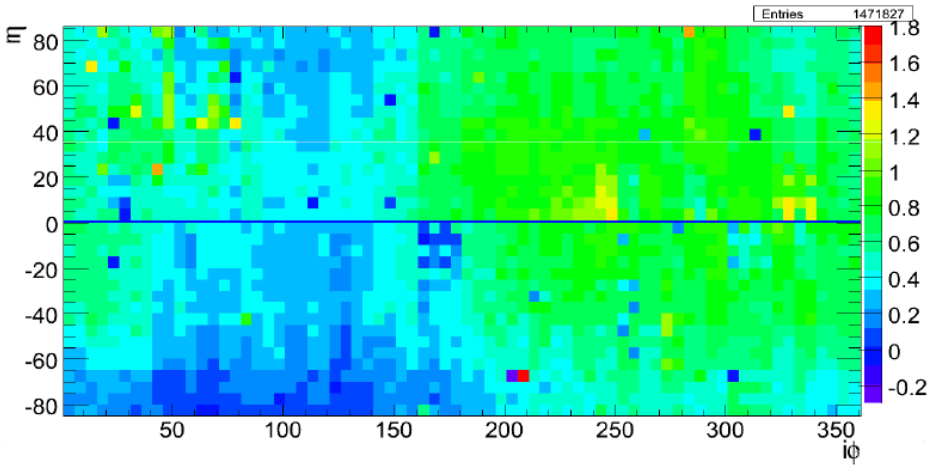

Figure 3.20: Timing map by trigger towers produced with CRUZET cosmics runs; among the 25 Million CRUZET triggers, 1.5 Million were selected asking the seed to be greater than 100 MeV. The color scale represents the difference in time between the signal 6^{th} sample and the peak obtained from the fit to the signal pulse shape, measured in clock units (25 ns): the top is earlier than the bottom, but the difference is less than 1 bunch crossing.

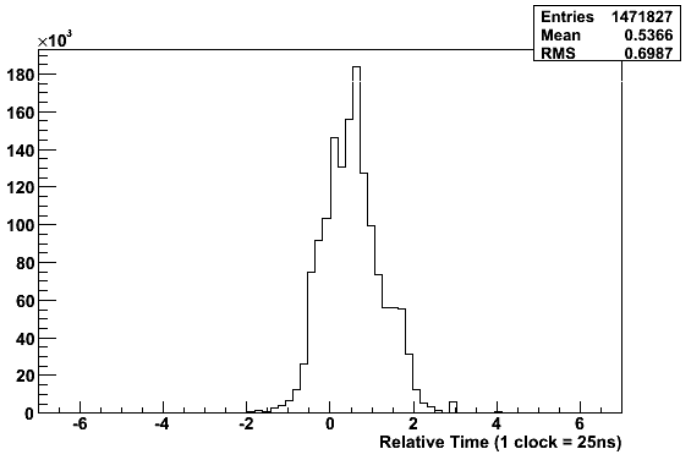

Figure 3.21: CRUZET ECAL timing from CRUZET cosmics runs; all seeds greater than 100 MeV were selected for the analysis.

Comparing laser runs and cosmics runs timing, it has been noticed that internal supermodule timing delays seen in Laser were also seen in cosmics, so they have been later on corrected out, while inter-supermodule timing delays seen in

Laser were not so evident in the Cosmics data. For this reason a deeper investigation is still ongoing.

3.3.2 The problematic channels study

A dedicated and standalone analysis is devoted to identify problematic channels not previously seen. The definition of "problematic" is given according to the study of different variables: the channel average amplitude, the amplitude RMS, channel pedestals and timing. For instance, in Fig. 3.22 the amplitude and amplitude RMS map are shown for one of the CRUZET runs.

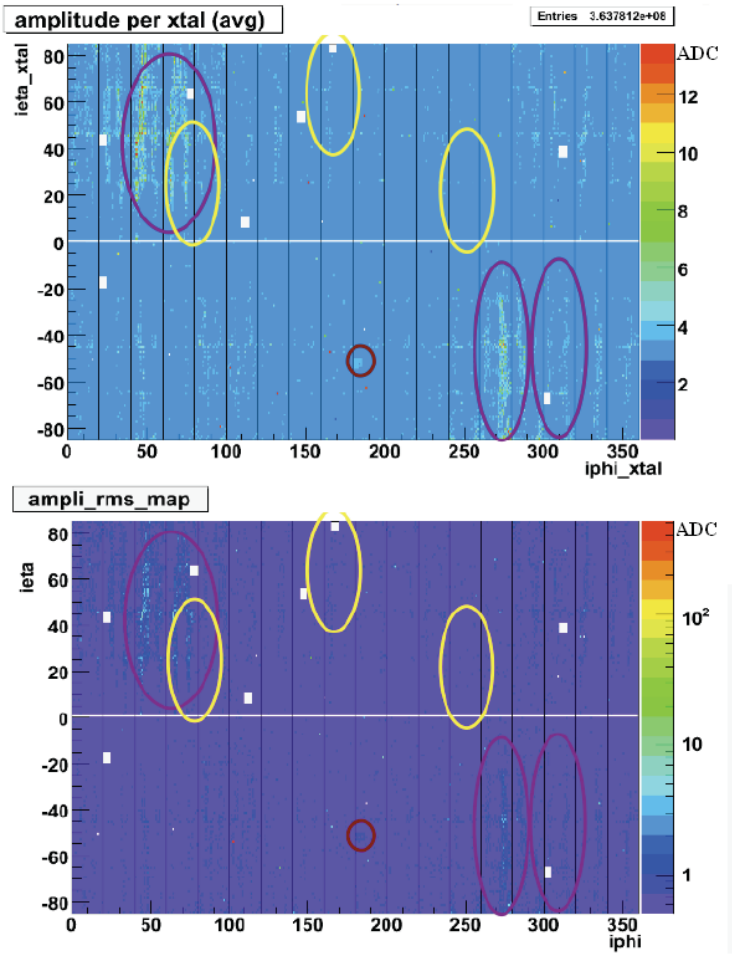

Figure 3.22: On top, the ($i\phi$,$i\eta$) map for the crystal average amplitude in ADC counts is shown, on bottom, the ($i\phi$,$i\eta$) map for the crystal amplitude RMS is shown. Both are produced using an ECAL self-triggered (top-bottom coincidence) CRUZET run. The amplitude was reconstructed with the max-min algorithm.

Different kinds of noise are identified in CRUZET I data:

- High Voltage noise, whose source has been found and fixed before CRUZET II data taking (yellow circles in Fig. 3.22) ;
- Trigger Tower noise, due to trigger towers possibly misconfigured (red circle);
- a "pattern" noise whose source is still unknown and under investigation (violet circles).

This latter kind of noise was already present in early (December and February) data taking, as the amplitude map in Fig. 3.23 shows. Some speculations have been put forward, concerning a possible connection between pattern noise and ECAL cables layout.

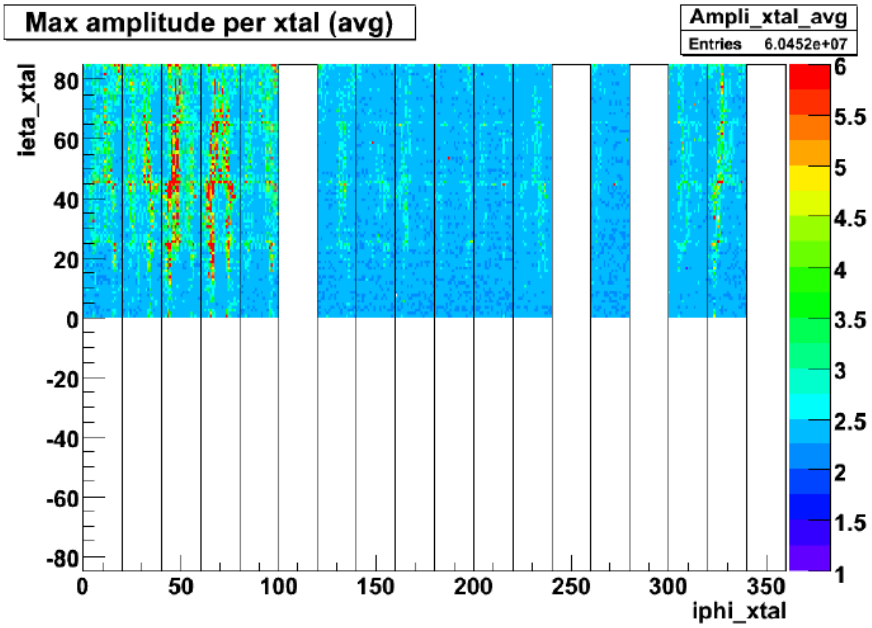

Figure 3.23: $(i\phi,i\eta)$ map for the crystal average amplitude in ADC counts for a February cosmics run; the amplitude is reconstructed with the max-min algorithm.

Thanks to this study, a list of problematic channels has been produced and added to the list of known hardware problems, which can be masked at offline level. See in Fig.3.24 the reconstructed amplitudes for all channels with and without the mask.

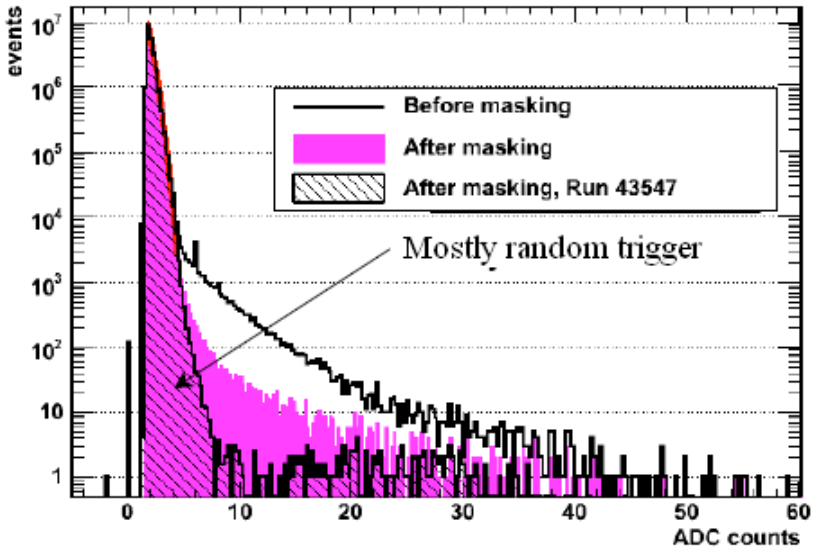

Figure 3.24: Reconstructed amplitudes for all ECAL channels before (black histogram) and after (pink histogram) the hot channels masking. A comparison with the amplitude distribution produced just using a HCAL triggering run (considered a random trigger for ECAL) is also shown.

3.4 High Energy events

Already during the GRUMM data analysis, a few events with a very high energy deposit in ECAL clusters were collected. In Fig. 3.25 the signal pulse shape of a matrix of channels from a GRUMM High Energy event is shown.

During CRUZET, a specific analysis has been developed to study those events. First, a selection of the cosmics events where at least one ECAL basic cluster energy is greater than 10 GeV is performed. Over the ≈24 millions of cosmics events collected, about 5400 are selected, that is 0.02% of the whole statistics. Moreover, about a hundred are events with cluster energy greater than 100 GeV. The first worry has been to establish whether such high energy deposits are due to a kind of noise or to real physics. The sources of real physics, all involving cosmics rays, are supposed to be two: a muon catastrophic Bremsstrahlung[3] or a muon deep inelastic scattering.
Thus, in order to exclude the noise source, a first study on the clusters positions is performed: in Fig. 3.26 a comparison between the number of total clusters and

[3]Bremsstrahlung is a process in which the muon interacts with a nucleus to produce gamma rays; like in pair production, the gamma rays quickly re-interact and produce an electromagnetic shower. Bremsstrahlung is stochastic and results in single catastrophic events of energy loss along the muon's trajectory.

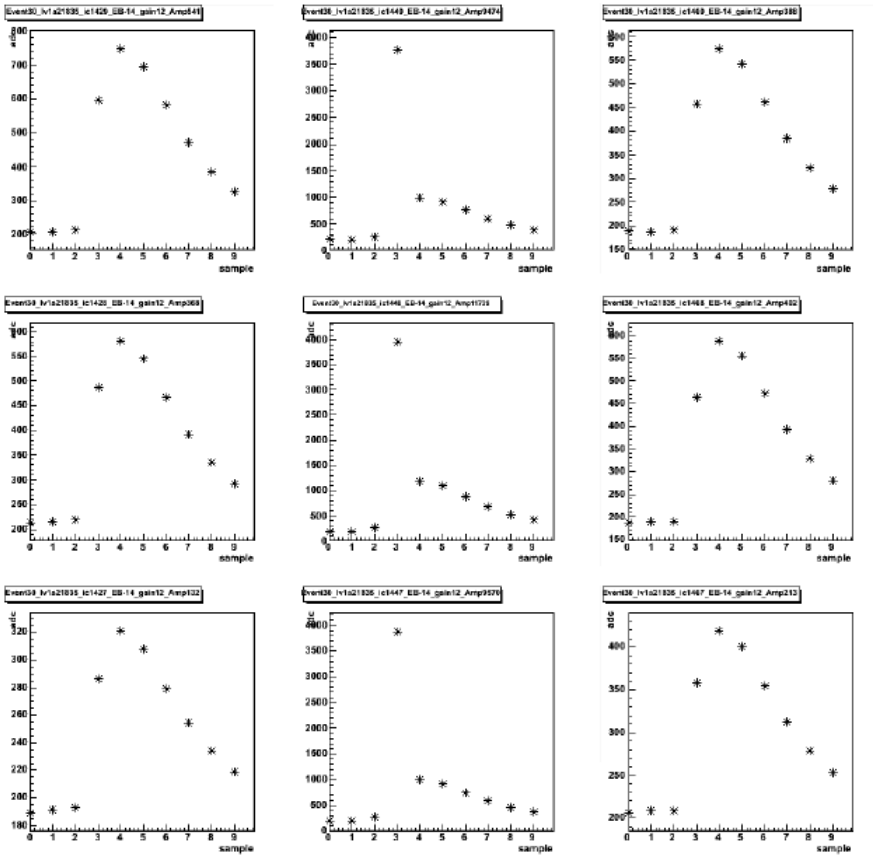

Figure 3.25: Signal pulse shape for a matrix of ECAL channels in a high energy GRUMM event; the amplitude is measured at gain (MPGA) 1 and gain (APD) 200, thus it is of 1000 $ADC_{counts} \cdot 10 \cdot 10 = 100$ GeV. In the same event, there were 83 channels with more than 30 MeV each and more than 450 GeV in total.

the number of high energy clusters for the selected events is shown.

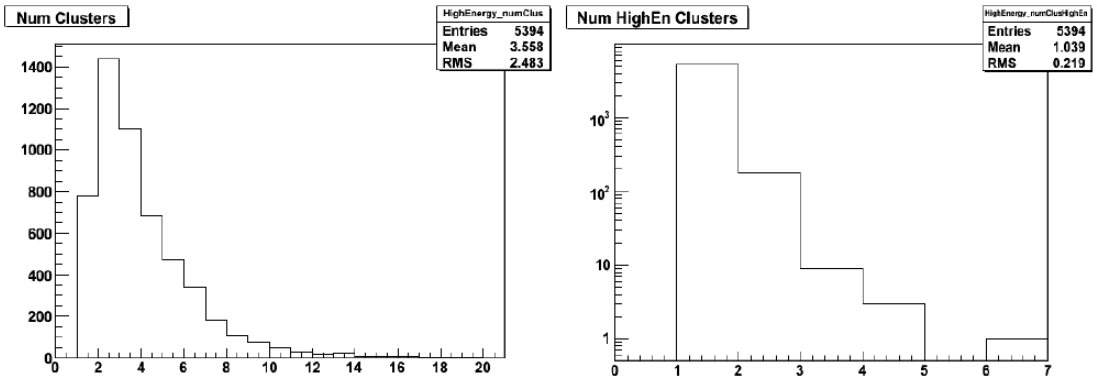

Figure 3.26: On the left, number of total clusters for each high energy event; on the right, number of clusters greater than 10 GeV for the same samples.

As can be seen in the occupancy plots (Fig. 3.27 and 3.28), the high energy clusters are quite homogeneously distributed; the same plots reveal that some of the clusters classified as high energy ones are actually due to noisy channels not yet masked. In fact, the samples used for this analysis are Reco data where the only mask applied is the one at hardware level, while the mask based on the "hot" channels identified during the CRUZET itself is applied only at a later stage.

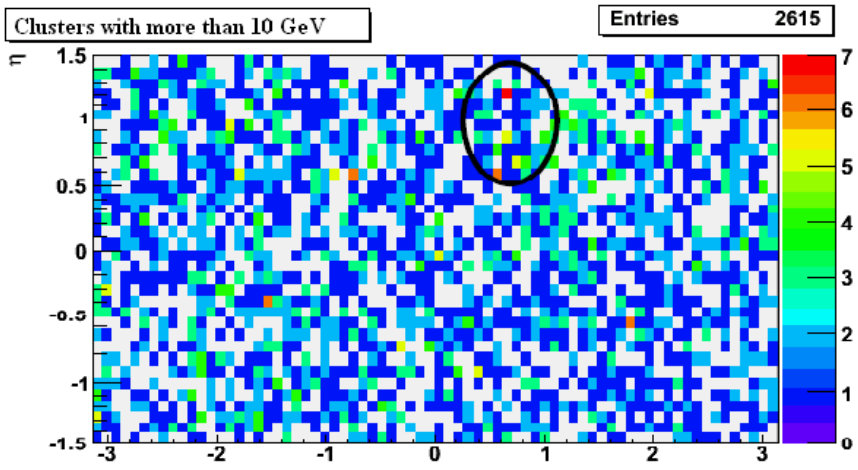

Figure 3.27: Occupancy plot in "real" ϕ and η coordinates, of the clusters with 10 GeV $< E_{clus} <$ 100 GeV; in the black circle, the red spots identified as noisy channels and from then on masked.

Moreover, the reconstructed muon signal has been studied in the same events. The number of tracks reconstructed by the muon system in the high energy events

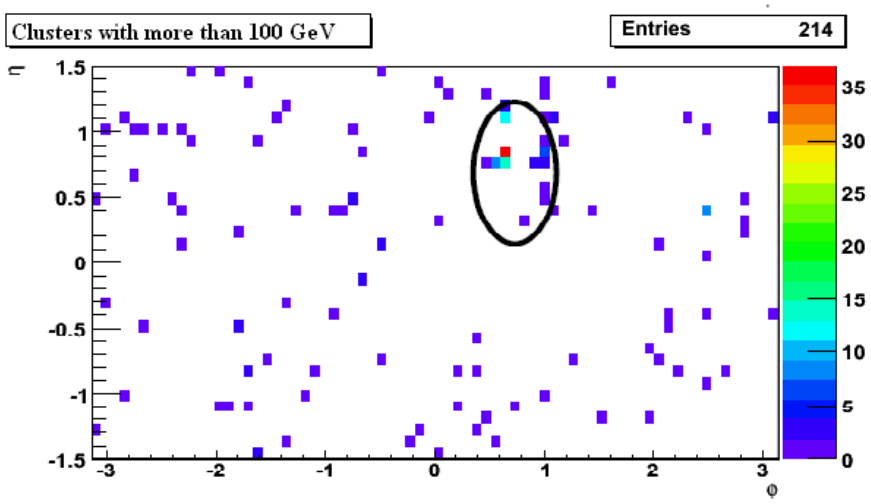

Figure 3.28: Occupancy plot in "real" ϕ and η coordinates, of clusters greater than 100 GeV; in the black circle, the red spots identified as noisy channels and from then on masked.

is shown in Fig. 3.29. About 200 events show zero tracks in the muon system: some of those events could be due to noise. A specific inquiry has been performed for events containing high energy clusters but no muon tracks: the $(i\phi, i\eta)$ energy map for the rechits relatives to those clusters (see Fig. 3.30) shows again the presence of some "hot" channels, but also the evidence of real muons probably not reconstructed by the barrel muon systems, because of their too large track azimuthal angle. In the same figure, the colour scale is the energy scale, so the red spots correspond to very high energy crystal hits. Comparing this map to the conventional occupancy plot binned in crystals, those red spots can be confidently identified as "hot" channels.

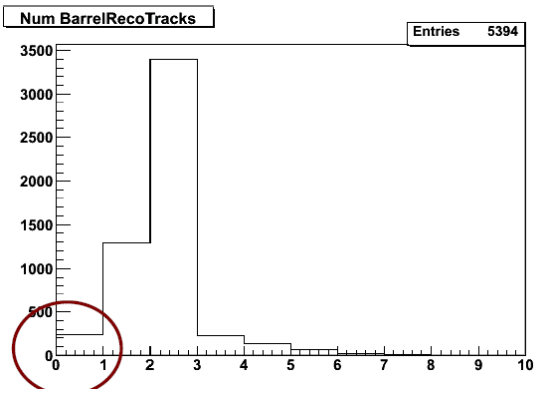

Figure 3.29: Number of barrel tracks reconstructed by the muon system (high energy events sample)

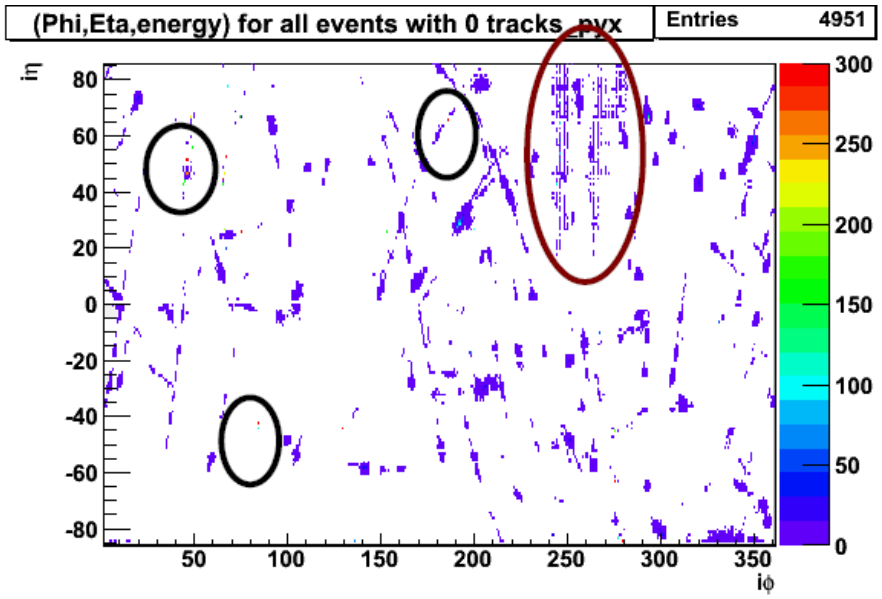

Figure 3.30: Occupancy of ECAL rechits for high energy events with no reconstructed tracks; in the black circles, identified hot channels; in the brown circle, a suspected hardware feature

After the exclusion of the noisy channels from the analysis, the cluster seed occupancy plot obtained from the remaining events shows that those events are homogeneously distributed with no more "hot" spots (see Fig. 3.31).

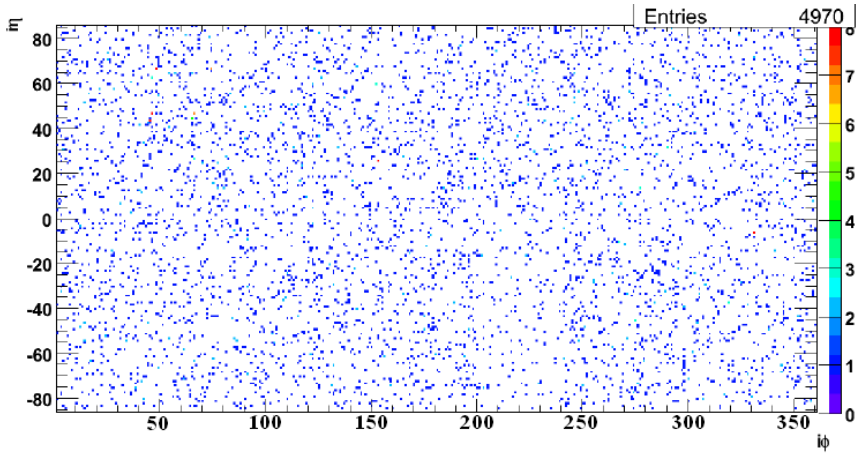

Figure 3.31: ECAL occupancy for high energy cluster seeds; filtered events.

Some preliminary studies have been done to identify the possible high energy events source. The number of active crystals for each cluster is peaked at about 15 crystals, where "active" means a crystal hit greater than 27 MeV from the high

energy cluster[4] (see 3.32). This number is also constant along the ϕ coordinate: in fact, for showering Bremsstrahlung photons the showers can basically cover the same number of crystals, indipendently from the ϕ position of the cluster. Since the number of crystals in high energy clusters is greater than the one in standard cosmics events, the μ catastrophic Bremsstrahlung hypothesis is more probable. First studies on the HCAL energy deposition have been performed to exclude or validate the deep inelastic scattering hypothesis; evidence of a high energy hadronic tail has been shown in filtered events, but the ECAL plus HCAL association, event per event, is still under study.

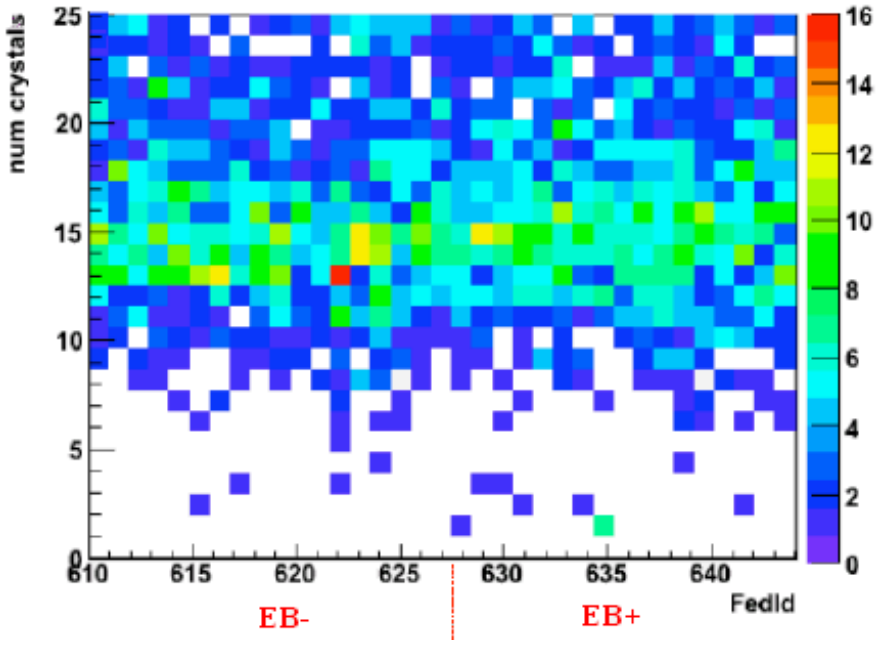

Figure 3.32: Occupancy for the number of active crystals in each cluster versus the supermodule identification number (FedId); the upper cutoff at 25 crystals is due to the fact that the basic cluster is built as an array of 5x5 crystals.

Finally, a specific study to verify the association between high energy clusters and reconstructed tracks is being performed. The idea is to build SuperClusters starting from basic clusters and to compare the high energy super clusters position with the energy deposit position predicted by the TrackAssociator. Events with certain configurations (such as containing two super clusters opposite in ϕ, with at least one high energy deposit) can be selected to perform the TrackAssociator comparison on higher purity samples. Super clusters with no associated tracks will need a deeper investigation.

[4]energy threshold put on ECAL rechits; since the ECAL channels noise RMS is of about 1.1 ADC counts, the threshold is chosen at $\approx 3\ \sigma$ from the noise

Chapter 4

The ECAL Phi-symmetry intercalibration with jet events

This chapter describes my contribution to the ECAL calibration task, focused on the phi-symmetry intercalibration of crystals at fixed η using jet trigger events. The ECAL calibration strategies are presented: both the *start-up* methods, using laboratory measurements, test beam or cosmics data, and the *in-situ* ones, taking advantage of physics events, are summarized. The phi-symmetry intercalibration algorithm is shown in detail, together with the results obtained on several millions of simulated events.

4.1 ECAL calibration strategy

The physics reach of the CMS electromagnetic calorimeter, in particular the discovery potential for a low mass SM Higgs in two photons decay channel, depends on its excellent energy resolution. The energy resolution can be parameterized as a function of energy

$$\left(\frac{\sigma}{E}\right)^2 = \left(\frac{S}{\sqrt{E}}\right)^2 + \left(\frac{N}{E}\right)^2 + C^2$$

where

- S is the stochastic term, affected by the shower lateral containment in a matrix of crystals and by the photo-statistics;
- N is the noise term;
- C the constant term; affected for instance by leakage effects, light yield non-uniformity effects, temperature stabilization and intercalibration precision.

The values of these parameters are measured from test beams and are listed in Fig. 4.1.

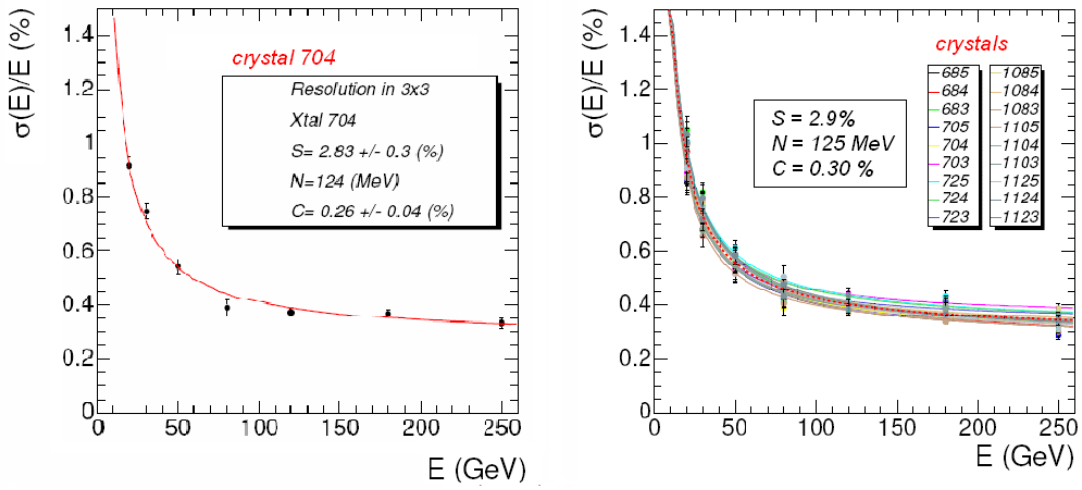

Figure 4.1: ECAL energy resolution as a function of electron energy as measured from 2006 beam test; the energy is reconstructed by summing the deposits in an array of 3x3 crystals, where the central crystal is the maximum energy one.

The final goal of the calibration strategy is to achieve the most accurate energy measurement for electrons and photons: in fact, crystal intercalibration precision goes directly into the energy resolution constant term with very little scaling, due to the fact that most of the energy of an electromagnetic cluster is contained within a single crystal (around 80%). For this reason, the calibration represents a key aspect to reach the design performance of the electromagnetic calorimeter. Calibration is naturally seen as composed of a global component, giving the absolute energy scale, and the so called "intercalibration component", that is the channel-to-channel relative component. Schematically we decompose the reconstructed energy into three factors:

$$E_{e,\gamma} = G \cdot F \cdot \sum_i c_i \cdot A_i$$

where

G is the global absolute scale to convert ADC counts in MeV; it can be set using physics events like $Z \rightarrow ee$ or electron beams of known energy. In particular, at the highest gain (12) the ADC full scaled 4096 counts correspond to a charge Q≈5 pC. With an average of 4.5 photoelectrons/MeV produced by each impinging electron, at APD gain 50, the global absolute scale can be

estimated as

$$\frac{Q}{4096\ ch_{ADC} \cdot q_{(e^-)} \cdot 4.5\ e^-/MeV \cdot 50} \approx 40\ MeV/ch_{ADC}$$

F is a correction function depending on the type of particle (for instance, it distinguishes between photons and electrons), on its position and momentum, and on the clustering algorithm used; it corrects for energy loss due to bremsstrahlung and various containment variations. Since different reconstruction algorithms are used to estimate the energy of different electromagnetic objects, the very first "algorithmic" corrections are obtained from simulated data. For some of the corrections (e.g. containment corrections), test beam data are also used to verify the simulation; in other cases (e.g. issues related to conversions and bremsstrahlung radiation in the tracker material) it will be necessary to use data taken *in situ* with the running detector. Two channels are particularly useful for this purpose: $Z \rightarrow \mu\mu\gamma$ [1] and $Z \rightarrow ee$;

c_i factors are the intercalibration coefficients, describing the channel to channel relative difference. The main source of channel-to-channel response variation in the barrel is the crystal-to-crystal variation of scintillation light yield (RMS of $\approx 8\%$), while in the endcap it is due to the VPT signal yield variation, together with the product of the gain, quantum efficiency and photocathode area variation (RMS of $\approx 25\%$). The channels intercalibration must be achieved using physics events (see the next paragraphs);

A_i are the signal amplitudes in ADC counts, summed over the clustered crystals.

4.1.1 Intercalibration at start-up

Preliminary estimates of the intercalibration coefficients c_i were obtained from laboratory measurements of crystal light yield, test beam precalibration of some supermodules and the commissioning of all supermodules with cosmics rays.
The laboratory measurements were performed in the two regional centres where ECAL was assembled (at CERN and at INFN-ENEA, Rome): the crystals were excited with a ^{60}Co source and the crystal light yield could be measured using a photo-multiplier tube. It was thus possible to estimate the c_i as

$$\frac{1}{c_i} \propto LY \cdot \epsilon_Q \cdot c_{ele} \cdot M$$

[1] the photon coming from inner bremsstrahlung

LY = Light Yield of the crystals

M = photo-detectors gain

ϵ_Q = photo-detector quantum efficiency

c_{ele} = calibration of the electronic chain

An independent LY measurement can also be obtained exploiting the correlation between the crystal LY and the Longitudinal Transmission at 360 nm.
The precision of the intercalibration which can be reached using the average of the direct light yield measurement and the light yield predicted from the longitudinal transmission is 4.2%; using only the direct light yield this precision is 4.6%. It is also possible to intercalibrate supermodules using an electron beam with well known energy: in the test beam, along the beam line, a supermodule was mounted on a rotating table allowing a full scan of each crystal in the supermodule with steps in both the η and ϕ coordinates. The response of a single crystal to electrons depends on the electron impact position. The electron position was measured with a set of hodoscopes; then the dependence in the 2 lateral coordinates was fitted with a 4^{th} order polynomial separately (see Fig. 4.2) and the measured amplitude S_{mean} was corrected as

$$S_{corr} = S_{meas} \frac{P_x^{max} P_y^{max}}{P_x(x) P_y(y)}$$

where $P_{x,y}^{max}$ is the maximum of the polynomial and x,y are the measured position of the incident electron in the two lateral coordinates.

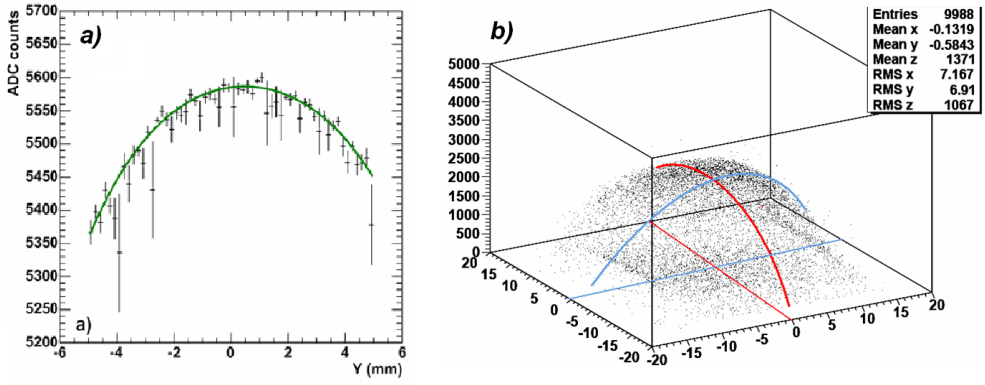

Figure 4.2: Polynomial fit (a) to energy in a single crystal as a function of a lateral coordinate, and energy distribution (b) in a 3x3 crystals matrix as a function of the 2 lateral coordinates.

The c_i are then defined as the ratio of the mean value of the corrected response with respect to a reference crystal. With this method 9 supermodules were intercalibrated and an overall precision of 0.3% was obtained.

Fig. 4.3 shows the intercalibration coefficients calculated from laboratory measurements plotted versus the test beam measurements.

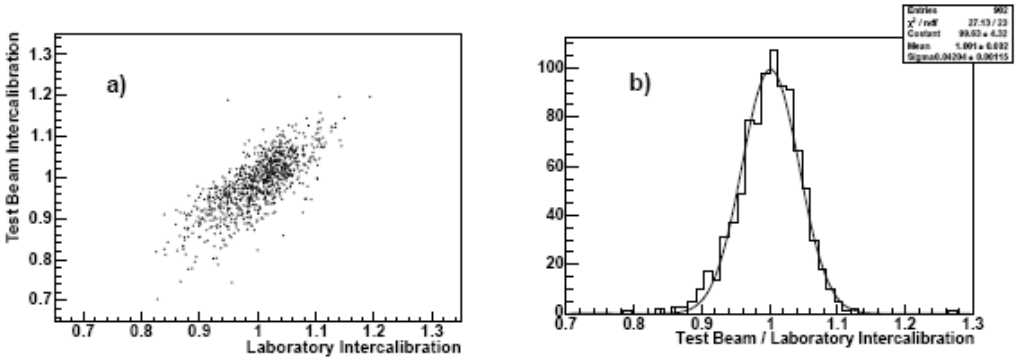

Figure 4.3: (a) Intercalibration coefficients obtained with supermodule 10 at the 2004 test-beam with high energy electrons versus intercalibration coefficients calculated from laboratory measurements, and (b) distribution of the fractional difference between the laboratory estimated coefficients and coefficients measured in the test-beam.

After the electronic integration, all 36 supermodules were calibrated using ≈5 million cosmics events collected in about one week: intercalibration coefficients were obtained for barrel supermodules with cosmic muons well aligned with the crystal axes. Aligned cosmic rays could be selected by vetoing on signals above a rather low threshold in the adjacent crystal with highest signal, avoiding the need for external tracking. In order to have a rather uniform number of cosmics events along the super-module length, the super-module was inclined by ≈10°. An average precision of 1.5% was obtained for all channels, ranging from 1.4 % in the central region to 2.2% at the high η end of the barrel.

4.1.2 In-situ intercalibration

In-situ calibration techniques will be the fundamental tool to reach the 0.5% goal precision. The "golden" channel to obtain an absolute calibration of ECAL crystals is the Z mass constraint in $Z \rightarrow e^+e^-$ but, since the statistics will be insufficient at low luminosity, several methods have been proposed to obtain intercalibration coefficients:

· at the start-up, the ϕ-independence of the energy deposited in the calorimeter can be used to rapidly inter-calibrate regions at the same pseudo-rapidity (η) (see Section 4.2);
· a complementary method, not relying on the momentum measurement, is based on $\pi^0 \to \gamma\gamma$ and $\eta^0 \to \gamma\gamma$ mass reconstruction;
· the Z mass constraint in $Z \to e^+e^-$ can also be used as a complement of the η ring inter-calibration at the start-up, or as invaluable tool to tune the electron reconstruction algorithms and to fix the energy scale. A similar use can be made of $Z \to \mu\mu\gamma$, where the photon comes from inner bremsstrahlung, constraining the γ energy using the di-muon system;
· once the tracker will be fully functional and aligned, the abundant electrons, mainly from $W \to e\nu$,[2] can be used for local intercalibration in regions with uniform tracker material, exploiting the E=p peak to be compared to the reconstructed energy.

Intercalibration with single electrons. Once the tracker is fully operational and well aligned, intercalibration of crystals can be obtained using the momentum measurement of isolated electrons. The main difficulty in using electrons for intercalibration is that they radiate in the tracker material in front of the ECAL, and both the energy and the momentum measurement are affected. Moreover the average amount of bremsstrahlung varies with tracker material thickness. So the single crystal intercalibration is obtained minimizing the difference between the energy and momentum measurements, in order to unfold the contribution of individual crystals to each energy measurement[3]. Due to the variation of the average value of E/p peak with η, caused by the variation of the amount of material in front of the ECAL, intercalibration is obtained locally in region over which the average value of the E/p is rather constant; in a second step the regions are intercalibrated between each other.
The calibration precision achievable is strongly dependent on the available statistics: preliminary results shows that with $\approx 2.4\ fb^{-1}$, the intercalibration precision obtainable is about 0.6%.

Intercalibration using π^0 and $\eta^0 \to \gamma\gamma$ events. These low mass particles could provide a useful calibration tool for a rapid intercalibration of all crystals, but also to study the effects of crystal transparency corrections by the laser

[2] because these electrons have a similar p_T to the photons of the benchmark channel $H \to \gamma\gamma$
[3] two algorithms to achieve this minimization have been considered and the results are similar and show no dependence on the technique used

monitor and to rapid check-out the detector performance. The intercalibration obtained from π^0 is not sensitive to tracker material as much as the intercalibration obtained using electrons is: decays into photons that do not convert are unaffected, while converted low-energy photons give rise to low-energy electrons, which reach the ECAL far from the expected photon impact point (because of the magnetic field). For this reason, the π^0 are selected as a pair of closeby ECAL clusters. It was found that almost all of the events containing a usable π^0 are well tagged by the isolated electron Level-1 trigger and some selection are applied to separate the π^0 candidates from the combinatorial background (e.g. it is important to consider only π^0 candidates with small opening angles). The main difficulty of the method to properly identify π^0 is to isolate the corresponding photons.
The preliminary results suggest that it will be possible to intercalibrate the ECAL using the reconstructed mass of π^0 with a precision of 0.5% with a very high statistic (1000 events per crystal). See figure 4.4.

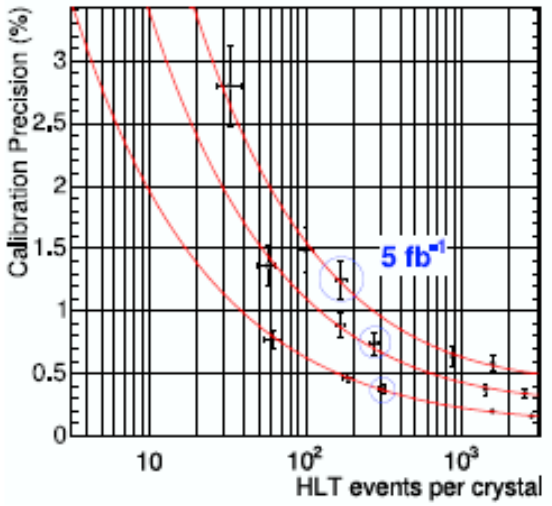

Figure 4.4: Calibration precision versus the number of events per crystal for different η regions. Upper curve: the last 10 crystals in the ECAL Barrel, Middle curve: 10 crystals in the middle of ECAL Barrel, Lower curve : the first 15 crystals in the ECAL Barrel. The third point along each line gives the precision for 5 fb^{-1} of integrated luminosity

Intercalibration using Z decays. Another powerful tool for ECAL calibration is the Z mass constraint in $Z \rightarrow ee$ decays, also useful for other purposes

like the tuning of the algorithmic corrections. At the start-up scenario these corrections will be taken from Monte Carlo simulation and the $Z \rightarrow ee$ events can be used to obtain a preliminary estimate of the intercalibration factors between rings ("intra-rings"). For this calibration only events with 2 golden electrons are chosen[4], since their reconstructed energy shows the least dependence on the tracker material. Taking the calorimeter regions as rings of crystals at fixed η in the ECAL barrel, the intercalibration coefficients are measured using the peak of the mass distribution. The peak is obtained from an iterative Gaussian fit in a region around the peak which excludes the crystals on the module borders. The achieved ring intercalibration precision corresponds to 0.6% using events for an integrated luminosity of 2.0 fb^{-1}.
Radiative decays $Z \rightarrow \mu\mu\gamma$ can be used in a similar way as the $Z \rightarrow e^+e^-$: the photon energy is here constrained from the di-muon system and the Z mass. The advantage of these events is the significant rate of high-p_T photons with very little background and an energy which can be known independently of ECAL. Events are selected by placing a loose cut on the di-muon mass and searching for a photon with high p_T within a fixed distance from the di-muon axes. Such events can be used to intercalibrate different regions of the ECAL (a statistical precision better than 0.1% is achieved for an intergated luminosity of 1 fb^{-1}), but also to investigate other calibration tasks (cluster correction algorithms, overall energy scale, etc).

4.2 ϕ-symmetry intercalibration with jet events

A method to intercalibrate crystals within rings at the same η takes advantage of the ϕ-symmetry of deposited energy: *the total energy deposited from a large number of events should be the same for all crystals in a ring in the same pseudorapidity (η) interval*. Then, intercalibration can be performed by comparing the total energy deposited in each crystal with the mean of the distribution of total energies for all crystals at that pseudorapidity ring.
At the start-up scenario, the phi-symmetry method will be a useful tool to speed-up the calibration procedure, thanks to the high rate of QCD events used and the resulting availability of energy deposits in ECAL crystals. Preliminary works show that a few hours of data taking at low luminosity assure an intercalibration precision in the barrel region ranging over η from 1.6% up to 3%. In fact,

[4]electrons least affected by radiation emission, with a reconstructed track well matching the supercluster and with a well behaved supercluster pattern, e.g. with a very low bremsstrahlung fraction

at the complete CMS optimal functioning, an intercalibration of ECAL to the design goal (better than 0.5%) should be achieved rapidly (in about 2 months) using electrons from notable decays, but this optimal functioning will surely take some time: a precision of about 0.6% is expected with a mean number of 370 events collected per ring, at an integrated luminosity[5] of $\approx 2\ fb^{-1}$. For this reason, phi-symmetry calibration will be an important tool at start-up, because it does not rely on the tracker measurements and can be performed without a perfectly aligned tracker. It will reduce the number of intercalibration coefficients remaining (ring-to-ring intercalibration), which can then be determined in a few days using $Z \rightarrow 2e$ events. On the other hand, the expected average precision is worse than the precision expected from calibration with single electrons, and an "intra-ring" intercalibration is also needed: so the phi-symmetry will be a starting method to be used in addition with other algorithms, like the calibration by Z decays.

Choices of events. Two kinds of events are suitable to investigate the ϕ-symmetry intercalibration method: minimum bias events and Level-1 jet triggers. Minimum bias events are the most general trigger option, chosen to avoid the problem of trigger bias (see Section 4.2.3). The main disadvantage is the very low energies involved, with some drawbacks:

1. since a lower threshold cut on energy deposits must be placed to exclude noise, in minimum bias events it must be chosen at the lowest possible value, in order to discriminate noise but not to loose a considerable amount of energy for the analysis. While the Gaussian-noise is simply correctable and its width variation is weak, there could be some form of non-Gaussian noise giving rise to large errors in the calibration precision; in Fig. 4.5 the noise is shown for cosmics events in ECAL;

2. since this calibration is performed at low energies (a few hundred MeV, see Fig. 4.6), a dangerous extrapolation to much higher energies (150 GeV) is needed, in order to perform physics studies with electrons and photons at LHC.

For these reasons, the proposal to use the trigger system to select higher energy deposits was put forward. The use of electromagnetic triggers would bring other problems of trigger bias (e.g. trigger towers with crystals miscalibrated toward high values would be over-represented and would put a bias in the total energy sums per rings); so the use of jet triggers is considered a more promising choice.

[5]This corresponds to 1 year of data taking at $\mathscr{L}_{inst} \approx 6.6 \cdot 10^{31} cm^{-2} s^{-1}$

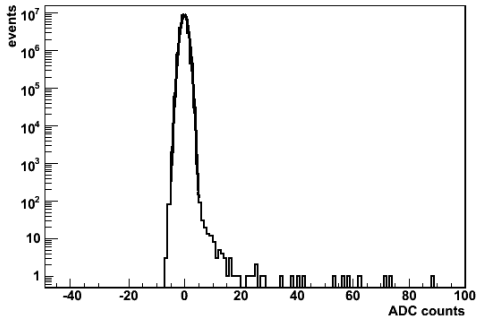

Figure 4.5: Noise amplitude in ADC counts for GRUMM cosmics events; 1 ADC count = 9 MeV at gain $G_{APD} = 200$.

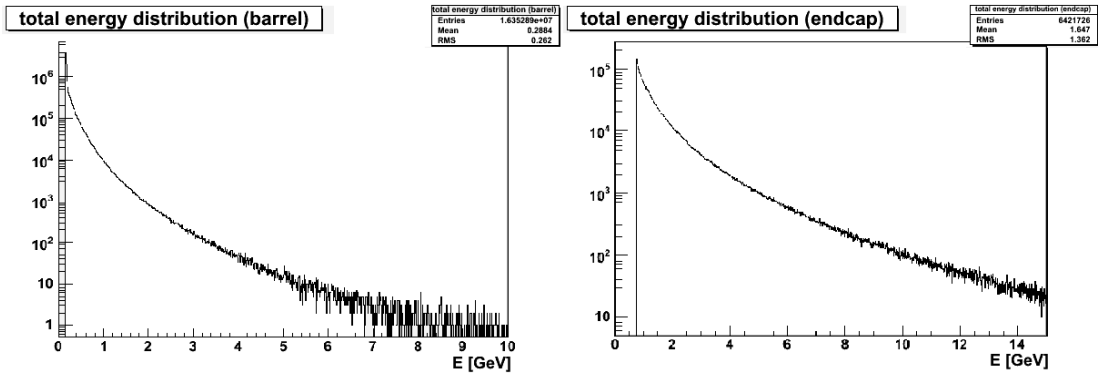

Figure 4.6: Rechits energy distribution obtained with 1 million minimum bias events (barrel rechits on the left, endcap rechits on the right).

The present work focuses on the phi-symmetry intercalibration algorithm with simulated jet trigger events.

Aims of my work. The main aim of my work was to define a strategy for rapidly obtaining the ECAL barrel crystals intercalibration coefficients using jet trigger events and to prepare and test a dedicated algorithm into the `CMSSW` framework. I measured the limit on the precision of this method and checked the effectiveness of the chosen trigger.

4.2.1 Event generation and L1 trigger simulation

Several millions of QCD events in different bins of hard scattering transverse momentum were generated with `PYTHIA` (see Appendix B), under the assumption of the best complete knowledge of the distribution of material in front of the calorimeter. In Tab.4.1 the details about some available QCD generated samples are listed; for the following analysis, the sample with $\hat{p}_T^{hard} > 120$ GeV is used, at a luminosity scenario of $\mathscr{L}_{integr} = 10^{30} cm^{-2} s^{-1}$.
Here are the main generation criteria:

- full simulation in `CMSSW_2_0_7` (see Section 2.5);
- nominal detector geometry simulation with `GEANT4`;
- scattering parameters set for *very* start-up scenarios
  $\mathscr{L}_{integr} = 10^{30} cm^{-2} s^{-1}$ (up to the goal of $\mathscr{L}_{instant} = 1 pb^{-1}$), 43×43 bunches
  $\mathscr{L}_{integr} = 10^{31} cm^{-2} s^{-1}$ (up to the goal of $\mathscr{L}_{instant} = 10 pb^{-1}$), 156×156 bunches
- no pile-up simulation;
- zero suppression;
- digitization and reconstruction in `CMSSW_2_0_7`.

Please note that the pile-up is not simulated, because the present work focuses on a start-up scenario where no pile-up is expected yet.

The Level-1 Trigger is then emulated to produce the jet trigger collections, that are the `CMSSW` collections of objects which fired the L1 jet triggers and were stored into the Event. L1 jet trigger objects are provided by the Regional and Global Calorimeter Trigger. As described in section 2.4.4, L1 jet trigger uses the transverse energy sums (electromagnetic and hadronic) computed in the so-called "calorimeter regions" (4×4 trigger towers); then, a 3×3 calorimeter region sliding

number of QCD generated events	minimum $\hat{p_T}$ for hard scattering	cross section	rate at $\mathscr{L} = 10^{30} cm^{-2} s^{-1}$
$\approx$ 3.9 M	30 GeV	160 μb	160 Hz
$\approx$ 4.1 M	50 GeV	21 μb	21 Hz
$\approx$ 4 M	80 GeV	3 μb	3 Hz
$\approx$ 2.8 M	120 GeV	0.5 μb	0.5 Hz

Table 4.1: Details about some available QCD generated samples (the rates are evaluated without taking into account efficiencies and acceptance); one week of data taking at the luminosity of $\mathscr{L} = 10^{30} cm^{-2} s^{-1}$ corresponds to an integrated luminosity of $1 pb^{-1}$. In the coloured row the sample used for the following analysis is shown.

window technique is used to span the complete coverage of the CMS calorimeter. The L1 jet candidate is found by requiring that central region E_T is higher than the 8 neighbour region E_T values and higher than a fixed value. In Fig. 4.7, the whole process is shown, up to jet reconstruction.

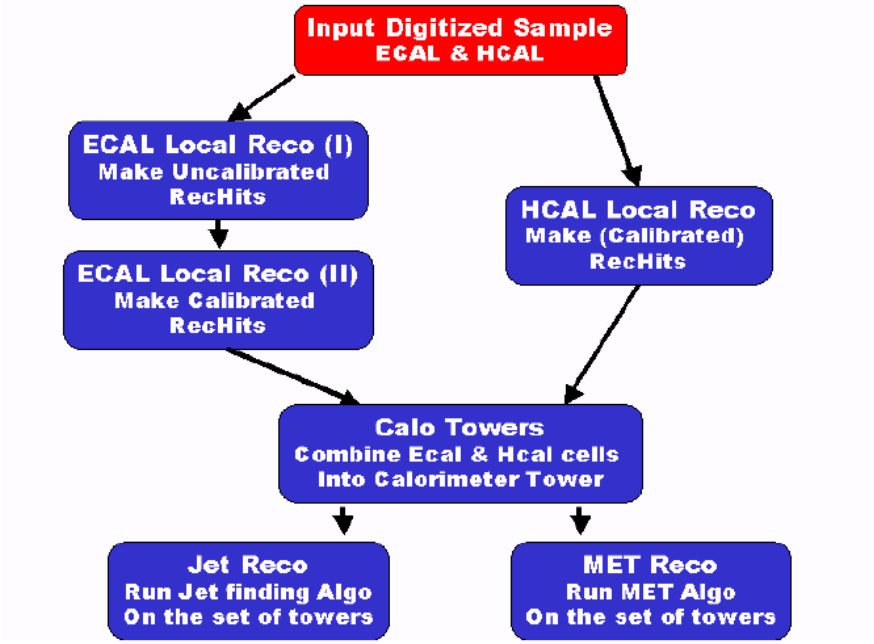

Figure 4.7: Schematical description of the jets reconstruction.

The two luminosity scenarios differ for the prescale factors applied at the various trigger streams: in Tab. 4.2 some of the available trigger streams for jets are shown, together with the corresponding prescale factors.

algorithm	prescale factor ($1pb^{-1}$)	prescale factor ($10pb^{-1}$)
ZeroBias	300000	1000000
MinBias	300000	1000000
SingleJet15	10	1000
SingleTauJet10	10	10000
SingleJet30	1	100
SingleJet50	1	1
SingleTauJet30	1	100
SingleTauJet40	1	10
DoubleTauJet30	1	10
DoubleJet70	1	1
TripleJet50	1	1
QuadJet15	10	100

Table 4.2: Subset of trigger streams from the L1 trigger menu used.

Together with the L1-trigger emulation, the `l1extraParticles` are also produced: these collections are physical representations of the L1 trigger objects, providing the useful quantities for the next analysis steps (e.g. transverse energy and momentum, η and ϕ coordinates). L1 jets are organized, at the hardware level, into 3 different collections[6]:
· Tau jets;
· Forward jets, with $|\eta| > 3.5$;
· Central jets, with $|\eta| < 3.5$, thus including both barrel and endcap jets.

4.2.2 Event selection

A first simple study on the generated event has been performed, in order to gain a good knowledge of the available jets and of their basic features.

Since the Forward jets spread over a region at $|\eta| > 3$, they do not cover the ECAL geometrical acceptance and for this reason they are not used for the following analysis. To focus just on Tau and Central jets, in Fig. 4.8 the two jet collections (E_T, η) distribution is shown.

After the exclusion of Forward L1-jets, all events containing at least 2 jets (Tau or Central) are selected. With this single request, it has been found that ≈96% of the generated events can be kept. Moreover, all jets from selected events appear to have fired the less "severe" L1 jet trigger path (`SingleJet15`).
The transverse energy distribution of the L1-jets, ordered by E_T, is plotted in Fig. 4.9. As expected, the minimum hard scattering $\hat{p}_T$ at the generator level

[6]those are in fact software objects used for user convenience, but in the end every condition is expressed using hardware objects

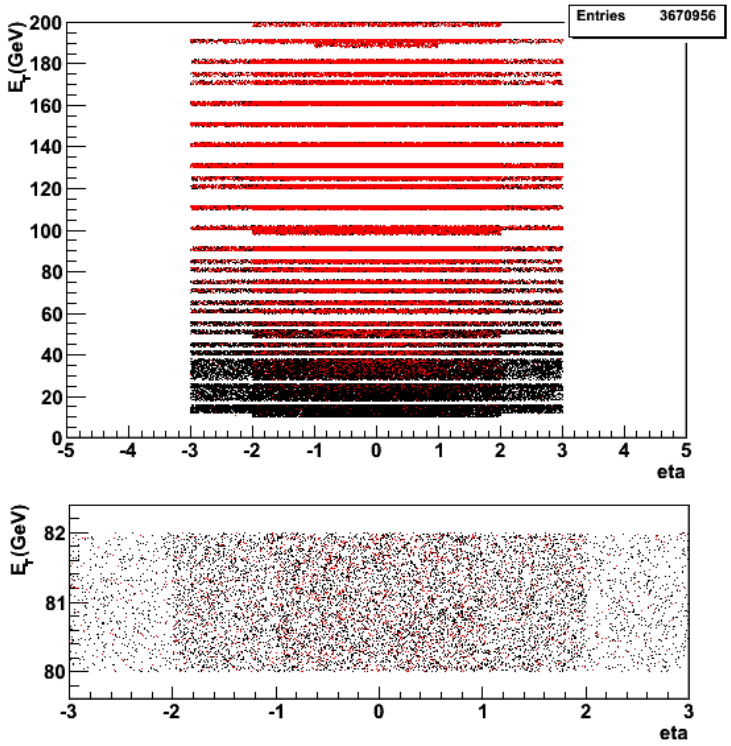

Figure 4.8: On top, (E_T, η) distribution for Central Jets (black marker) and Tau Jets (red marker); on bottom, a zoom of the top plot is presented. The clear quantization in E_T is due to the hardware trigger (L1) energy measurements.

affects the distribution of the highest E_T jet (leading jet).

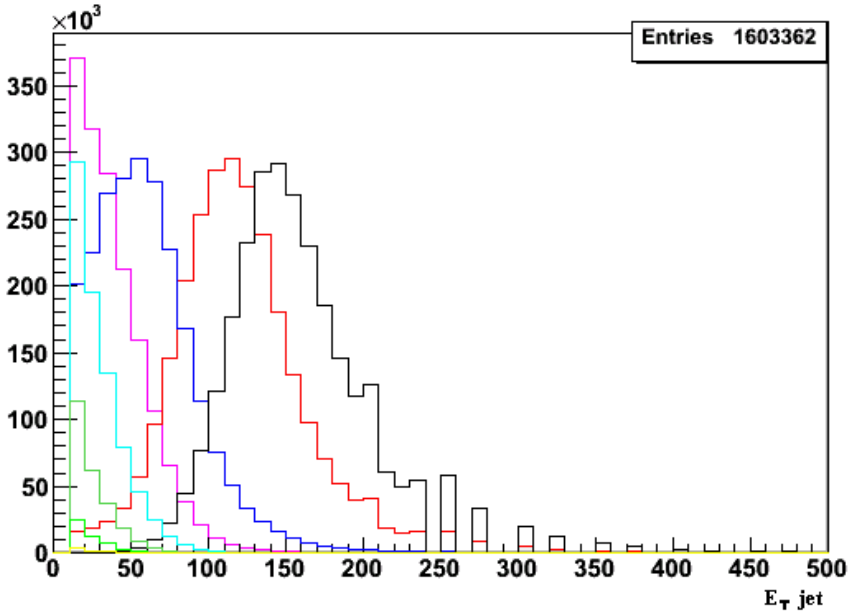

Figure 4.9: Transverse energy distribution for the L1 jets, ordered by E_T; sample with $p_T^{hard} >$ 120 GeV.

In Fig. 4.10 the same transverse energy distribution is shown for just the leading jet and the "second leading jet" (second-highest E_T jet in the event) for all the selected events; this distribution can be compared to the transverse energy distribution for leading and second leading jet from those events containing just 2 jets (see Fig. 4.11).

Similarly in Fig. 4.12 and 4.13, the jet transverse energy distribution is shown for events containing respectively just 3 jets and 4 jets.

In Fig. 4.14 the (η, ϕ) transverse energy map is shown for the event leading jet: the ECAL barrel ($-1.4 < \eta < 1.4$) is clearly covered by higher transverse energy jets than the endcaps, as expected.

Finally, the ratio between the two leading jets transverse energy sum and the total jet transverse energy in each event is distributed as in Fig. 4.15. Excluding those events with strictly 2 jets, the distribution can be fitted with a Gaussian with mean at about 0.76, that is to say 76% of the total jet energy is carried by the first two leading jets in the event.

At this point, it could be useful to put a threshold on the transverse energy of the leading-jet. In fact, 1 kHz of Level-1 bandwidth is expected to be allocated to an ECAL phi-symmetry calibration stream, using jets and minimum bias

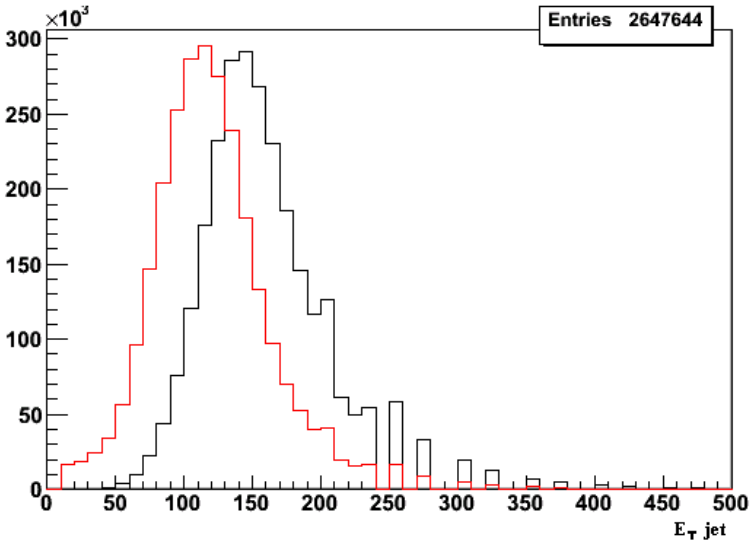

Figure 4.10: Transverse energy distribution for the leading jet (in black) and second leading jet (in red), for all selected events.

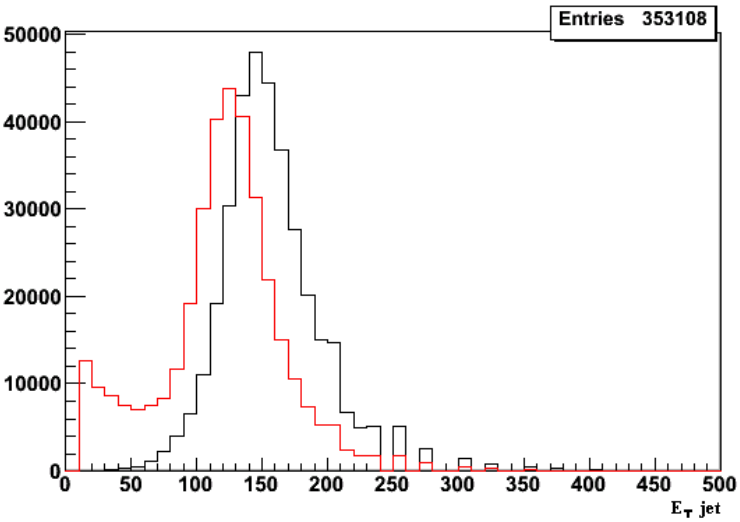

Figure 4.11: Transverse energy distribution for the leading jet (in black) and second leading jet (in red) for events containing just 2 jets; ; the distribution for the lowest E_T jet shows a low energy tail, assumed to be due to HCAL noise.

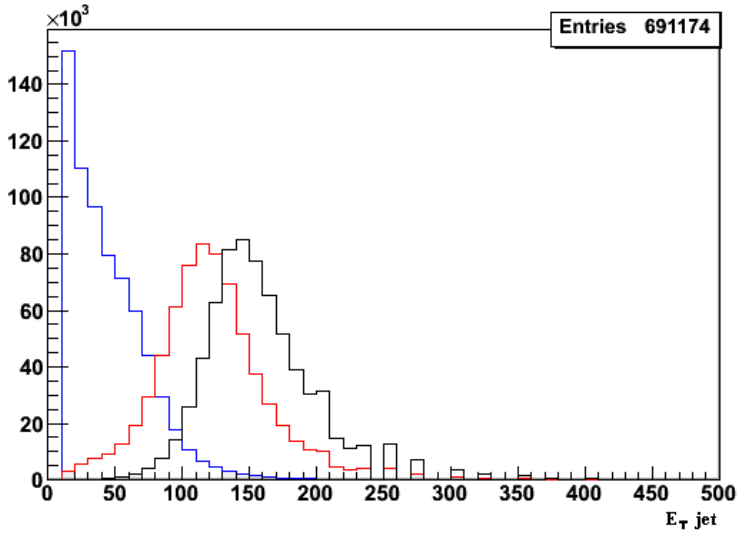

Figure 4.12: Jet transverse energy distributions, ordered in E_T, for events with just 3 jets; events selected from the $\hat{p_T}^{hard} > 120\ GeV$, trigger menu for a luminosity of $1pb^{-1}$. Again, the distribution for the third jet shows a noise tail, much more evident than in the previous plot due to the lower jet E_T.

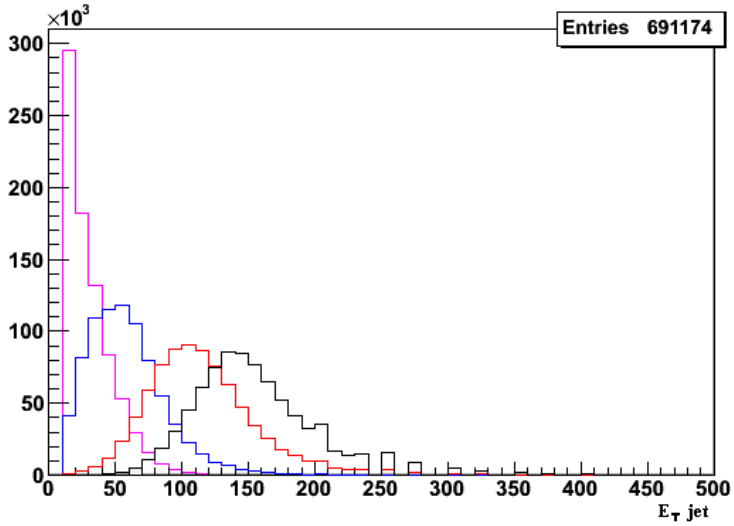

Figure 4.13: Jet transverse energy distributions, ordered in E_T, for events with just 4 jets; events selected from the $\hat{p_T}^{hard} > 120\ GeV$, trigger menu for a luminosity of $1pb^{-1}$.

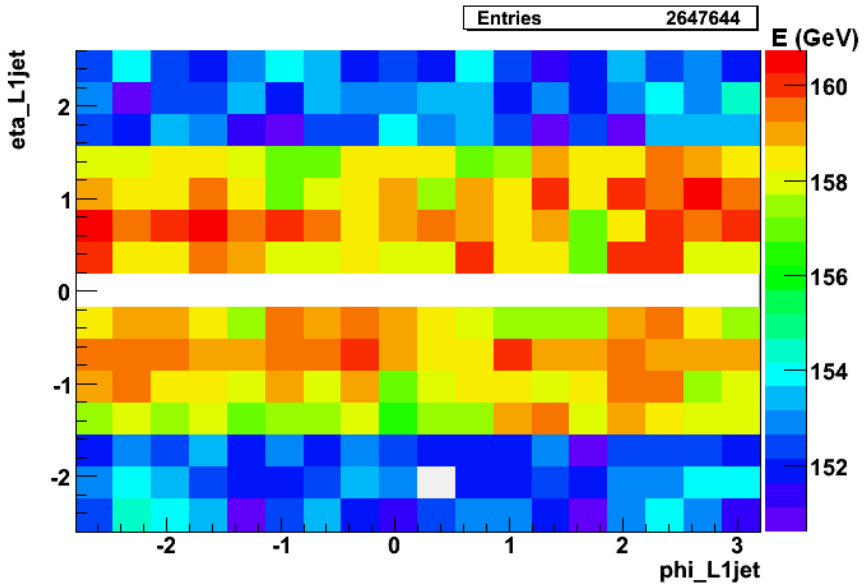

Figure 4.14: (η, ϕ) map for the leading jet, where the colour scale represents the jet transverse energy; events selected from the $\hat{p_T}^{hard} > 120GeV$ sample, trigger menu for a luminosity of $1pb^{-1}$. The barrel occupancy is higher than the endcap occupancy, since transverse energy is considered.

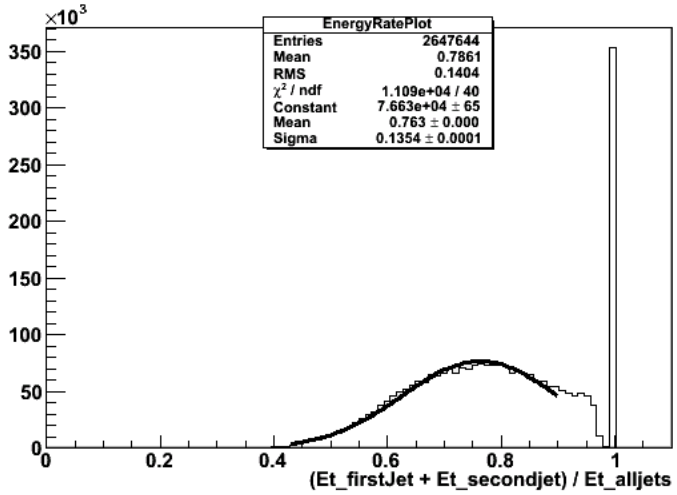

Figure 4.15: Ratio between the two leading jets transverse energy sum and the total jet transverse energy in each selected event.

events, but this bandwidth is saturated at high luminosity by low p_T jets. Thus a threshold should be put on the highest E_T jet, in order to collect only very high energy jets and to saturate the bandwidth in a relative short time: the threshold value depends on the instantaneous luminosity, according to the expected rate as shown in Tab. 4.3.

minimum $\hat{p_T}$ for hard scattering	cross section	rate (luminosity of $10^{30} cm^{-2} s^{-1}$)	rate (low lumi, $10^{32} cm^{-2} s^{-1}$)	rate (high lumi, $10^{34} cm^{-2} s^{-1}$)
30 GeV	160 μb	160 Hz	16 kHz	1.6 MHz
50 GeV	21 μb	21 Hz	2.1 kHz	210 kHz
80 GeV	3 μb	3 Hz	300 Hz	30 kHz
120 GeV	0.5 μb	0.5 Hz	50 Hz	5 kHz

Table 4.3: Expected rates for different $\hat{p_T}$-hard QCD processes, at various luminosity scenario.

Nevertheless, since the present work deals with an "early" start-up luminosity scenario, no cut is put on the leading jet transverse energy: otherwise, the QCD event rate would be considerably reduced, to the disadvantage of the intercalibration precision. In fact, the cut would result in only a small fraction of the generated events passing the threshold such that the remaining statistics would be insufficient to perform the study and a greater amount of time would be needed. For instance, the event rate is reduced to 26 Hz (at a luminosity of $10^{30} cm^{-2} s^{-1}$) if we require to have at least 2 Level-1 jets with $E_T > 40$ GeV in the QCD process (see also Section 1.3.3).

4.2.3 Selection of crystal energy deposits

Having selected the "good" events for further analysis and picked the right jet collections, the following step is to focus on the crystals energy deposits: every deposit should satisfy certain selection criteria (upper and lower energy thresholds); moreover it should be correctly associated to the L1-jets chosen.

Thresholds on crystal energy deposits A lower energy threshold is put in order to exclude noise: while for minimum bias events this threshold must be set just above the noise level, leading to the concerns already mentioned, the higher energies present in jet trigger events permit the choice of an increased value for the lower threshold. The ECAL rechit energy distribution obtained (see Fig. 4.16) is fitted with a Gaussian and the threshold is set at 255 MeV, that is about 4 σ. Likewise, the lower threshold for endcap energy deposits is set at 1 GeV (see Fig. 4.17).

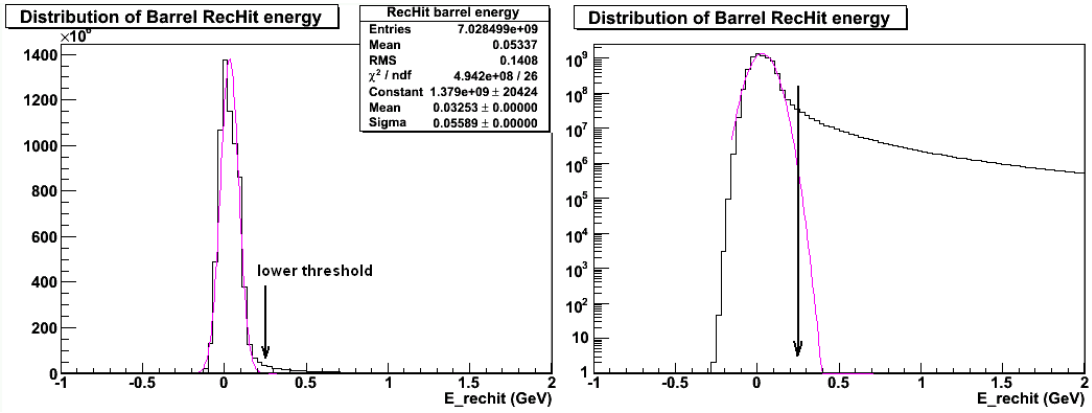

Figure 4.16: Barrel rechits energy distribution with the Gaussian fit (on the right, on logarithmic scale); events selected from the $\hat{p_T}^{hard} > 120GeV$ sample, trigger menu for a luminosity of $1pb^{-1}$.

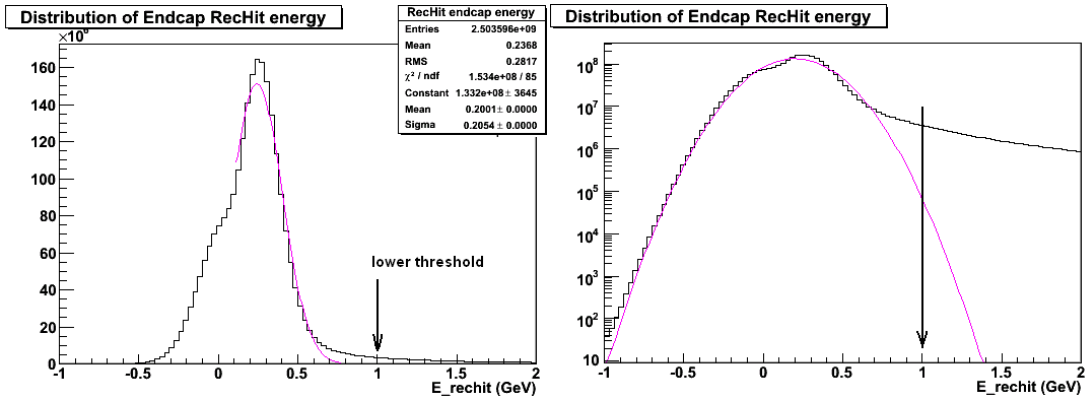

Figure 4.17: Endcap rechits energy distribution with the Gaussian fit (on the right, on logarithmic scale); events selected from the $\hat{p_T}^{hard} > 120GeV$ sample, trigger menu for a luminosity of $1pb^{-1}$.

Moreover, an upper threshold is needed to remove the low statistics tail at high energy. In fact, a few deposits with very high energy can have a significant effect on the value of the summed transverse energy in a crystal, later performed, and can affect the intercalibration precision. The upper threshold is chosen at 200 GeV for the barrel rechits and at 400 GeV for the endcap rechits, that is when the rechit energy distribution goes below ≈ 10 events in a billion. This upper threshold is strongly dependent on the statistical sample used and it is one of the parameters that must be optimized with real data.

In Fig. 4.18 the rechit energy distribution is shown up to the high energy tail.

Exclusion of the triggering jet Compared with the minimum bias choice, the main problem of a jet trigger event is the *trigger bias*: the choice of events where the energy deposits come from L1 trigger objects could bias the energy deposition itself, since the L1 decision is based on an energy computation. This bias could come from a HCAL miscalibration region or from an ECAL one. For this reason, it would be better to exclude from the event those objects which fired the trigger paths.
The Level-1 Trigger for jets works so that the energy associated with each calorimeter tower (ECAL plus HCAL) is compared to the energy associated to each other; the "regional candidate" consists then of a trigger tower with an energy higher than that of its neighbors. The Regional Calorimeter Trigger gives the candidate information to the Global Calorimeter Trigger, where the candidates are sorted and the 4 highest-energy ones are selected (see Section 2.4.4). They are used as an input for the physics trigger algorithm calculations and the final L1 decision is taken by applying a final `OR` to all the previously calculated algorithm bits. Since the used samples do not come from a specific trigger stream, but different trigger bits appear to be fired in each event, and moreover all the L1 jets could in principle have fired at least the `SingleJet15` stream, there is not any simple way to establish which jet should be excluded from the analysis.
In spite of that, the highest-E_T jet could be associated to a trigger tower with crystals miscalibrated more probably than all the other L1-jets in the event: this fact would lead to a bias in the energy sum per ring (at η fixed). Therefore, as a first analysis approach, the highest-E_T jet in the event is excluded: that is, *the energy deposits associated with the leading jet do not contribute to the total energy deposit in a given crystal.*
To perform this exclusion, the ΔR quantity is used, defined as

$$\Delta R = \sqrt{\Delta\eta^2 + \Delta\phi^2}$$

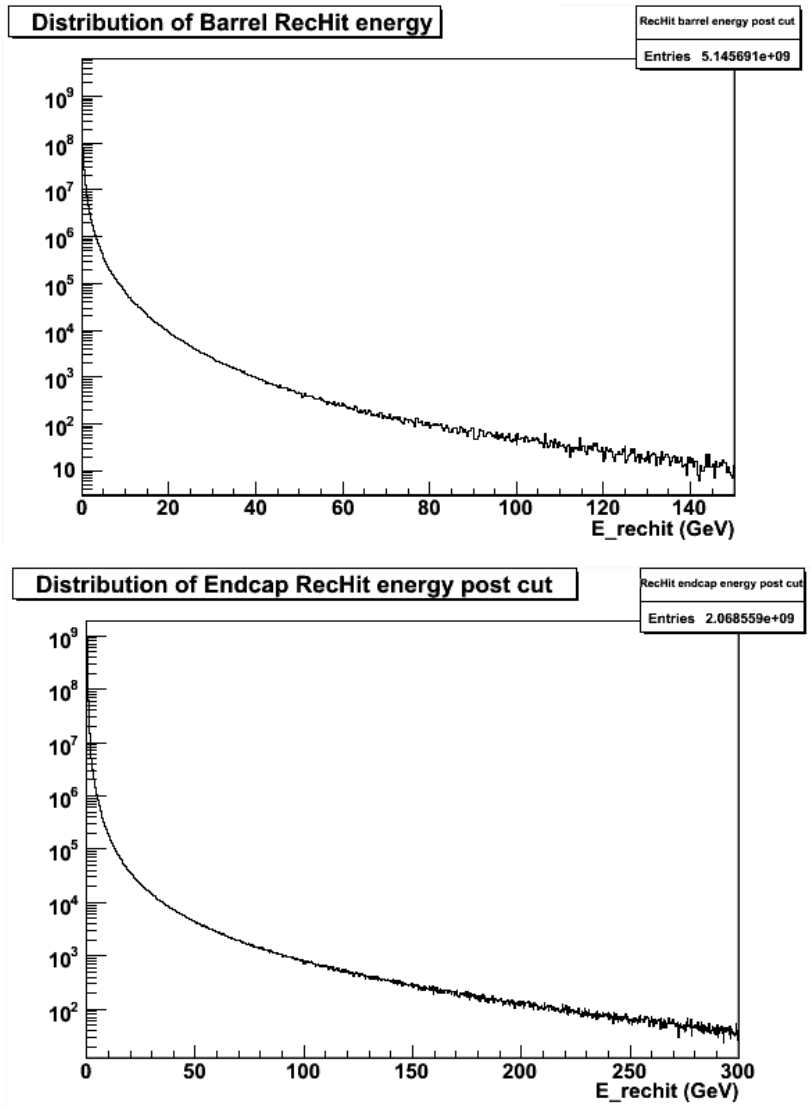

Figure 4.18: Rechits energy whole distribution for events selected from the $\hat{p_T}^{hard} > 120GeV$ sample, trigger menu for a luminosity of $1pb^{-1}$; on top, barrel rechits distribution, on bottom, endcap rechits distribution.

where $\Delta\eta$ and $\Delta\phi$ are the differences in η and ϕ respectively between the position of a crystal hit (energy deposit) and the position of the leading jet in the event. As for the position of the jet, it is defined to be the centre of the L1-trigger region containing the jet[7] (see Section 2.4.4). The value of the cut on ΔR is chosen after examining the distribution (see Fig. 4.19) of this variable for all crystal hits satisfying the energy thresholds mentioned in the previous section.

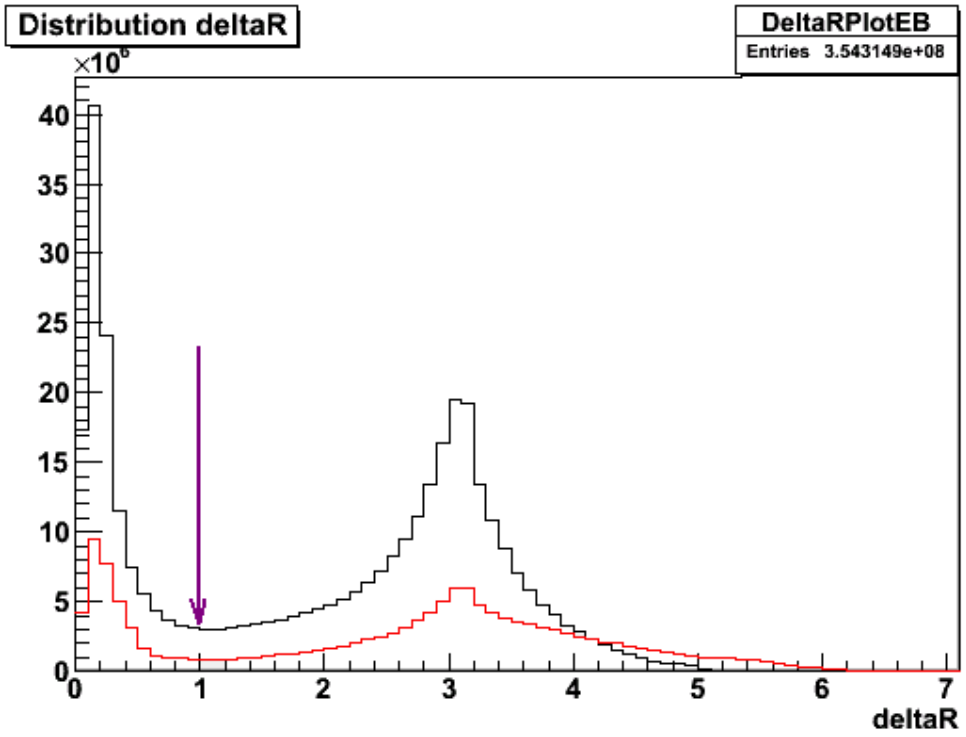

Figure 4.19: ΔR distribution for all ECAL crystal rechits, after the energy thresholds applied; events selected from the $\hat{p_T}^{hard} > 120GeV$ sample, trigger menu for a luminosity of $1pb^{-1}$. The black histogram refers to the barrel crystals and the red histogram to the endcap ones.

The peak at low ΔR corresponds to hits from the leading jet, while the peak at $\Delta R = \pi$ corresponds to hits coming from the second highest-E_T jet in the event, approximately back-to-back in ϕ if the event contains only 2 jets. The second peak is wider because of the events containing more than 2 jets: for these events, actually, hits not coming from the leading jet can span the whole ϕ range. Thus, a cut at

$$\Delta R \geq 1rad$$

[7]remember that a calorimeter trigger region is a 4×4 array of trigger towers; in the barrel, each trigger tower consists of 5×5 ECAL crystals and there is a full match between ECAL and HCAL trigger towers

is applied to exclude hits coming from the highest E_T jet.

4.2.4 Determination of the intercalibration coefficients

As already mentioned, under the assumption of a rotational symmetry in ϕ, the intercalibration can be performed by comparing the total energy deposited in each crystal with the mean of the distribution of total energies for all crystals at that pseudorapidity. But also the CMS detector can be considered symmetric about $\eta = 0$, so the activity should be the same for all crystals at the same absolute η, that is all crystals within the two rings at equal distances at either side of $\eta = 0$.
The first step is then to compute all the transverse energy sums for each barrel crystal, using the transverse energy deposits from all the selected events. Then, for each of 85 pairs of rings in the barrel, the distribution of the truncated[8] E_T sums ΣE_T for all crystals (720) within the pair of rings is produced. Each distribution is fitted with a Gaussian in order to measure the mean value. In Fig. 4.20 examples of ΣE_T fitted distributions are shown for different values of $|\eta|$.

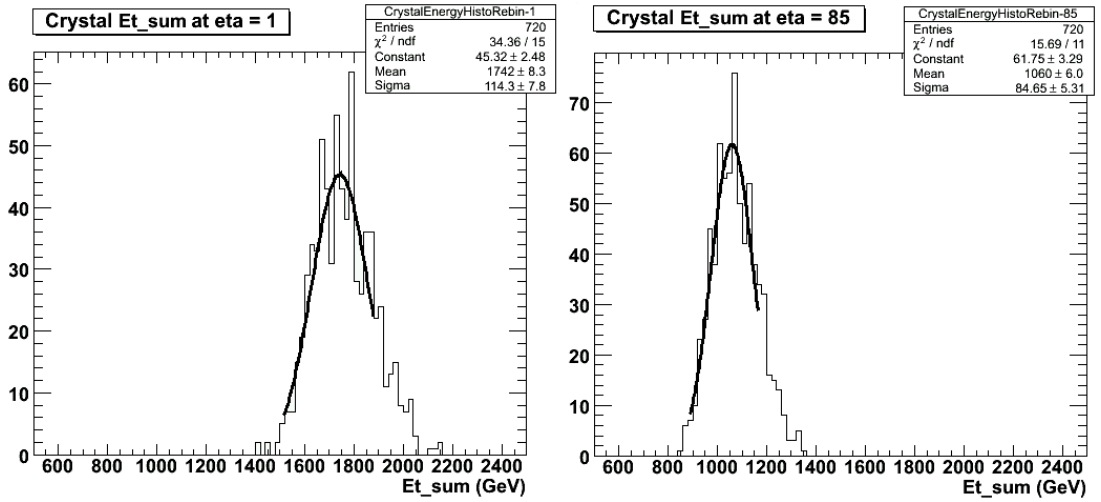

Figure 4.20: ΣE_T fitted distribution for all crystals within the pair of rings at two different $|i\eta|$ values.

A secondary peak or a right tail in the ΣE_T distribution at higher ΣE_T is evident (see Fig.4.21): it is due to higher entries from the crystals (18 in each ring) on one side of each inter-module gap. In fact, as a consequence of the arrangement of crystals in the ECAL barrel (they are 3°off-pointing), crystals

[8]due to the upper and lower thresholds applied to the rechit deposits

on one side of an inter-module gap receive a greater number of hits than other crystals (see Fig. 4.22). To exclude this right tail, the Gaussian function is shifted toward lower ΣE_T values.

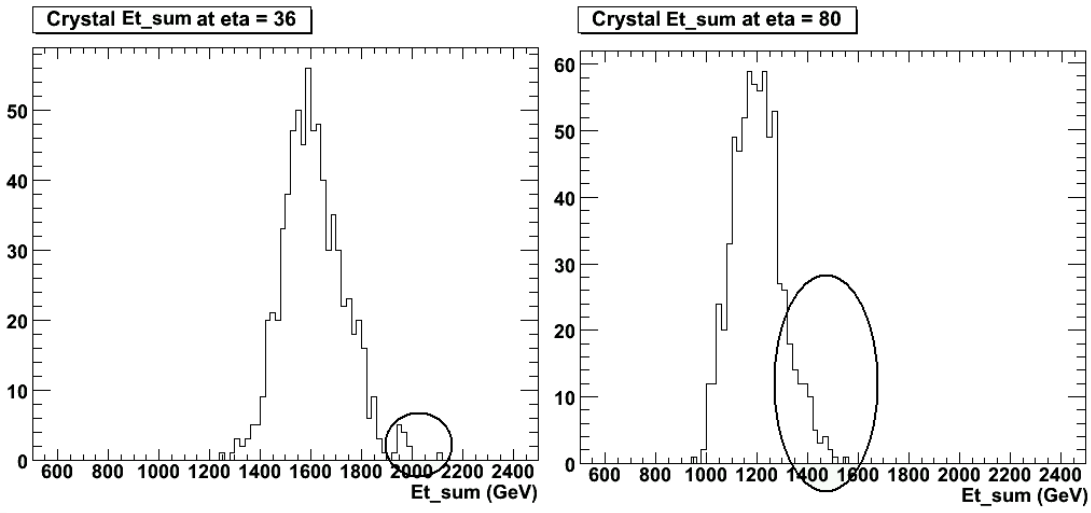

Figure 4.21: On the left, ΣE_T distribution for all crystals within the pair of rings at $|i\eta| = 36$; on the right, ΣE_T distribution for all crystals within the pair of rings at $|i\eta| = 80$; respectively, a small "second peak" and a right tail are pointed out by a circle.

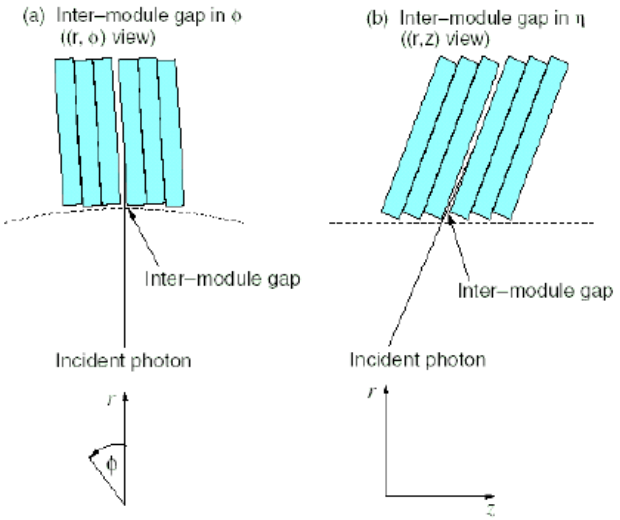

Figure 4.22: Effect of the presence of inter-module gaps.

Energy sum variations. In Fig. 4.23 the 3D $(i\eta, i\phi, \Sigma E_T)$ histogram for the collected transverse energy sums is shown: the ΣE_T clearly varies as a function of

η. This is the result of different factors, for instance, the jet processes kinematic.

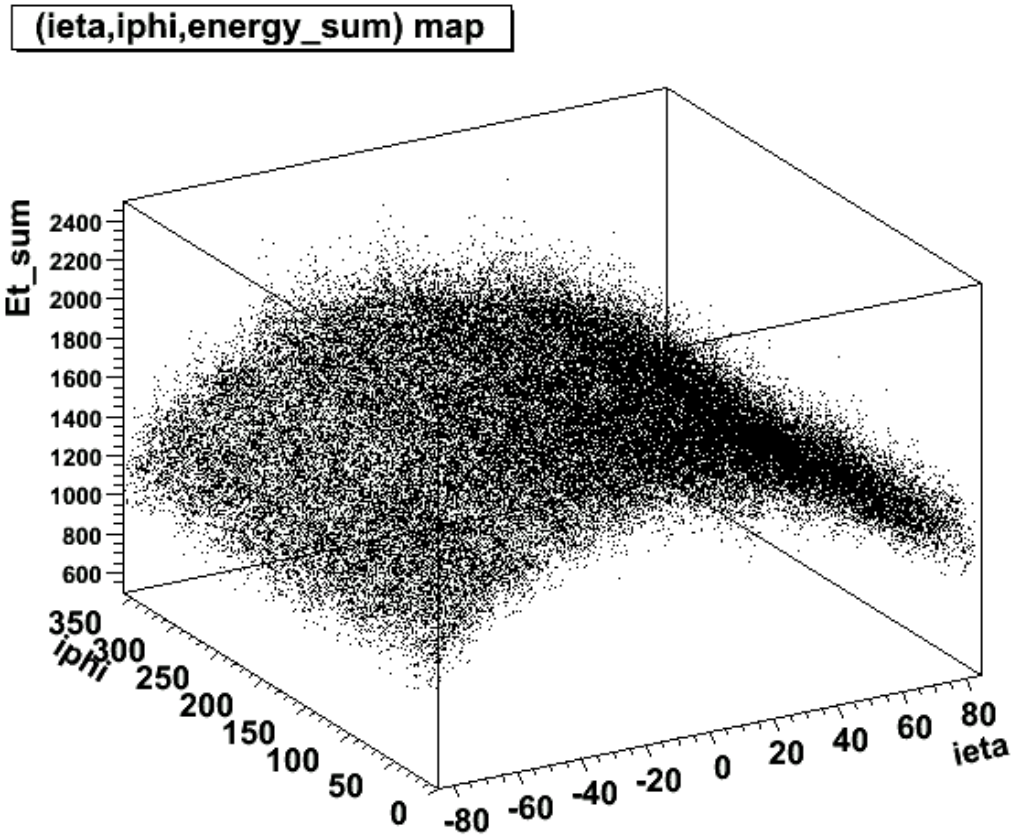

Figure 4.23: 3D $(i\eta, i\phi, \Sigma E)$ map.

Fig. 4.24 shows the $(i\eta, i\phi)$ map for the collected E_T energy sums, normalized on the transverse energy sum relative to a crystal of reference (chosen at $i\eta$=1, $i\phi$=1). The grid-like pattern is due to two effects: the vertical rows with a greater amount of collected energy fit the module η-gaps pattern, since crystals on one side of inter-module η-gaps receive a greater number of hits than other crystals. The (less evident) horizontal rows correspond to the supermodules boundaries over ϕ and thus reveal the supermodules geometry.

In Fig. 4.25 the variation of ΣE_T with $i\eta$ is shown (the histogram pattern due to the module η-gaps pattern is evident), whilst in Fig. 4.26 the variation of ΣE_T with $i\phi$ is shown for all crystals in the pair of rings at $|i\eta|$=1.

The intercalibration coefficients. Finally, the intercalibration constants are estimated dividing the total ΣE_T collected in each crystal by the Gaussian mean of the same pair of rings ΣE_T distribution:

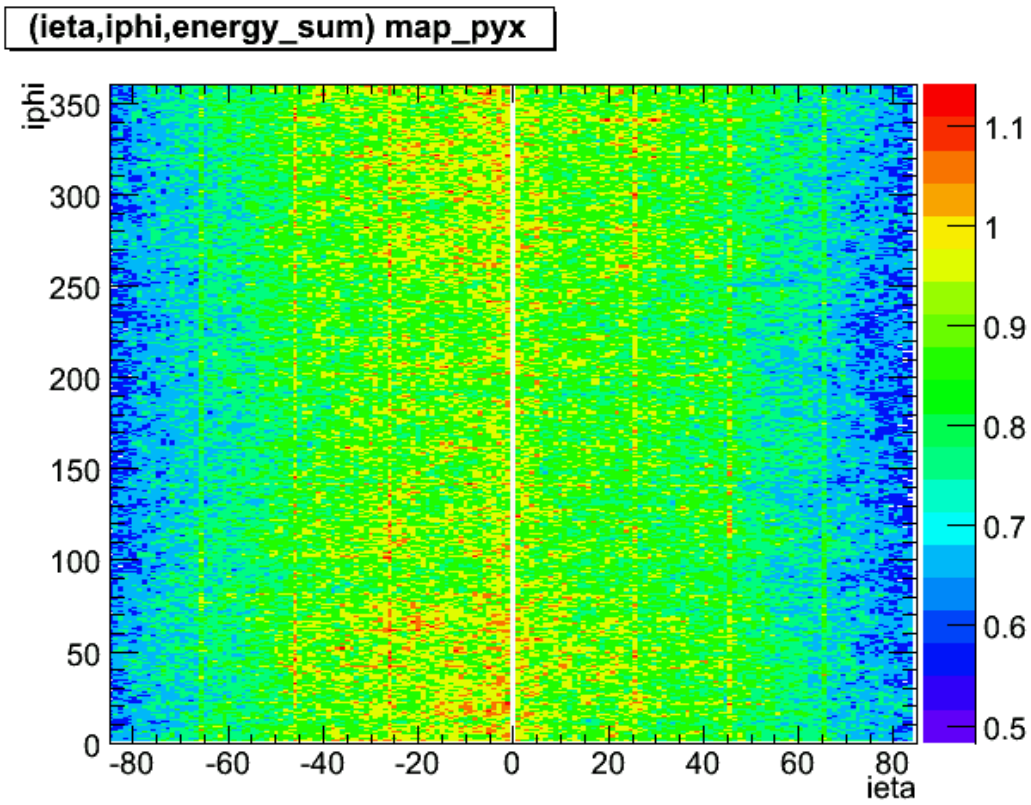

Figure 4.24: $(i\eta, i\phi)$ map for the collected E_T sums (on the coloured scale), normalized on the ΣE_T relative to the crystal at $i\eta$=1, $i\phi$=1.

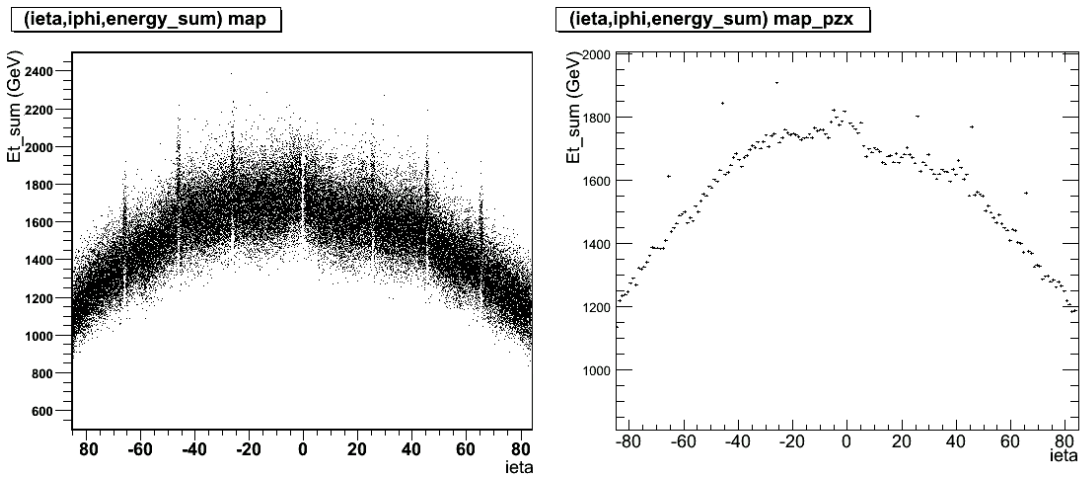

Figure 4.25: On the left, variation of ΣE_T with $i\eta$; on the right, the profile of the same histogram is shown.

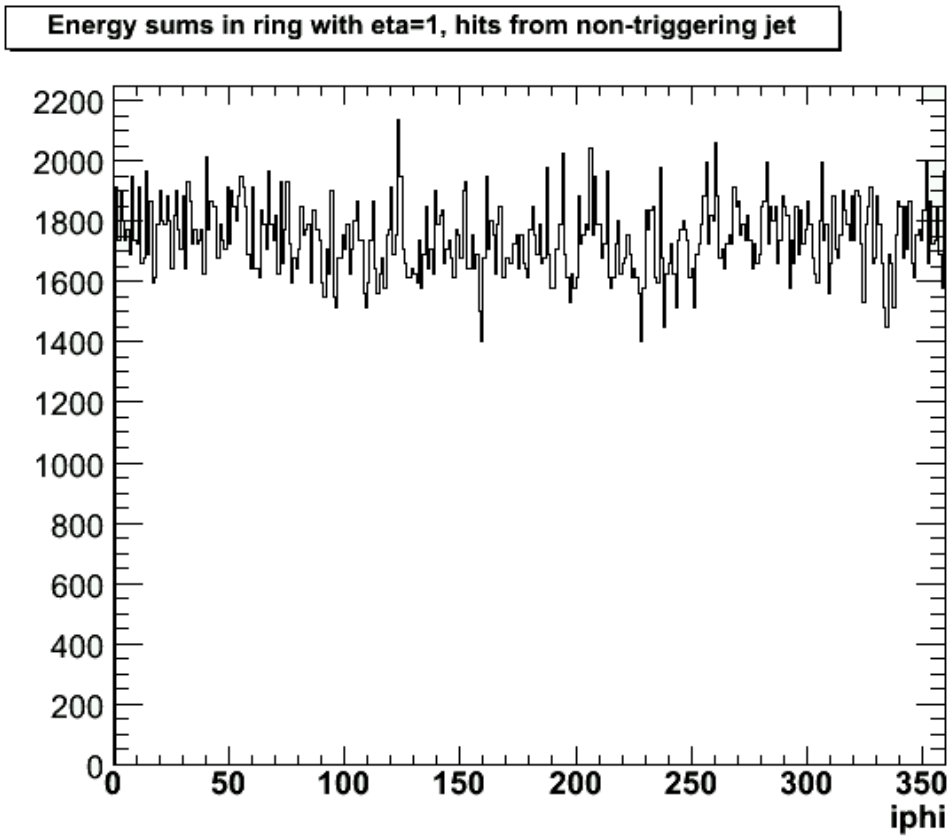

Figure 4.26: Transverse energy sums distribution for all crystals in rings at $|\eta| = 1$.

$$c_i \;=\; \frac{(\sum E_T)_i}{(\sum E_T)_{mean}}$$

In this way, the constants are factors by which an energy deposit must be divided, in order to obtain a "calibrated rechit". To have the "official" multiplicative factors, the constants must be inverted.

4.2.5 Corrections and determination of the intercalibration precision

The Gaussian width of the ΣE_T distribution should in principle represent the intercalibration precision. However, due to the fact that the E_T sum is obtained from a truncated E_T distribution (with a lower and an upper energy thresholds as explained in section 4.2.3), this is not true anymore.

Correction for the E_T truncation. The Gaussian width of the ΣE_T distribution for the crystals in a pair of rings is proportional rather than equal to the intercalibration precision. The constant of proportionality is determined empirically from the relationship between the size of an applied miscalibration and the resulting fractional change in ΣE_T. In fact, a small change in the calibration constant of a crystal will result in a proportional change to the measured ΣE_T in that crystal, with a constant of proportionality not equal to 1.0.
A miscalibration ϵ_M varying between +5% and -5% is applied to each crystal, event per event, multiplying the crystal energy deposit by $(1 + \epsilon_M)$; then, the total E_T sums are re-calculated for each crystal for all selected events, after lower and upper thresholds. The distribution of the fractional change ϵ_T in the total energy measured versus the miscalibration ϵ_M is provided for each pair of rings at $|\eta|$ fixed; ϵ_T is linearly proportional to ϵ_M and the constant of proportionality (the so-called k-factor) is found to be close to 1.1 for all rings of crystals in the ECAL barrel; with aproximately no variations over η.
In Fig. 4.27 the fractional change in the total energy measured as a function of ϵ_M is shown for all crystals in the two rings at $|\eta| = 1$. For the range of miscalibrations shown, the relationship between ϵ_T and ϵ_M is given by a straight line with a slope 1.08; that is a miscalibration of 10% changes the total energy observed by 10.8%.

The intercalibration precision which can be obtained for each pair of rings is then given by the Gaussian width of the ΣE_T distribution divided by k.

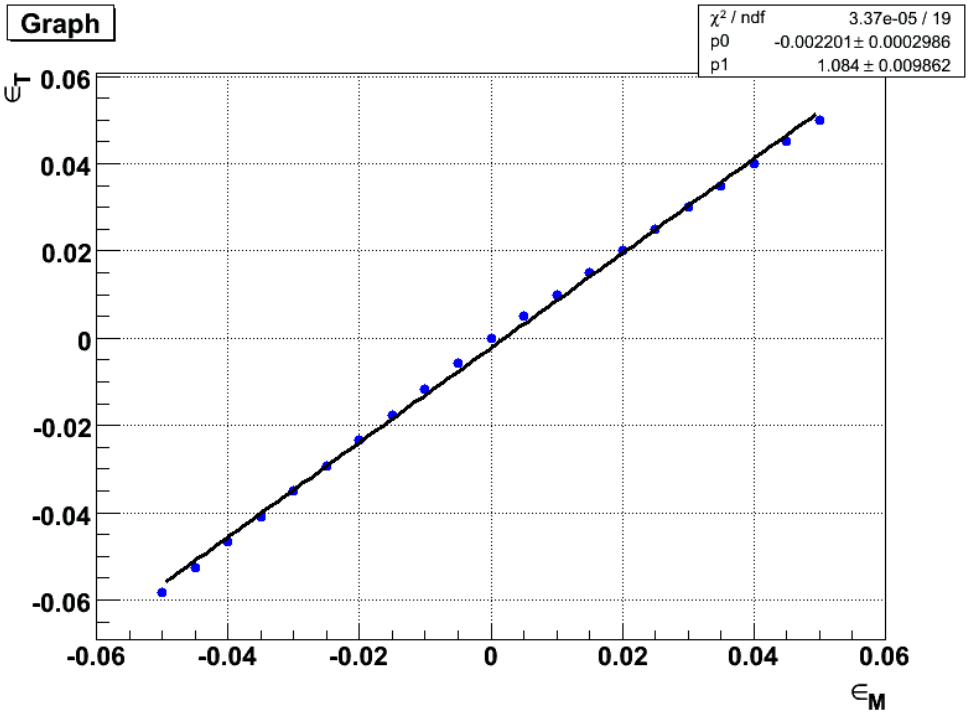

Figure 4.27: Fractional change ϵ_T in the total energy measured as a function of the introduced miscalibration ϵ_M, for crystals in the two rings at $|\eta| = 1$.

The corrected intercalibration coefficients. Before evaluating the intercalibration precision, the intercalibration coefficients must be corrected according to the measured k-factors:

- for each crystal, the corrected "miscalibration" is calculated using the k-factor of the relative ring, as

$$\epsilon'_M = \frac{\left(\frac{\Sigma E_T}{\langle \Sigma E_T \rangle} - 1\right)}{k}$$

- the corrected multiplicative calibrations are then calculated as

$$c_i^{new} = \frac{1}{\epsilon'_M + 1}$$

In Fig. 4.28 the $(i\eta, i\phi)$ map for the obtained constants is shown.

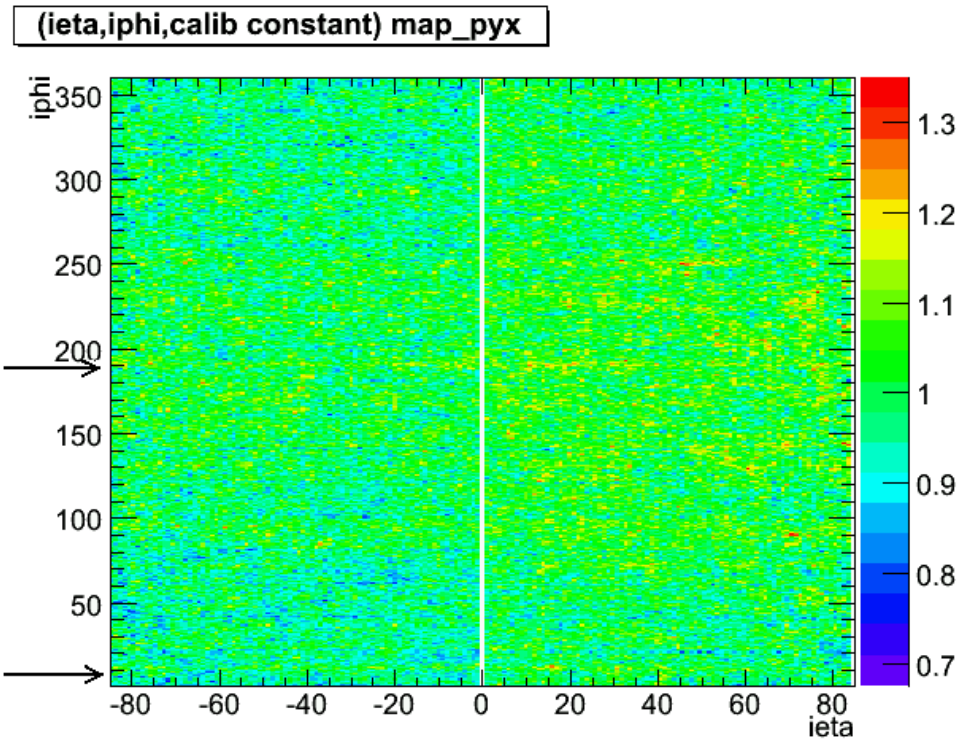

Figure 4.28: $(i\eta, i\phi)$ map for the intercalibration corrected constants (on the coloured scale); the two arrows highlight the features at $i\phi = 10°$ and $i\phi = 190°$ due to the material budget in front of ECAL.

In Fig. 4.29 and Fig. 4.30, the variation of c_i constants respectively with $i\eta$ and $i\phi$ is shown: the variation of c_i with $i\phi$ shows a particular pattern (narrow peaks every 20 degrees) which fits the supermodule ϕ-gaps pattern, while at $i\phi = 10°$ and $i\phi = 190°$ two features at higher c_i can be attributed to the material budget in front of ECAL (two rails used for the insertion of the Tracker are placed at that azimuthal position). The same features can be found in the calibration map of Fig. 4.28.

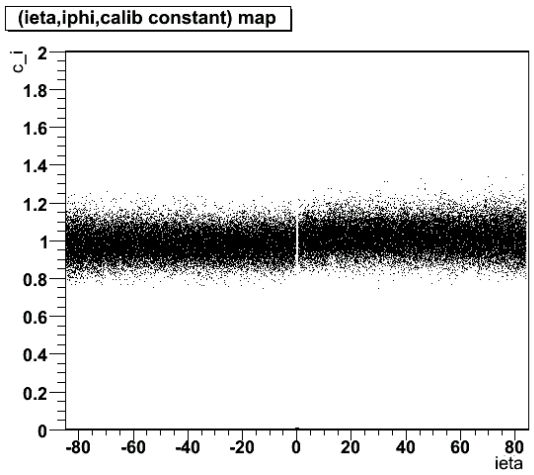

Figure 4.29: Variation of c_i constants with $i\eta$.

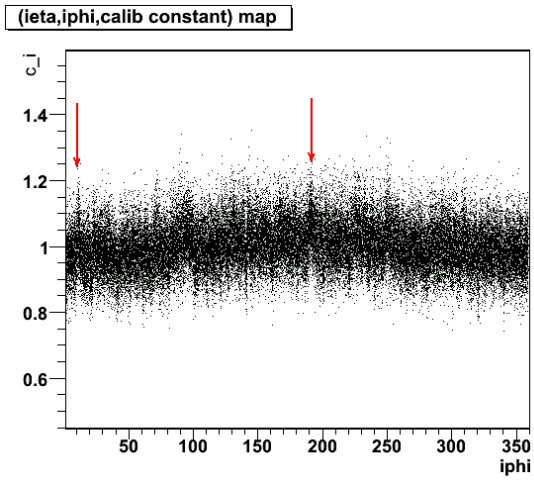

Figure 4.30: Variation of c_i constants with $i\phi$.

Intercalibration precision and comparison with the original calibrations
Finally, the technique is tested comparing the obtained calibration constants to the original ones, provided by laboratory measurements and suitable for a start-up luminosity scenario. For each crystal, the ratio

$$R = \frac{c_i^{old}}{c_i^{new}}$$

is calculated, and the distribution of R for each pair of rings is provided and fitted with a Gaussian. The gaussian width of the distribution is an estimate of the intercalibration precision.

In Fig. 4.31 the ratio R distribution is shown for all crystals at $|i\eta| = 1$, while in Fig. 4.32, the values of distribution widths is shown as a function of η. The trend reveals the energy deposition dependence from the variation with η of the amount of material between the interaction point and ECAL. The obtained precision of about 7% (increasing up to 8% for higher η values) is much more worse than expected , due to the very low statistics.

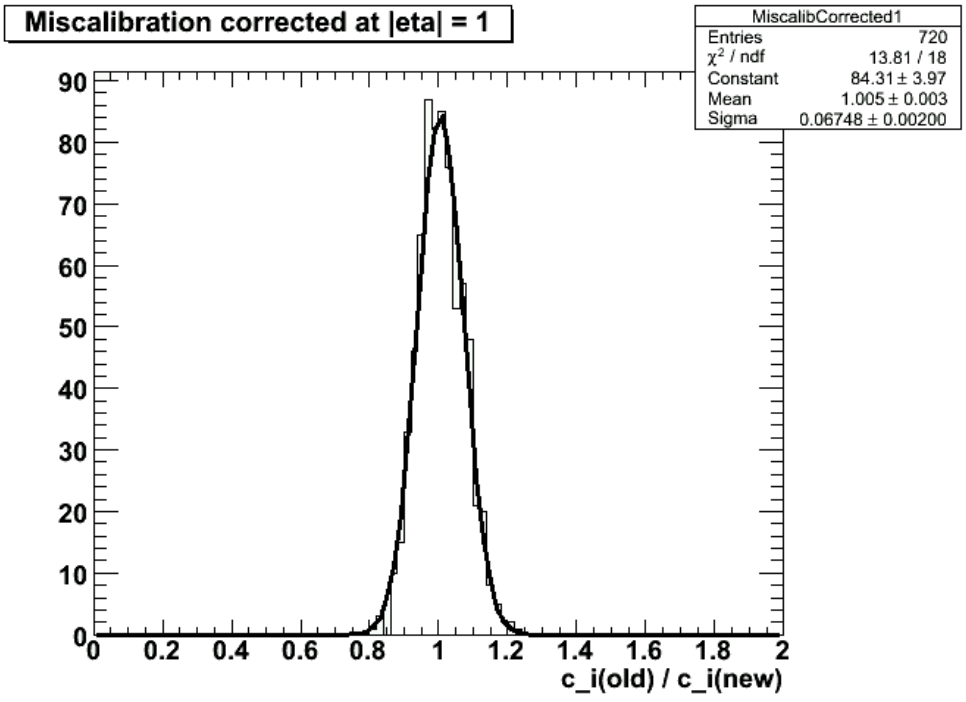

Figure 4.31: Distribution of the quantity c_i^{old}/c_i^{new} for all crystals within the ring at $|i\eta| = 1$.

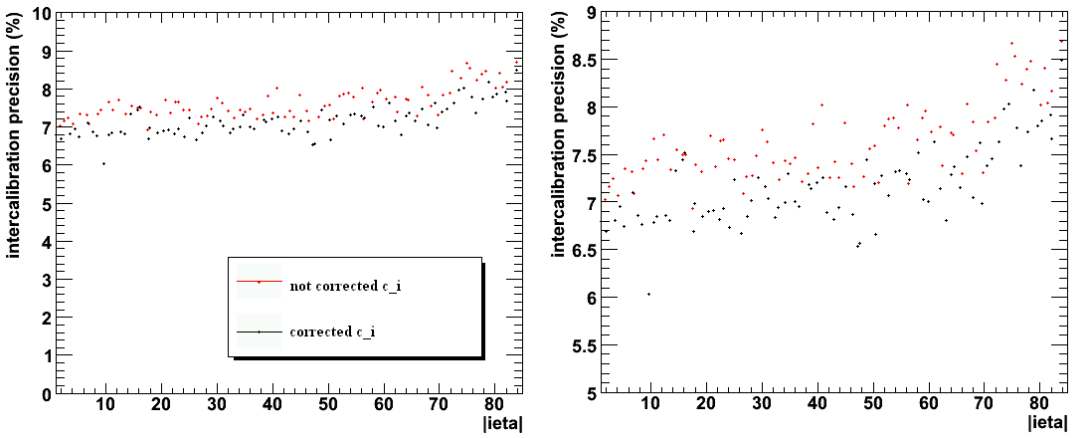

Figure 4.32: On the left, intercalibration precision before (red marker) and after (black marker) the correction applied using the k-factors; on the right, a zoom of the same histogram is shown.

4.2.6 Intercalibration including all jets

Due to the fact that the energy deposits associated with the highest E_T jet have not been used to calculate the energy sums for each crystal, a bias could have been introduced in the algorithm. In order to verify the real existence of this bias, the previously described procedure is repeated using all the ECAL barrel energy deposits, only applying the upper and lower energy thresholds.
Fig. 4.33 shows the $(i\eta, i\phi)$ map for the collected E_T energy sums, normalized to the transverse energy sum relative to the crystal at ($i\eta$=1, $i\phi$=1); while in Fig. 4.34 the $(i\eta, i\phi)$ map for the obtained calibration constants is presented, after the k-factor correction. The spread around $c_i \approx 1$ appears to be smaller, and this is also evident in Fig. 4.35, where the calibration constants variation over η is presented. This is clearly due to the higher available statistics in terms of collected rechits (higher energy sums value obtained for each crystal).

For the same reason, the intercalibration precision (see Fig. 4.36) is much more improved (≈4-5% after the k-factor correction): an expected $\approx \sqrt{2}$ improvement is clearly seen.

Please note that the transverse energy sums distribution is no more affected by the oscillation over ϕ appeared in Fig. 4.26: the same plot is reproduced in Fig.4.37.

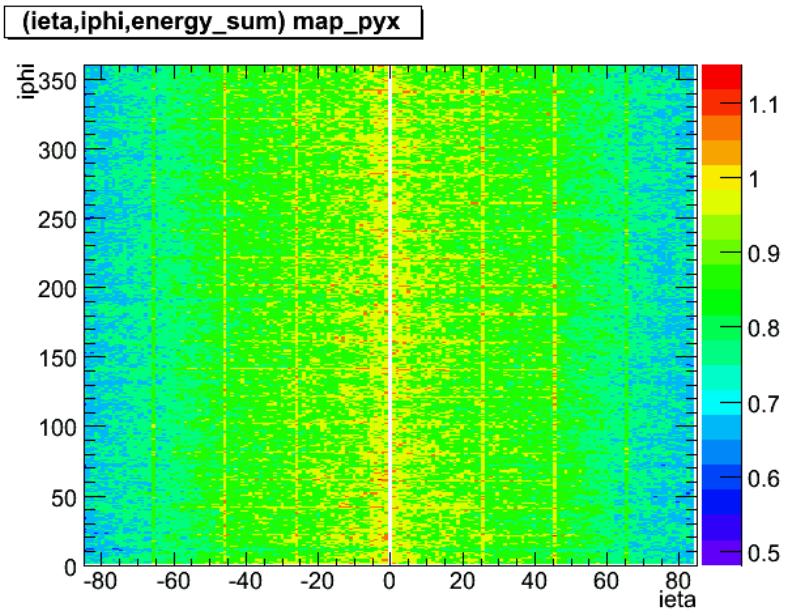

Figure 4.33: $(i\eta, i\phi)$ map for the collected E_T sums (on the coloured scale), normalized on the transverse energy sum relative to the crystal at ($i\eta$=1, $i\phi$=1).

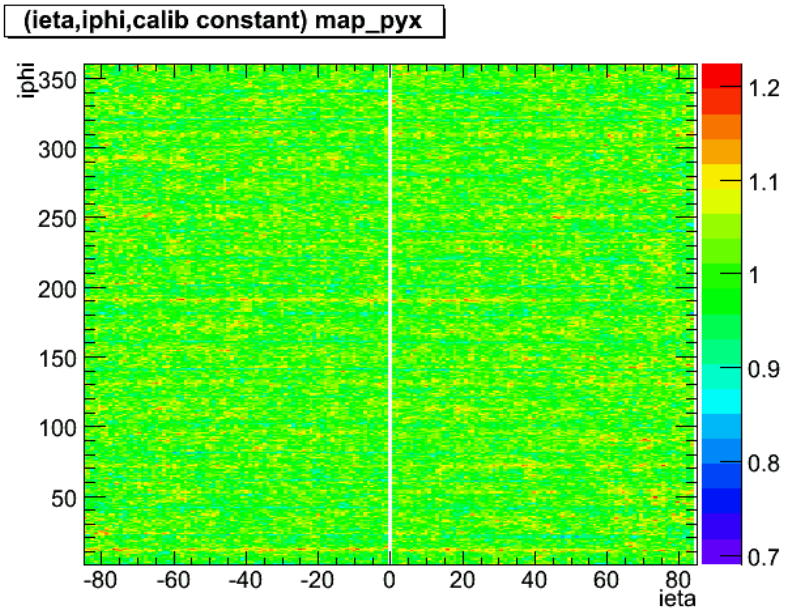

Figure 4.34: $(i\eta, i\phi)$ map for the intercalibration coefficients (on the coloured scale).

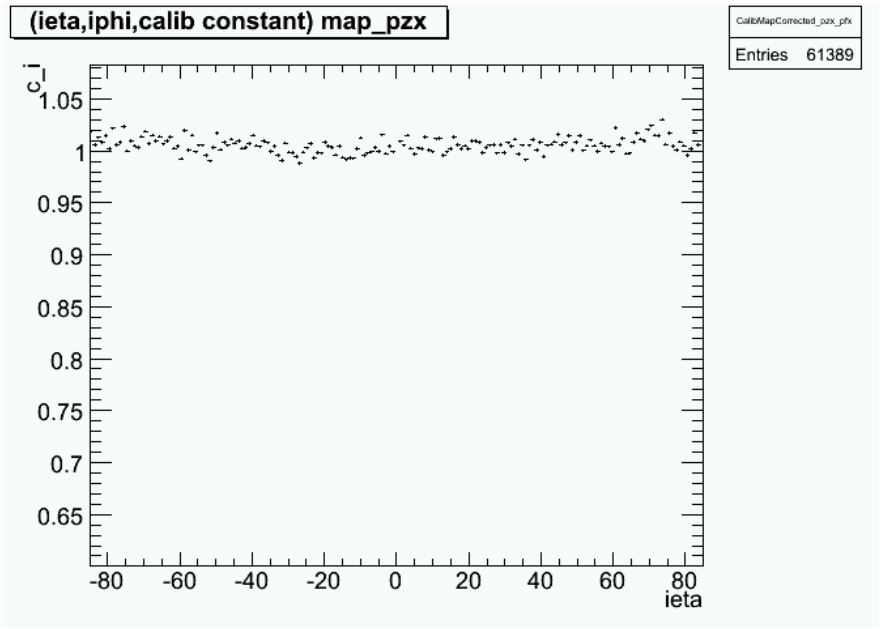

Figure 4.35: Variation of c_i constants with $i\eta$.

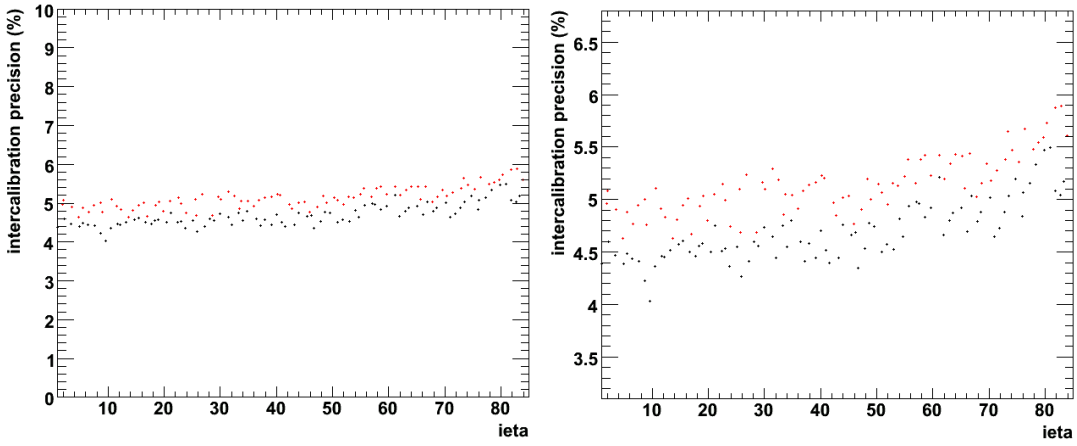

Figure 4.36: On the left, intercalibration precision before (red marker) and after (black marker) the correction applied using the k-factors; on the right, a zoom of the same histogram is shown.

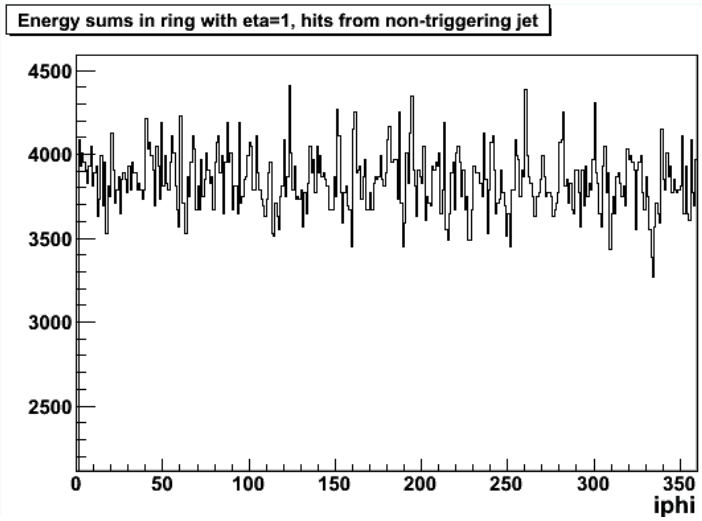

Figure 4.37: Transverse energy sums distribution for all crystals in rings at $|i\eta| = 1$.

4.2.7 Conclusions and outlook

This work demonstrate the feasibility of the jet trigger ϕ-symmetry intercalibration method. Nevertheless, this study has been performed on events generated at fixed bins of hard scattering transverse momentum ($\hat{p}_T^{hard}$) and the algorithms will need to be tuned with real data. The main goal is to achieve a good balance between the statistical precision of the intercalibration constants and the need of collect high transverse energy in ECAL. A specific jet trigger path must be used to select the most appropriate events for the ϕ-symmetry calibration.

To estimate the jet trigger rate, the QCD cross section as a function of $\hat{p}_T^{hard}$ can be used. It has been shown the strong correlation between the event $\hat{p}_T^{hard}$ and the E_T peak of the highest energy jet. Therefore, by tuning the E_T threshold at the L1 trigger level, a rough jet trigger rate estimate can be done. The main constraint is the 1 kHz trigger bandwidth limit assigned to the calibration stream. The expected QCD rate for $\hat{p}_T > 15$ GeV at $\mathcal{L} = 10^{30} cm^{-2} s^{-1}$ is of the order of 2.5 kHz; a two-jets trigger requirement will strongly reduce this rate. At higher luminosities, a `DoubleJetXX` trigger path with different E_T thresholds (`XX`) must be exploited to reduce the rate to an acceptable level. As can be seen in Fig. 4.38, with a sample produced at $\hat{p}_T > 120$ GeV and a luminosity of $1 pb^{-1}$, ≈94% of events pass the `DoubleJet70` L1 filter, while ≈72% pass the `DoubleJet100`. By selecting a $\hat{p}_T > 80$ GeV, the `DoubleJet100` path reduces the sample to ≈50%.

To obtain the statistics of ≈10 M events, necessary to reach a precision of

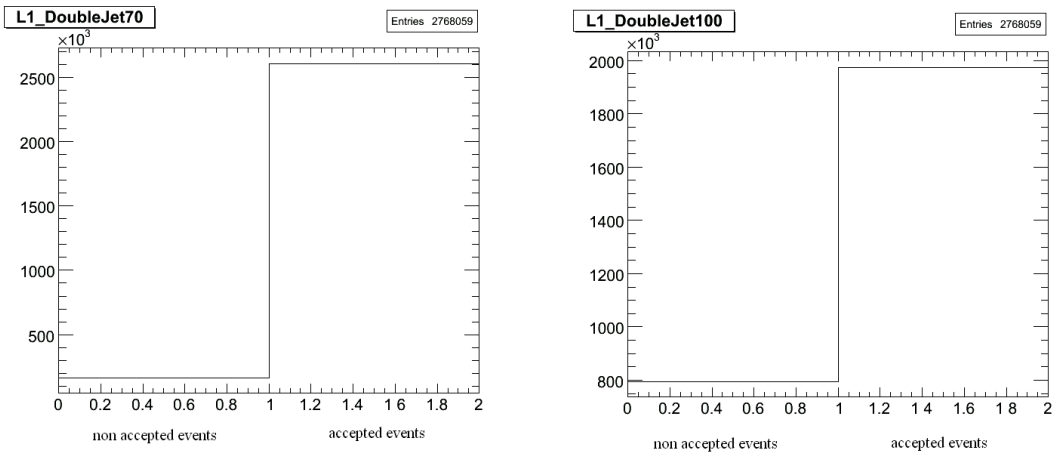

Figure 4.38: Comparison between the number of $\hat{p}_T > 120$ GeV events which do not pass the L1 trigger requirements (left bin) and the number of events which pass the same trigger requirements (right bin); the same comparison is provided for `DoubleJet70` path (left plot) and `DoubleJet100` path (right plot).

about 2%, few days of data taking will be sufficient at a luminosity greater than $10^{31} cm^{-2} s^{-1}$. Nevertheless, the algorithm can be tuned since startup and the trigger thresholds will be optimized as the luminosity increases.

Chapter 5

HLT efficiency measurement on $H \rightarrow ZZ^{(*)} \rightarrow 4e$ events

One of the most promising channels for the search of the Higgs boson at the LHC is the single production mode followed by a decay in a $ZZ^{(*)}$ pair. This inclusive process $pp \rightarrow H + X \rightarrow ZZ^{(*)} + X$ is on the critical path of a discovery at the LHC, over an extended range of possible m_H values; in fact, the value of m_H is a free parameter of the SM which must be constrained by experiments. This chapter presents the triggering steps for data reduction focusing on the decay chain $H \rightarrow ZZ^{(*)} \rightarrow e^+e^-e^+e^-$. In particular, my work was to measure the High Level Trigger (HLT) efficiency for this specific channel. Thus, the signal and background processes are initially detailed, together with the electron reconstruction and high level trigger algorithm chosen. The efficiency measurements and HLT output rates obtained for different Higgs mass samples are then presented, together with some preliminary results concerning the background processes for a 4 electrons final state channel. The work focuses on the start-up luminosity scenario of $10^{32} cm^{-2} s^{-1}$.

5.1 Signal and background processes

The inclusive single Higgs boson production benefits from a high production cross-section at the LHC of about $40 \cdot 10^3$ fb (NLO) at $m_H = 130$ GeV/c^2, decreasing monotonically for higher m_H. The production cross-section is dominated ($> 80\%$) in this mass range by gluon-gluon fusion processes via triangular loops involving heavy quark (mostly the top quark) flavours. The branching ratio in the SM for the $H \rightarrow ZZ^{(*)}$ decay is sizeable ($> 1\%$) for any Higgs mass value above about 115 GeV/c^2. It rises to a peak value above around 150 GeV/c^2 and

is suppressed around $m_H \approx 2 \cdot m_W$. For $m_H = 2 \cdot m_Z$, it reaches a plateau of 20 to 30%. The $ZZ^{(*)}$ contribution, i.e. with at least one Z boson on its mass shell, is greater than 50% for $m_H > 115$ GeV/c^2, and greater than 85% for $m_H > 150$ GeV/c^2. Thus, the $H \rightarrow ZZ^{(*)} \rightarrow e^+e^-e^+e^-$ (in short H $\rightarrow$ 4e) channel offers a possibly significant, very clean and simple multi-lepton final state signature.
A main background source of four electrons final states arises from non-resonant SM continuum production of $Z^{(*)}/\gamma Z^{(*)}/\gamma$ and the production of real ZZ pairs which proceeds dominantly via quark-antiquark annihilation. This constitutes an irreducible background which will be hereafter referred to as the "$ZZ^{(*)}$" background. Other 4e background sources come from pair production of heavy quark flavours such as the $t\bar{t}$ production and the $Z^{(*)}/Zb\bar{b}$ associated production mediated by QCD, and which proceeds dominantly via gluon-gluon fusion. These will be hereafter referred to as the $t\bar{t}$ and "$Zb\bar{b}$" background processes. Additional contributions could in principle come from misidentified 4e events in which "fake primary electrons" are reconstructed due to early photon conversions in the CMS detector, or are produced in QCD jets from leptonic and semi-leptonic meson and baryon decays or from $\pi^0\pi^\pm$ hadron overlaps. A potentially dangerous misidentified background comes from Z+jet(s) Drell-Yan production at NLO in which the Z boson recoils against the jet(s). The suppression of the Z + jet(s) background via electron identification and kinematics is provided by high level studies.

5.1.1 Simulated samples

All signal and background processes are simulated for pp collisions at the LHC at a centre-of-mass energy of 14 TeV with no pile-up conditions from multiple collisions, as expected in the start-up luminosity configuration. The $H \rightarrow 4e$ signal samples are generated with `PYTHIA`, the detector geometry is simulated via `GEANT4` and the reconstruction in provided in `CMSSW_1_3_1`. The Higgs boson is produced via either gluon fusion or weak boson fusion processes, and forced to decay into a Z boson pair. The Z bosons are subsequently forced to undergo a decay in a 4 leptons final state. The event sources used for the measurements are three sets of samples of $H \rightarrow ZZ^* \rightarrow 4l$ events, with Higgs masses 140 GeV, 160 GeV and 170 GeV, and one $H \rightarrow ZZ^* \rightarrow 4e$ sample with a higher Higgs mass of 190 GeV.

5.1.2 Pre-selection at generator level

Since most of the samples used have all the 4 leptons final states, the first step is the selection of a $H \rightarrow 4e$ sample contained in the ECAL fiducial region.

Therefore, a filter module is applied to events: its function is to select at least two electrons and two positrons (at the generated level) having specific values of transverse momentum and eta coordinate. The main steps of the filter are:

1. look for a Higgs with two Z daughter particles;
2. check if each Z has two daughter particles (A and B);
3. check whether the A and B particles are electrons or positrons with a minimum transverse momentum (p_T) of 5 GeV and a maximum eta (η) value of 2.7;
4. if the event contains at least 2 electrons and 2 positrons satisfying those criteria, accept the event for the next analysis step.

These loose cuts put the necessary preselection at the generation level: they require the angular acceptance ($|\eta| < 2.7$) well within the electromagnetic calorimeter volume ($|\eta| \leq 3$) and the transverse momentum sufficiently high to allow a good efficiency in the electron selection and reconstruction.

5.2 Electron reconstruction

For a Higgs boson with a mass in the range $m_H < 300\ GeV/c^2$, the $ZZ^{(*)} \rightarrow e^+e^-e^+e^-$ final state always involves at least one low p_T electron, i.e. an electron with p_T well below $m_Z/2 \approx 45$ GeV/c^2. In the m_H range below the Z pair production threshold, where the Z and Z* bosons themselves receive in general only a small transverse momentum, the mean p_T of the softest electron falls in a range where a full combination of tracking and calorimetry information becomes important. This softest electron, which couples to the off-shell Z*, typically has $p_T < 10$ GeV/c for masses $m_H < 140$ GeV/c^2, as can be inferred from Fig. 5.1 and Fig. 5.2

Hence, an excellent electron reconstruction is essential down to very low p_T values, well below the range for which the reconstruction will be best controlled in CMS via measurements with SM single Z and single W production.

The reconstruction of electron objects is initiated by the presence of electromagnetic superclusters (see section 3.1). ECAL superclusters are then used to drive the finding of pixel seeds for the primary electron tracks: hits in the pixel layers are predicted by propagation of the energy weighted mean position of the supercluster backward through the magnetic field, under both charge hypotheses, toward the pixel detector. The 2 pixel hits found serve as seeds for the building

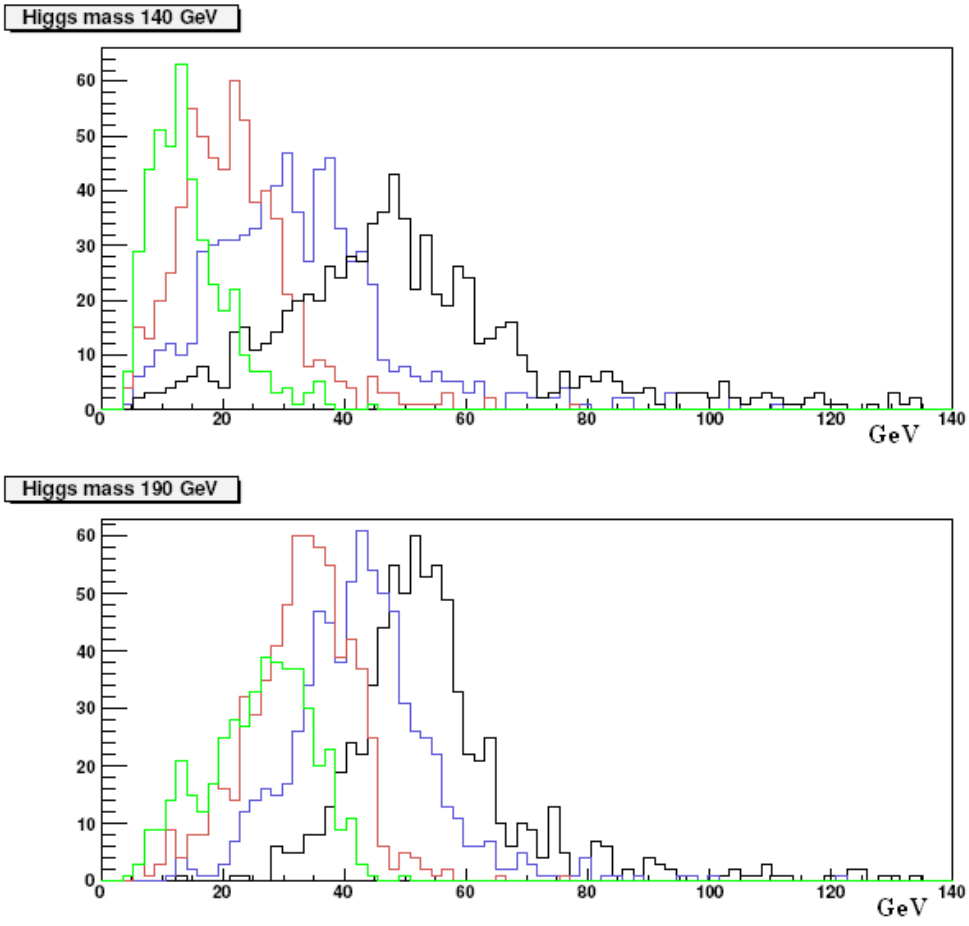

Figure 5.1: Electron pt sorted values for the $H \rightarrow 4e$ events analysed

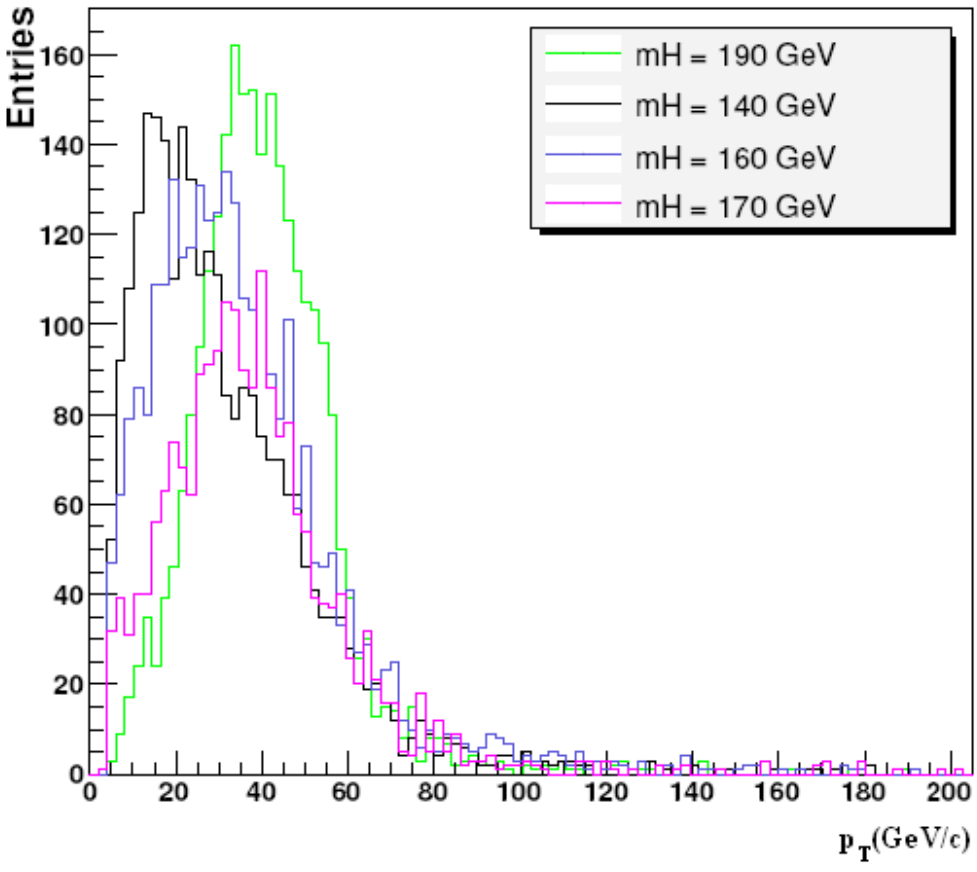

Figure 5.2: Reconstructed electron pt distributions for the $H \rightarrow 4e$ events analysed

and fitting of electron tracks in the Silicon Tracker. The default track reconstruction method in CMS relies on a simple Kalman Filter (KF) algorithm, but a nonlinear filter approach such as the Gaussian Sum Filter (GSF) had also been studied for track reconstruction and can in principle better describe the propagation of electrons. In this way, the tracker and ECAL information are combined for the electron energy measurement at low p_T and an error estimate is available for each reconstructed electron.

5.3 Data reduction at the triggering level and HLT efficiency

The events of interest for the Higgs boson search in the $H \rightarrow 4e$ channel must satisfy a minimal set of requirements. A first and compulsory condition for the events is to satisfy the CMS Level 1 trigger conditions and the filtering of the High Level trigger.

L1 trigger for electrons. L1 electromagnetic trigger is based on ECAL energy deposition and no attempt is made to distinguish between electrons and photons at this stage. Energy deposits in trigger towers are classified as isolated or non-isolated and the L1 trigger is then split into 4 paths requiring different E_T thresholds (see Tab. 5.1 for the 4 paths E_T thresholds. The relaxed triggers accept both isolated and non-isolated trigger deposits and are required to satisfy higher E_T thresholds.

L1 EM trigger path	E_T threshold (GeV)
Single isolated	12
Single relaxed	15
Double isolated	8
Double relaxed	10

Table 5.1: E_T thresholds for L1 electromagnetic trigger paths

HLT for electrons. The electromagnetic High Level trigger selection is then performed on the candidates passing the L1 trigger requirements, by applying a sequence of filters of increasing complexity. Several HLT algorithms are provided for triggering on electromagnetic objects. The list of requirements for electrons are shown in Tab. 5.2.

	Single Electron	**Double Electron**	**Relaxed Single Electron**	**Relaxed Double Electron**
L1 seed	L1_SingleIsoEG12	L1_DoubleIsoEG8	L1_SingleEG15	L1_DoubleEG10
$\|\eta\|$	< 2.5	< 2.5	< 2.5	< 2.5
E_t	> 15 GeV	> 10 GeV	> 17 GeV	> 12 GeV
$T_k isol$	< 0.06	< 0.4	< 0.06	< 0.4
HCAL isol barrel	< 3 GeV	< 9 GeV	< 3 GeV	< 9 GeV
HCAL isol endcaps	< 3 GeV	< 9 GeV	< 3 GeV	< 9 GeV
E/P barrel	< 1.5	–	< 1.5	–

Table 5.2: HLT electron paths: for each of the four paths a subsample of rejection cuts is shown for $10^{32} cm^{-2} s^{-1}$ luminosity.

The HLT algorithms are classified as a "single e", or a "double e", both in the two different shapes of "isolated" or "non isolated" (relaxed). Relaxed paths differ from isolated ones at the L1 trigger level: they do not impose isolation for the electromagnetic object at L1, and the increased rate is thus compensated by a higher transverse energy cut at the HLT level. The logical `OR` of those paths will be used to evaluate the efficiency of the trigger selection for the Higgs into 4 electrons decay channel.

5.3.1 Results: HLT performance tests

HLT efficiencies. The HLT efficiency measurement is performed in two ways:

- calculating the *absolute efficiency*, that is the number of events which have passed the HLT selection divided by the number of total "good" generated events which have passed the Filter

$$\varepsilon = \frac{HLT\ events}{All\ events}$$

- calculating the *efficiency relative to the L1 seed*, that is the number of events which have passed the HLT selection divided by the number of those events which have passed the L1 seed paths

$$\varepsilon = \frac{HLT\ events}{L1\ events}$$

The efficiencies for each HLT path decision and for the logical `OR` of all of them are evaluated. The latter is the total HLT efficiency for the $H \to ZZ^* \to 4e$ channel and requires that at least one of the four electromagnetic HLT paths is

satisfied by the event. See Tab. 5.3, 5.4, 5.5, 5.6 for the results obtained on different Higgs mass samples.

m_H **140 GeV**	**Single Electron**	**Relaxed Single**	**Double Electron**	**Relaxed Double**	**Logical** `OR`
Absolute	93.9%	93.2%	90.2%	91.2%	$(96.9 \pm 0.6)\%$
On L1 seed	94.2%	93.5%	92.2%	91.7%	

Table 5.3: HLT efficiencies computed on a MC sample of 783 $H \to 4e$ events

m_H **160 GeV**	**Single Electron**	**Relaxed Single**	**Double Electron**	**Relaxed Double**	**Logical** `OR`
Absolute	94.9%	95.5%	89.4%	94.4%	$(98.1 \pm 0.5)\%$
On L1 seed	95.2%	95.7%	90.8%	94.7%	

Table 5.4: HLT efficiencies computed on a MC sample of 831 $H \to 4e$ events

m_H **170 GeV**	**Single Electron**	**Relaxed Single**	**Double Electron**	**Relaxed Double**	**Logical** `OR`
Absolute	95.4%	95.8%	91.2%	94.4%	$(98.1 \pm 0.5)\%$
On L1 seed	95.6%	95.8%	92.6%	94.4%	

Table 5.5: HLT efficiencies computed on a MC sample of 593 $H \to 4e$ events

m_H **190 GeV**	**Single Electron**	**Relaxed Single**	**Double Electron**	**Relaxed Double**	**Logical** `OR`
Absolute	97.6%	97.3%	95.8%	97.4%	$(98.9 \pm 0.4)\%$
On L1 seed	97.6%	97.3%	95.9%	97.4%	

Table 5.6: HLT efficiencies computed on a MC sample of 732 $H \to 4e$ events

The efficiency error is calculated according to the statistical formula

$$\sigma_\epsilon = \sqrt{\frac{\epsilon(1-\epsilon)}{N}}$$

where ϵ is the efficiency value and N is the number of all events processed.

Sources of HLT inefficiency. The execution of the HLT paths produces an output trigger report where the detailed results for every algorithm called by the HLT are shown. This report is used to analyse the sources of inefficiency for each path. The main ones are:

- `Pixel Match Filter`, that is an algorithm which checks the match between pixel hits and supercluster and rejects candidates not associated with pixels;
- `Electron E over p Filter`, a filter on the supercluster energy over track momentum, requiring E/p < 1.5 for the barrel and E/p < 2.45 for the endcaps;
- `L1 seed`, that is a filter which checks the response of the L1 trigger; it is mainly responsible for the double electron paths inefficiency;
- `L1 Match Filter Regional`, which look for an η-ϕ match between the supercluster position, reconstructed by the HLT algorithms, and the L1 seed position; it is mainly responsible for inefficiency on the double electron paths.

HLT rates. The forecasted HLT rates produced by $H \rightarrow 4e$ events are evaluated, using the efficiencies already measured and according to Eq. 5.1.

$$\mathcal{R} = \sigma_{tot} \cdot (B.R.)_{(H \rightarrow ZZ^* \rightarrow 4e)} \cdot \epsilon_{pre} \cdot \mathcal{L} \cdot \epsilon_{HLT} \tag{5.1}$$

where

- σ_{tot} is the total cross section for the Higgs boson production
- $B.R._{(H \rightarrow ZZ^* \rightarrow 4e)}$ is the branching ratio for this physics channel
- ϵ_{pre} is the preselection efficiency depending on the Higgs mass hypothesis
- $\mathcal{L}$ is the start-up luminosity of $10^{32} cm^{-2} s^{-1}$
- ϵ_{HLT} is the HLT efficiency measured.

In table 5.7 and 5.8 the values for cross sections within acceptance and the obtained rates are respectively shown.

m_H $[Gev/c^2]$	σ_{NLO} [pb]	$\sigma_{NLO} \cdot B.R._{(H \to ZZ^* \to 4e)} \cdot \epsilon_{pre}$ [fb]
140	33.69	1.78
160	26.56	0.92
170	23.89	0.43
190	19.67	3.58

Table 5.7: Cross sections at BLO (pb) and cross sections multiplied by branching ratios and by generator pre-selection efficiency (fb), for different m_H.)

m_H $[Gev/c^2]$	**Single Electron**	**Relaxed Single**	**Double Electron**	**Relaxed Double**	**Logical OR**
140	1.58	1.57	1.51	1.53	1.63
160	0.84	0.85	0.79	0.84	0.87
170	0.42	0.42	0.40	0.41	0.43
190	3.53	3.52	3.44	3.52	3.57

Table 5.8: HLT rates for a luminosity of $10^{32} cm^{-2} s^{-1}$, computed on MC samples of $H \to 4e$ events $[10^{-7} Hz]$

background	$\sigma_{tot} \times B.R._{(final4e)} \times \epsilon_{pre}$ [fb]
ZZ^*	9.12
$Zb\bar{b}$	53.30
$t\bar{t}$	178.9

Table 5.9: Cross section values for background processes.

Background rates. In order to evaluate the HLT rates produced by background events, the background generated samples are also filtered and passed through the HLT paths. The corresponding HLT efficiencies are measured. In Tab. 5.9 the values for the background cross sections within acceptance are shown.

The filter applied on the background events requires the presence of 4 electrons in the final state within the ECAL acceptance, as for the signal. 3000 ZZ^* events and 6000 $t\bar{t}$ events have been filtered, with a filter efficiency of respectively ≈50% and ≈1%. In Tab. 5.10, 5.11, 5.12 the HLT measured efficiencies and rates for background events are listed ($Zb\bar{b}$ sample was missing).

Fig. 5.3 shows all the results on the HLT efficiency. The signal efficiency grows with the Higgs mass as expected, and it is always higher than 96%. In the same plot, background efficiencies are shown for a comparison.

This study proves that the current electromagnetic HLT algorithms are well-

background	**Single Electron**	**Relaxed Single**	**Double Electron**	**Relaxed Double**	**Logical OR**
ZZ^*	758.9	782.2	580.9	662.9	826.9
$Zb\bar{b}$	-	-	-	-	-
$t\bar{t}$	130.55	130.55	773.62	918.68	145.05

Table 5.10: HLT rates for a luminosity of $10^{32}cm^{-2}s^{-1}$, computed on MC samples of background (4e final state) events $[10^{-7}Hz]$; $Zb\bar{b}$ data are missing.

ZZ^*	**Single Electron**	**Relaxed Single**	**Double Electron**	**Relaxed Double**	**Logical OR**
Absolute	83.2%	85.8%	63.7%	72.7%	$(90.6 \pm 0.7)\%$
On L1 seed	86.5%	87.9%	77.7%	79.3%	

Table 5.11: HLT efficiencies computed on 3000 ZZ^* MC events (1490 $ZZ^* \rightarrow 4e$ events)

$t\bar{t}$	**Single Electron**	**Relaxed Single**	**Double Electron**	**Relaxed Double**	**Logical OR**
Absolute	72.9%	72.9%	43.2%	51.3%	$(81.1 \pm 4.5)\%$
On L1 seed	72.9%	72.9%	56.1%	52.7%	

Table 5.12: HLT efficiencies computed on 6000 $t\bar{t}$ events (74 $t\bar{t} \rightarrow 4e$ events)

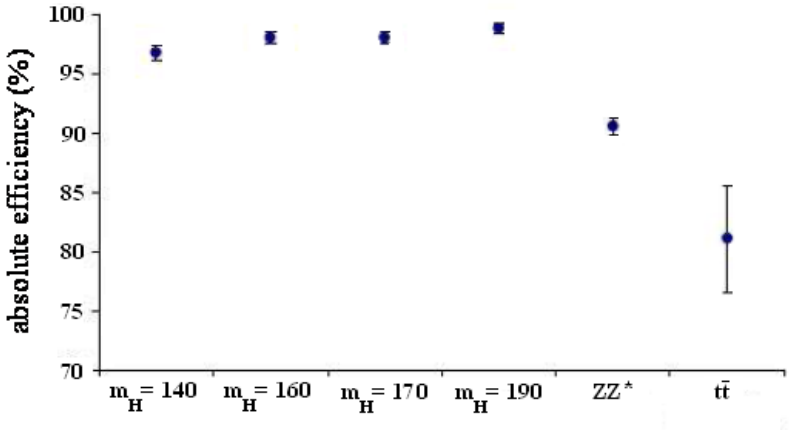

Figure 5.3: Signal and background efficiencies measured.

suited for the selection of the $H \rightarrow ZZ^* \rightarrow 4e$ events.

The HLT efficiency measurements with a more up-to-date CMSSW release. Similar HLT studies on the $H \rightarrow 4e$ channel have been performed with a more up-to-date software release (CMSSW_1_6_0), in order to validate it. The new release has a revised version of the electromagnetic HLT algorithms, where some cuts have been tuned to optimize the background rejection, particularly for the Higgs boson signal.
Generated samples of $H \rightarrow 4l$ for Higgs masses of 115 GeV, 130 GeV, 150 GeV and 195 GeV have been used. The samples have been filtered to select signal events falling in the ECAL fiducial region, requiring four electrons with $p_T > 5$ GeV and $|\eta| < 2.5$. The HLT efficiencies have been evaluated in the two luminosity scenarios of $\mathscr{L} = 10^{32} cm^{-2} s^{-1}$ (start-up) and of $\mathscr{L} = 10^{33} cm^{-2} s^{-1}$ (low luminosity). In Tab. 5.13 and 5.14 the absolute efficiency for all the paths and all the Higgs masses are shown for the two different luminosity scenarios.

m_H	**Single Electron**	**Relaxed Single**	**Double Electron**	**Relaxed Double**	**Logical OR**
115 GeV	90.6%	89.9%	84.7%	86.1%	$(95.3 \pm 0.6)\%$
130 GeV	93.6%	92.5%	88.7%	90.1%	$(97.4 \pm 0.3)\%$
150 GeV	94.9%	95.0%	91.2%	93.6%	$(98.0 \pm 0.2)\%$
195 GeV	96.9%	97.5%	94.2%	96.6%	$(99.0 \pm 0.2)\%$

Table 5.13: HLT absolute efficiencies computed on MC samples of ≈23000 $H \rightarrow 4l$ events, with a filter efficiency of ≈ 6%-7%. Start-up luminosity scenario.

m_H	**Single Electron**	**Double Electron**	**Relaxed Double**	**Logical OR**
115 GeV	78.8%	81.2%	71.1%	$(91.4 \pm 0.8)\%$
130 GeV	82.7%	86.3%	77.6%	$(94.1 \pm 0.5)\%$
150 GeV	87.4%	89.9%	87.4%	$(96.6 \pm 0.3)\%$
195 GeV	94.2%	94.1%	94.9%	$(98.3 \pm 0.2)\%$

Table 5.14: HLT absolute efficiencies computed on MC samples of ≈23000 $H \rightarrow 4l$ events, with a filter efficiency of ≈ 6%-7%. Low luminosity scenario (the single relaxed electron path is not used at this luminosity).

In Fig. 5.4 and Fig. 5.5 the obtained efficiencies (for the logical OR of all the paths) are shown, in comparison to the measured efficiencies for the other $4l$ final state decays ($H \rightarrow 4\mu$, $H \rightarrow 2e2\mu$). Due to the new HLT cuts, the results are

slightly worse than in the previous release, but still acceptable for the following analysis steps.

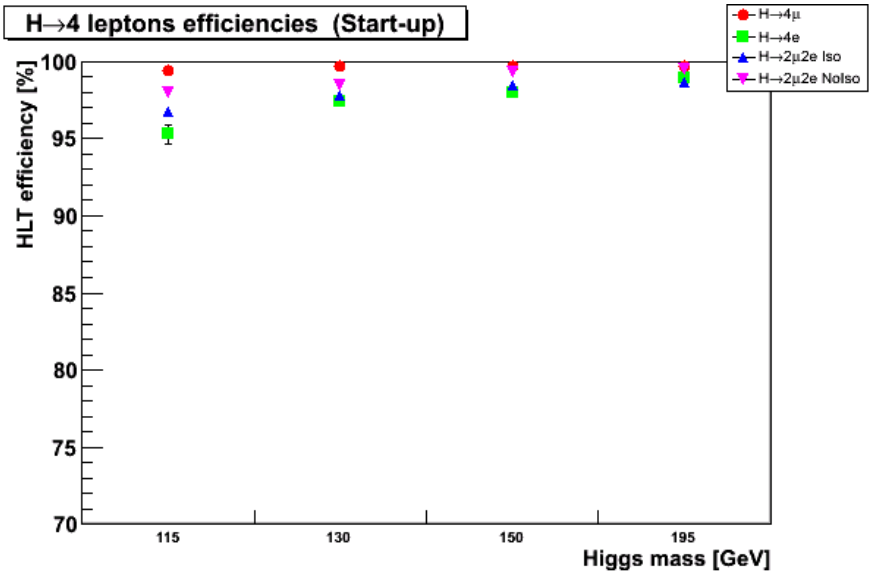

Figure 5.4: Signal HLT efficiency measured for the $H \rightarrow ZZ* \rightarrow 4e$ channel, compared to the results obtained for the other 4 leptons final state decays; start-up luminosity scenario.

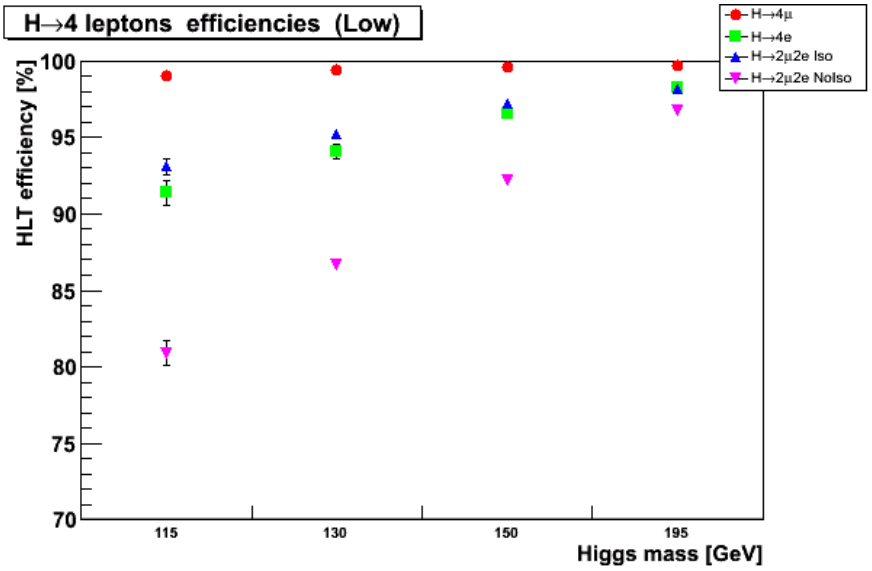

Figure 5.5: Signal HLT efficiency measured for the $H \rightarrow ZZ* \rightarrow 4e$ channel, compared to the results obtained for the other 4 leptons final state decays; low luminosity scenario.

Conclusions

The Large Hadron Collider data taking will start in a few months and its design luminosity will be reached after an initial phase at $10^{30} - 10^{32} cm^{-2} s^{-1}$.
The work presented in this thesis covers the description and the performance studies of the algorithms which I developed for the CMS electromagnetic calorimeter startup. The ECAL performance has been studied in detail with cosmics muon data and the results obtained will be very useful to a better knowledge of the detector response. I particularly focused on high energy events collected during Spring 2008 data taking.
Moreover, during the CMS startup phase, a very fast and quite efficient calibration must be provided. I studied the feasibility of a ϕ-symmetry algorithm optimized on generated jet events, to calibrate ECAL channels evaluating achievable precision and time needed. During the first months of CMS data taking, this method will be tested and tuned with real data, to optimize the trigger thresholds as a function of the measured rates.
On the other side, the $H \rightarrow ZZ^* \rightarrow e^+e^-e^+e^-$ high level trigger path analysed in the last chapter meets our expectation for this channel, that can only be studied at full design luminosity.

Appendix A
Symmetry Lie group

In a symmetry Lie group G = SU(N) the generators T^α (hermitian operators) satisfy the algebra

$$\left[T^\alpha, T^\beta\right] = if^{\alpha\beta\gamma}T_\gamma$$

where $f^{\alpha\beta\gamma}$ are the structure constants. A Lie algebra is defined when these constants are given. Remember that a group representation is a set of hermitian matrices t^α (with dimension $d\times d$) which satisfy the Lie algebra commutation relations; d is the so called representation dimension. Among the Lie group representations we find the irreducible representations:

- a Fundamental representation (d = N), that is the N-dimensional vector in SU(N); it is also given a non-equivalent representation $\overline{N}$;
- an Adjoint representation ($d = N^2$-1), that is the representation that the algebra generators belong to; the adjoint representation matrices are defined by the structure constants themselves:

$$\left(t_G^\beta\right)_{\alpha\gamma} = if^{\alpha\beta\gamma}$$

If t^α is a matrix in the irreducible representation r, then

$$Tr[t^\alpha] = 0$$

$$Tr\left[t_r^\alpha, t_r^\beta\right] = C(r)\delta^{\alpha\beta}$$

where C(r) is a group typical constant and $C(r) = \frac{1}{2}$ if r is the fundamental representation, $C(r) = N$ if r is the adjoint one.

Appendix B
Monte Carlo generators

There are several available Monte Carlo event generators for proton-proton collisions: each of them simulates a hadronic final state corresponding to some particular model of the underlying physics; the details of the implementation of the physics are different but the underlying philosophy of the generators is the same. A general scheme of event generation can be split into the following phases:

1. hard scattering process (hard scattering usually calculated at LO), a process dependent phase where new physics can lie;

2. initial and final state parton showers (resummation of QCD logs), well described by the "QCD-known physics"; it is process independent;

3. perturbative decays (calculated in QCD, EW, BSM..), multiple perturbative scattering and non-perturbative hadronization processes; the hadronization process is model dependent and process independent;

4. soft underlying event and hadron decays; energy, process and model dependent.

The MonteCarlo generators differ for the model and the approximations[1] used. As for models, the generators can mainly be parton shower (PS) or matrix element (ME): parton shower generators are based on simplified matrix element calculations, performed at the parton level, and describe the parton fragmentation into hadrons through the parton showering; they are used for final states with soft and collinear partons. On the other side, ME generators work only at a partonic level, performing an exact matrix element calculation; they are used to describe final states with high energy partons well separated. PYTHIA (T. Sjostrand, 1994) and HERWIG (B. Webber et al., 1992) are examples of Leading Order Parton Shower generators, while ALPGEN (M.L.Mangano, M. Moretti, F.

[1] LO, NLO, and also NNLO

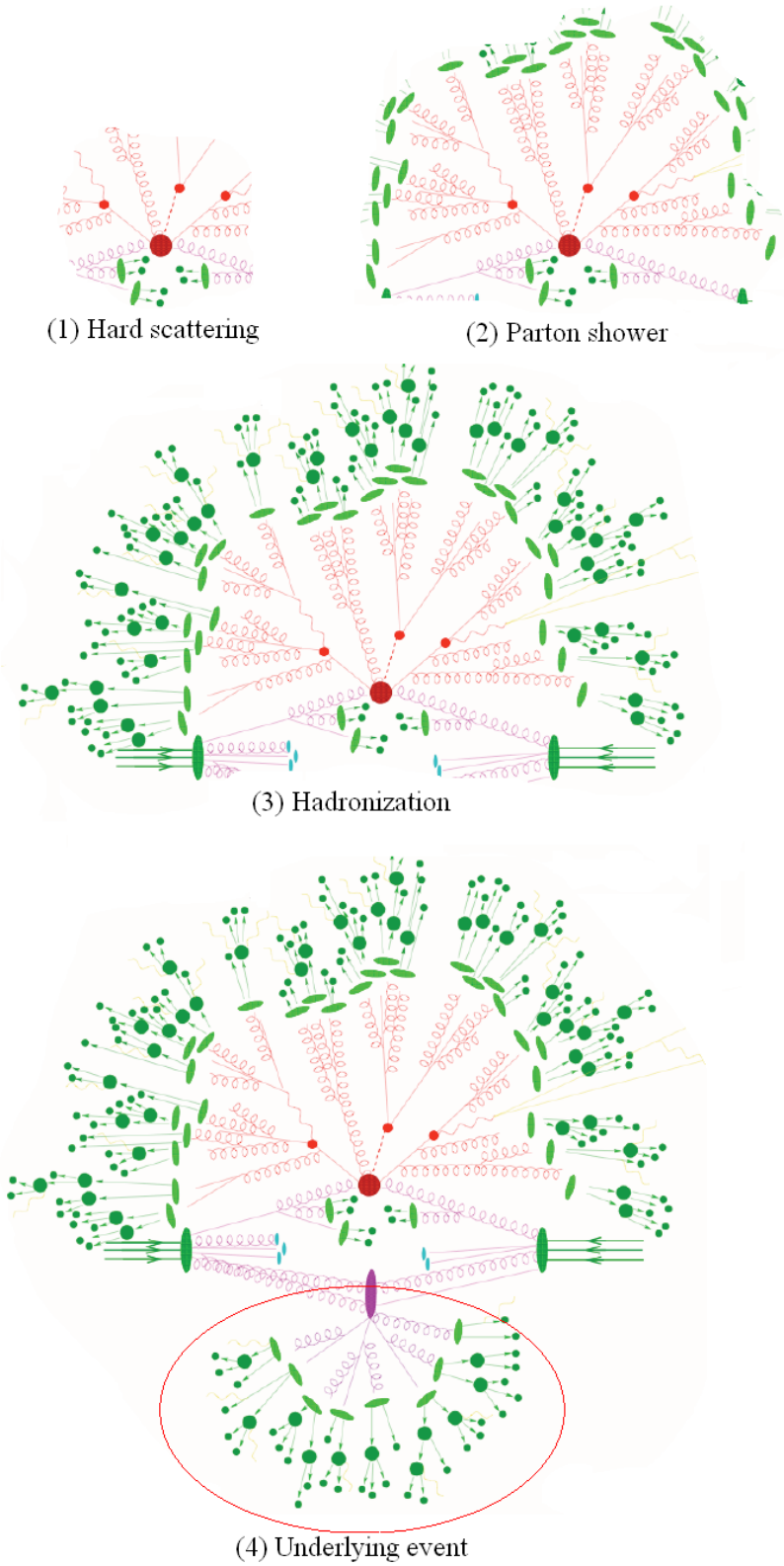

Figure 5.6: Schematic representation of a general pp collision event phases to be simulated.

Piccinini, R. Pittau, A. Polosa, 2002) or COMPHEP (A. Pukhov et al., 1999) are Matrix Element multi-partons generators; typically, a ME generator is merged with a parton shower one. In Fig. 5.7 some differences between parton showers and ME generators are listed.
The dominant cross section at the LHC consists of events with no hard scattering: these minimum bias events are important at LHC, particularly at design luminosity, as they overlap with interesting events. The generators use a different approach in this case: for instance, HERWIG uses a parametrization of data mainly from the CERN $p\bar{p}$ collider, while PYTHIA uses a mini-jet model where the jet cross section is used at very low transverse momenta (i.e. the hard scattering process is extrapolated until it saturates the total cross section). CMS uses the PYTHIA approach with dedicated modifications that agree with present data from Tevatron.

	matrix-elem MC's	shower MC's
final-state description	hard-parton jets. Describes geometry, correlations, ...	full information available at the hadron level
higher-order effects: loop corrections	hard to implement: must introduce negative probabilities	included as vertex corrections (Sudakov FF's)
higher-order effects: hard emissions	included, up to high orders (multijets)	approximate, incomplete phase space at large angles
resummation of large logs	?	unitarity implementation (i.e. correct shapes but not total rates)

Figure 5.7: Comparison between ME and parton shower generators.

Aknowledgements

Questo lavoro é stato possibile grazie alla disponibilitá, al sostegno, alla pazienza di alcune persone per le quali nutro stima e riconoscenza. Ho avuto la fortuna di incontrare persone entusiaste del proprio lavoro, capaci di esternare una sincera passione per la scienza e di trasmettere con semplicitá le proprie conoscenze, ma soprattutto persone umili e buone, in grado di anteporre l'amicizia a qualsiasi esigenza lavorativa.
Il mio primo ringraziamento va a Nadia. Molte delle scelte che hanno condizionato questi ultimi due anni di studi sarebbero state differenti senza la sua fiducia ed il suo appoggio, senza la sua presenza e i suoi incoraggiamenti positivi. In lei riconosco una guida ed un Maestro. Un enorme ringraziamento va a Stefano e Roberta, per l'aiuto, i tanti insegnamenti e i bei momenti trascorsi insieme, ma anche per avermi regalato la consapevolezza che la passione per la fisica puó sicuramente conciliarsi con l'amore per la famiglia. Vorrei ringraziare poi Ezio Menichetti per i preziosi suggerimenti, Nicoló Cartiglia per le spiegazioni elargite con coinvolgente entusiasmo, e Margherita Obertino per l'aiuto dimostrato in questi ultimi mesi. Thanks a lot to Toyoko Orimoto, for her helpfulness and kindness, and to all the CMS ECAL Prompt Feedback Analysis Group. Un grazie di cuore fa infine al gruppo di CMS Torino e a tutti gli "abitanti" del secondo piano, in particolare ai dottorandi e ai miei compagni di ufficio, per avermi accolto con affetto, a Matteo, per la sua allegria, gentilezza e onestá disarmanti, e ad Alberto ed Andrea, tolleranti ascoltatori e compagni fedeli in questa avventura.

Ma questo lavoro é stato possibile solamente grazie al sostegno incondizionato e alle premure ricevute da quanti mi vogliono bene da sempre. Alla mamma, per la sua forza e purezza, la sua comprensione, il suo bene senza riserve, per il suo profumo, i vestiti colorati, la solaritá e l'energia inesauribile, e al papá, per la sua tenerezza e il suo sostegno silenzioso, per gli scherzi e le risate, per i libri, i dischi, per i suoi capelli in continuo mutamento, a mamma e papá insieme, stupendi, dolci, complici e alleati sempre presenti. Alla nonna Ninna, perché é la persona migliore che abbia mai conosciuto, al suo coraggio e alla sua generositá, per le

lezioni di cucito, le interminabili storie, i pranzi, per i suoi occhi buoni. A mio zio Felice, per i suoi sempre nuovi aneddoti e racconti, le barzellette e il ricordo dei Natali passati assieme, a mio zio perché mi ha sempre incoraggiato e apprezzato. Un grazie va anche alla nonna Ivanna e a tutta la mia famiglia, a quanti si sono allontanati e a quanti sono invece ritornati, nel bene e nel male, perché spero che tutto possa un giorno sistemarsi. Vorrei anche ringraziare Maria Luisa e Rodolfo, per l'appoggio affettuoso e costante, il professor Dauria, per avermi convinto a seguire questa strada, e il mio maestro di musica Davide Biancolli, perché mi ha insegnato cosa significa imparare divertendosi.

Infine, un abbraccio forte forte va a tutti i miei amici, agli amici di fisica, agli amici del CERN e agli amici di sempre. Per le chiacchiere, i discorsi, le feste, i té e i gelati, per le passeggiate e le gite, le risate, la musica. Per avermi consolato nei momenti difficili. Per aver sopportato e per aver capito. Un abbraccio ai Waste Pipes, per i tanti concerti che mi hanno accompagnato in questi anni, e ad Acca, per esserci sempre stato. Un grazie speciale va a Cate, che mi ha insegnato a credere nei propri sogni e a lottare per realizzarli.

A Daniele, che é entrato nella mia vita con un té alla vaniglia e mi ha trascinato in un nuovo favoloso mondo.

We made a promise we swore we'd always remember
No retreat, baby, no surrender.

Bibliography

[1] CMS Collaboration, *The CMS Physics Technical Design Report, Vol. I: Detector performance and software*, CERN/LHCC 2006-001 and CMS TDR 8.1, (2006);

[2] CMS Collaboration, *The CMS Physics Technical Design Report, Vol. II: Physics Performance*, CERN/LHCC 2006-021 and CMS TDR 8.2, (2006);

[3] CMS Collaboration, *CMS Wiki Pages*, `https://twiki.cern.ch/twiki/bin/view/CMS/`;

[4] The CMS Electromagnetic Calorimeter Group, *Reconstruction of the signal amplitude of the CMS electromagnetic calorimeter*, Eur.Phys.JC46, (2006) 23-25;

[5] ECAL Collaboration, *Intercalibration of the barrel electromagnetic calorimeter of the CMS experiment at start-up*, CMS Note (2008) 018, in preparation;

[6] Baden A.R., *Jets and kinematics in hadronic collisions*, Int. J. Mod. Phys. (1998) A13:1817-1845;

[7] Futyan D., *Intercalibration of the CMS Electromagnetic Calorimeter Using Jet Trigger Events*, CMS Note (2004) 2004/007;

[8] Futyan D., *Intercalibration of ECAL crystals in ϕ Using Symmetry of Energy Deposition*, CMS Note (2002) 2002/031;

[9] Sterman G., *An introduction to Quantum Field Theory*, (1993);

[10] Particle Data Group, *Review of Particle Physics*, Phys. Lett. B592 (2004) 1-1109;

[11] CMS Collaboration, *CMS High Level Trigger*, CERN/LHCC (2007) 2007-021;

[12] Agostino L., Pieri M., *High Level Tigger Selection of Electrons and Photons*, CMS Note (2006) 2006/078;

[13] Meridiani P., *The calibration strategy of the CMS electromagnetic calorimeter*, proceeding of the 9th ICATPP Conference on Astroparticle, Particle, Space Physics, Detectors and Medical Physics Applications, Como, (2005);

[14] Oggero S., *Summer Student Project Report*, (2007);

[15] Oggero S., Orimoto T., Doglioni C., Gozzelino A., *High energy events in Ecal*, talk for the CMS ECAL Prompt Feedback Analysis Group, (20/05/2008);

[16] Oggero S., Orimoto T., *High energy events in Ecal -upgrades ongoing-*, talk for the CMS ECAL Prompt Feedback Analysis Group, (10/06/2008);

[17] Oggero S., Obertino M., *High energy events in Ecal -update on CRUZET I data-*, talk for the CMS ECAL Prompt Feedback Analysis Group, (17/06/2008);

[18] Orimoto T., *ECAL in CRUZET*, talk for the CMS Run Coordination Meeting, (30/05/2008);

[19] Cooper S., *CRUZET: An ECAL Overview*, talk for the CMS ECAL Detector Preformance Group, (15/05/2008);

[20] Haupt J., *The ECAL Commissioning timing, CRUZET and Laser*, talk for the CMS ECAL Detector Preformance Group, (15/05/2008);

[21] Haupt J., *ECAL Commissioning Data Tutorial*, talk for the CMS ECAL Prompt Feedback Analysis Group, (29/04/2008);

[22] Doglioni C., *Iguana visualization of CRUZET events*, talk for the CMS ECAL Prompt Feedback Analysis Group, (20/05/2008);

[23] Doglioni C., *Noise studies on P5 data*, talk for the CMS ECAL Detector Performance Group, (12/06/2008);

[24] Acosta D., *CSA08 goals for physics and DPG*, talk for the Offline Computing Meeting, (2008);

[25] Dafinei I., *Lead tungstate crystals for the CMS Electromagnetic Calorimeter at the LHC*, 10th ICATPP Conference on Astroparticle, Particle, Space Physics, Detectors and Medical Physics Applications, Como, (2007);

[26] Ellis S.D., Huston J. et al., *Jets in Hadron-Hadron Collisions*, hep-ph/0712.2447;

[27] Iglesias C., *Jet Reconstruction*, talk for the IFAE Thursday Meetings, (2005);

[28] Brooke J. et al, *Updated Interface Specification for the CMS Level-1 Regional Calorimeter Trigger to Calorimeter Global Trigger*, CMS IN (2004) 2004/009;

[29] Andreev M., Bugaev E.V., *Muon bremsstrahlung on heavy atoms*, Phys. Rev. D55 (1997) 1233;

[30] Maltoni F., *LHC Physics and Monte Carlo*, lectures for the International School of Theoretical Physics, Parma, (2006);

[31] Salerno R., *Test beam results of the CMS Electromagnetic Calorimeter*, proceeding of the 9th ICATPP Conference on Astroparticle, Particle, Space Physics, Detectors and Medical Physics Applications, Como, (2005);

[32] Beauceron S., *Results of the 2006 test beam campaign for the CMS Electromagnetic Calorimeter*, Acta Phys.Polon. B proceedings, (2008);

[33] Ranieri R., *TheMicrostrip Trackermaterialbudget*, talk for theMaterialBudgetandEngineeringWorkingGroupMeeting, (2007);

[34] Mellado B. et al., *Higgs Production Cross-Sections and Branching Ratios for the ATLAS Higgs Working Group*, Phys. Com. (2007) 024;

[35] Apanasevich L., *Trigger Issues for JetMET and QCD*, talk for the CMS HCAL/JetMET/QCD trigger session, (2008);

[36] Baffioni S., Charlot C. et al., *Discovery potential for the SM Higgs boson in the* $H \to ZZ^{(*)} \to e^+e^-e^+e^-$ *decay channel*, CMS Note (2006) 2006/115;

[37] Tabarelli T., *ECAL Calibrations*, talk for the CMS ECAL Detector Preformance Group, (29/05/2008);

[38] Bellan R., *Muon Software Commissioning*, talk for the CMS Run Coordination Meeting, (30/05/2008);

[39] Donato F., *Appunti del corso di Fenomenologia delle Interazioni Fondamentali*, Torino (2007);

[40] Mariotti C., *Lezioni di fisica delle particelle 2*, Torino (2007);

[41] Bellan R., *Study and development of the CMS High Level Trigger and Muon Reconstruction algorithms and their effects on the* $pp \to \mu^+\mu^- jjjj$ *Vector Boson fusion process*, PhD Thesis, (2007);

[42] Ferri F., *The CMS Electromagnetic Calorimeter for the Higgs Boson Search* $H \to ZZ^{(*)} \to 4e$ *at the LHC*, Tesi di Dottorato, (2005);

[43] Yazgan E., *Searcg for a Standard Model Higgs boson in CMS via Vector Boson fusion in the* $H \to WW \to l\nu l\nu$ *channel and optimization of energy reconstruction in CMS using test beam 2006 data*, PhD Thesis, (2007).

List of Figures

List of Tables